**Date:** April 11, 2017

Proposal for JLab PAC45

# Strange Quark Spectroscopy with a Secondary $K_L$ Beam at GlueX


Shankar Adhikari[1], Moskov J. Amaryan[2,*,†], Alexey V. Anisovich[3,4], Marouen Baalouch[2], Mikhail Bashkanov[5,†], Rene Bellwied[6], William J. Briscoe[7], William K. Brooks[8], Eugene Chudakov[9], Philip L. Cole[10], Volker Crede[11], Pavel Degtyarenko[9], Gail Dodge[2], Michael Döring[7,9], Michael Dugger[13], Hovanes Egiyan[9], Stuart Fegan[14], Gagik Gavalian[9], Viacheslav Gauzshtein[15,16], Derek I. Glazier[17], Jose Goity[9], Lei Guo[1], Helmut Haberzettl[7], Mirza Hadžimehmedović[18], Avetik Hayrapetyan[19], Tanja Horn[20], Charles E. Hyde[2], David Ireland[17], Benjamin C. Jackson[21], Christopher D. Keith[9], Chan W. Kim[7], Ivan Kuznetsov[15,16], Alexander B. Laptev[22], Iliya Larin[12], Valery E. Lyubovitskij[15,16,23,8], Maxim Mai[7], D. Mark Manley[24], Vincent Mathieu[25], Maxim Matveev[4], Kanzo Nakayama[21], Yongseok Oh[26], Hedim Osmanović[18], Rifat Omerović[18], Kijun Park[9], William Phelps[1], Eric Pooser[9], John W. Price[27], David Richards[9], Dan-Olof Riska[28], Barry G. Ritchie[13], James Ritman[29,†], Hui-Young Ryu[30], Elena Santopinto[31], Andrey V. Sarantsev[3,4], Daria Sokhan[17], Alexander Somov[9], Jugoslav Stahov[18], Justin R. Stevens[32,†], Igor I. Strakovsky[7,†], Alfred Švarc[33], Adam Szczepaniak[25,9], Simon Taylor[9], Daniel Watts[5], Nilanga Wickramaarachchi[2], Ronald L. Workman[7], Nicholas Zachariou[5], Bingsong Zou[34]

[1] Physics Department, Florida International University, Miami, FL, USA
[2] Old Dominion University, Norfolk, VA 23529, USA
[3] Helmholtz-Institut für Strahlen- und Kernphysik, Universität Bonn, 53115 Bonn, Germany
[4] National Research Centre "Kurchatov Institute", Petersburg Nuclear Physics Institute, Gatchina, 188300 Russia
[5] School of Physics and Astronomy, University of Edinburgh, Edinburgh EH9 3FD, United Kingdom
[6] Physics Department, University of Houston, Houston, TX 77204, USA
[7] The George Washington University, Washington, DC 20052, USA
[8] Universidad Tecnica Federico Santa Maria, Casilla 110-V, Valparaiso, Chile
[9] Jefferson Lab, Newport News, VA 23606, USA
[10] Idaho State University, Pocatello, ID 83209, USA
[11] Florida State University, Tallahassee, FL 32306, USA
[12] Institute for Theoretical and Experimental Physics, Moscow, 117218, Russia
[13] Arizona State University, Tempe, AZ 85267, USA
[14] Institut für Kernphysik, University of Mainz, D-55099 Mainz, Germany
[15] Tomsk State University, 634050 Tomsk, Russia

[16] Tomsk Polytechnic University, 634050 Tomsk, Russia
[17] SUPA School of Physics and Astronomy, University of Glasgow, Glasgow G12 8QQ, United Kingdom
[18] Faculty of Natural Sciences and Mathematics, University of Tuzla, 75000 Tuzla, Bosnia and Herzegovina
[19] II. Physikalisches Institut, Justus Liebig-University of Giessen, Giessen 35392, Germany
[20] The Catholic University of America, Washington, DC 20064, USA
[21] University of Georgia, Athens, GA 30602, USA
[22] LANL, Los Alamos, NM 87545, USA
[23] Institute of Theoretical Physics, University of Tübingen, D-72076 Tübingen, Germany
[24] Kent State University, Kent, OH 44242, USA
[25] Center for Exploration of Energy and Matter, Indiana University, Bloomington, IN 47403, USA
[26] Kyungpook National University, Daegu 702-701, Republic of Korea
[27] California State University, Dominguez Hills, Carson, CA 90747, USA
[28] Finnish Society of Science and Letters, 10130 Helsinki, Finland
[29] Institut für Experimentalphysik I - Ruhr-Universität, 44780 Bochum, Germany
Institute für Kernphysik & Jülich Center für Hadron Physics, 52425 Jülich, Germany
[30] Department of Physics, Pusan National University, 46241 Busan, Republic of Korea
[31] I.N.F.N. Sezione di Genova, 16146 Genova, Italy
[32] College of William and Mary, Williamsburg, VA 23185, USA
[33] Rudjer Bošković Institute, 10002 Zagreb, Croatia
[34] Institute of Theoretical Physics, Chinese Academy of Sciences, Beijing 100190, People's Republic of China
[*] Contact Person
[†] Spokesperson

**Abstract**

We express our interest in creating a secondary beam of neutral kaons in Hall D at JLab to be used with the GlueX experimental setup for strange hadron spectroscopy. The flux of the order of $\sim 10^4 K_L/s$ on physics targets of the GlueX will allow a broad range of measurements to be made by improving statistics of previous data obtained on hydrogen targets by almost two orders of magnitude. Use of a deuteron target will provide measurements in a completely unexplored region of *terra incognita*.

The experiment should measure both differential cross sections and self-analyzed polarizations of the produced $\Lambda$, $\Sigma$, and $\Xi$ hyperons using the GlueX detector at the Jefferson Lab Hall D. The measurements will span c.m. $\cos\theta$ from -0.95 to 0.95 in the c.m. range above $W = 1490$ MeV and up to 4000 MeV. New GlueX data will greatly constrain partial-wave analyses and reduce model-dependent uncertainties in the extraction of strange resonance properties (including pole positions), providing a new benchmark for comparisons with QCD-inspired models and LQCD calculations.

The proposed facility will also have an impact in the strange meson sector by providing measurements of the final-state $K\pi$ system from threshold up to 2 GeV in the invariant mass to establish and improve on pole positions and widths of all $K^*(K\pi)$ P-wave states as well as for the S-wave scalar meson $\kappa(800)$.

# Contents

# 1 Scope of Proposal

The nature of QCD confinement continues to provide an ongoing challenge to our understanding of soft QCD. Studies of the baryon spectrum provide one avenue to learn more about this unique feature since the location and properties of excited states reflect the dynamics and relevant degrees-of-freedom within hadrons.

Through analyses of decades worth of data, from both hadronic and electromagnetic (EM) scattering experiments, we have found numerous baryon resonances, and determined their masses, widths, and quantum numbers. There are 109 baryons in PDG2016 Listings [1] and only 58 of them are $4^*$ or $3^*$ [1]. Many more states have been predicted by quark models (QMs). For example in case of $SU(6) \times O(3)$, it would be required 434 resonances, if all revealed multiplets were completed (three 70 and four 56).

Three light quarks can be arranged in six baryonic families, $N^*$, $\Delta^*$, $\Lambda^*$, $\Sigma^*$, $\Xi^*$, and $\Omega^*$. The number of members in a family that can exist is not arbitrary [2]. If $SU(3)_F$ symmetry of QCD is controlling, then for octet: $N^*$, $\Lambda^*$, and $\Sigma^*$, and for decuplet: $\Delta^*$, $\Xi^*$, and $\Omega^*$. The number of experimentally identified resonances of each baryon family in PDG2016 summary tables is 17 $N^*$, 24 $\Delta^*$, 14 $\Lambda^*$, 12 $\Sigma^*$, 7 $\Xi^*$, and 2 $\Omega^*$. Constituent QMs, for instance, predict the existence of no fewer than 64 $N^*$ and 22 $\Delta^*$ states with mass less than 3 GeV. The seriousness of the "missing-states" problem [3] is obvious from these numbers. To complete $SU(3)_F$ multiplets, one needs no less than 17 $\Lambda^*$s, 41 $\Sigma^*$s, 41 $\Xi^*$s, and 24 $\Omega^*$s.

If such kind of "missing resonances" exist, these states have either eluded detection or have produced only weak signals in the existing data sets. The search for such resonances provides a natural motivation for future measurements at Jefferson Lab. As stated in the *2015 Long Range Plan for Nuclear Science* [4]: *For many years, there were both theoretical and experimental reasons to believe that the strange sea-quarks might play a significant role in the nucleon's structure; a better understanding of the role of strange quarks became an important priority.*

Low-lying baryon resonances, both hyperons and non-strange states, are usually considered as three-quark systems. But the quarks in such consideration are constituent, not current ones. This prevents their description by the well-understood perturbative QCD. It seems, however, that some qualitative consequences of QCD still work even for the non-perturbative constituent quarks. One of them is the suppression of effective strong interaction for the heavier s quark in comparison with the lighter $u$ and $d$ quarks (due to the asymptotic freedom). It is revealed, e.g., in smaller widths of hyperon resonances as compared with similar non-strange baryon resonances. The same phenomenon is seen also for meson resonances (compare widths of $K^*$ and $\rho$ meson resonances). Further investigation of this and other similar properties may help to improve our understanding of the nature of the constituent quarks and other non-perturbative effects.

The JLab12 energy upgrade, with the new Hall D, is an ideal tool for extensive studies of non-strange and, specifically, strange baryon resonances [5, 6]. Our plan is evolving to take advantage of the existing high quality photon beam line and experimental area in the Hall D complex at Jefferson Lab to deliver a beam of $K_L$ particles onto a liquid hydrogen/deuterium cryotarget ($LH_2/LD_2$) within the GlueX detector. The recently constructed GlueX detector in Hall D is a large acceptance spectrometer with good coverage for both charged and neutral particles that can be adapted to this purpose. Obviously, a $K_L$ beam facility with good momentum resolution is crucial to provide the data needed to identify and characterize the properties of hyperon resonances. The masses and widths of the lowest $\Lambda$ and $\Sigma$ baryons were determined mainly with kaon beam experiments in the 1970s [1]. First determinations of the pole position in complex energy plane for a hyperon, for instance for $\Lambda(1520)3/2^-$, has began to be studied recently [7]. An intense $K_L$ beam would open a new window of opportunity not only to locate "missing resonances" but also to establish their properties by studying different decay channels systematically.

The recent white paper, addressed to the physics with meson beams and endorsed by a broad physics community, summarized unresolved issues in hadron physics, and outlined the vast opportunities and advances that only become possible with a "secondary beam facility" [8]. The Hall D GlueX K-long Facility (KLF) measurements will allow studies of very poorly known multiplets of $\Lambda^*$, $\Sigma^*$, $\Xi^*$, and even $\Omega^*$ hyperons with unprecedented statistical precision, and have a potential to observe dozens of predicted (but heretofore unobserved) states and to establish the quantum numbers of already observed hyperons listed in PDG2016 [1]. Interesting puzzles exist for PDG listed excited hyperons that do not fit into any of the low-lying excited multiplets: they need to be further revisited and investigated. Excited $\Xi$s, for instance, are very poorly known. Establishing and discovering new states is important, in particular, for determination of the multiplet structure of excited baryons.

We organized three Worksops: *Physics with Neutral Kaon Beam at JLab* (KL2016) (February 2016) [9], *Excited Hyperons in QCD Thermodynamics at Freeze-Out* (YSTAR2016) (November 2016) [10], and *New Opportunities with High-Intensity Photon Sources* (HIPS2017) (February 2017) [11]. They were dedicated to the physics of hyperons produced by the neutral kaon beam. The KL2016 Workshop [12] follows our LoI–12–15–001 [13] to help address the comments made by the PAC43 and to prepare the full proposal for PAC45. Obviously, the proposed GlueX KLF program is complementary, for instance, to the CLAS12 baryon spectroscopy experiments [14, 15] and would operate in Hall D for several years. The YSTAR2016 Workshop [16] is a successor to the recent KL2016 Workshop and considered the influence of possible "missing" hyperon resonances on QCD thermodynamics, on freeze-out in heavy ion collisions and in the early universe, and in spectroscopy. Finally, the HIPS2017 Workshop [17] aimed at producing an optimized photon source concept with potential increase of scientific output at Jefferson Lab, and at refining the science for hadron physics experiments benefitting from such a high-intensity photon source.

Additionally, the proposed facility will also have a great impact in the strange meson sector by measurements of final-state $K\pi$ system from threshold up to 2 GeV in the invariant mass to establish and improve on pole positions and widths of all $K^*(K\pi)$ P-wave states and the S-wave scalar meson $\kappa(800)$. In particular, the $\kappa(800)$ meson has been under discussion for decades and still remains to be unequivocally confirmed with corresponding quantum numbers by doing detailed phase-shift analysis with high statistics data [18]. A detailed study of the $K\pi$ system is very important to extract the so-called $K\pi$ vector and scalar form factors to be compared with $\tau \to K\pi\nu_\tau$ decay and can be used to constrain the $V_{us}$ Cabibbo-Kobayashi-Maskawa (CKM) matrix element as well as to be used in testing CP violation in decays of heavy $B$ and $D$ mesons into $K\pi\pi$ final state.

# 2 The Brief Case for Hyperon Spectroscopy

The present experimental knowledge of the strange hyperon spectrum is deplorably incomplete, despite the fact that the ground states of the strange hyperons have been known since the 1960's. In the case of the $\Lambda$ hyperon resonance spectrum, only the lowest negative parity doublet is well established even though the structure of these resonances remains under discussion. In the case of the $\Sigma$ and $\Xi$ hyperons, only the lowest decuplet resonance states $\Sigma(1385)$ and $\Xi(1530)$ are well understood.

The lowest positive-parity resonances in the spectrum of the $\Lambda$ and $\Sigma$ hyperons, the $\Lambda(1600)$ and $\Sigma(1660)$ are experimentally known, but their structure is not. In the case of the $\Xi$ hyperon, the lowest positive-parity resonance remains unknown.

To settle the nature of the hyperon resonances, their main decay modes have to be determined by experiment. A clear example of how the decay modes can settle the structure of the resonances is provided by the $\pi$-decay widths of the decuplets $\Delta(1232)$, $\Sigma(1385)$, and $\Xi(1530)$. The ratio of these decay widths is 13:4:1, whereas if they were simple 3-quark states, with 3, 2, and 1 light quark each, the ratio should be 9:4:1. Comparison of these ratios indicate that the $\Sigma(1385)$ and $\Xi(1530)$ appear to be 3-quark states, while the $\Delta(1232)$ is more complex and formed by a 3-quark core with a surrounding meson (or multiquark) cloud. This conclusion is well supported by extensive theoretical calculations [19, 20].

## 2.1 The $\Lambda(1405) - \Lambda(1520)\ 1/2^- - 3/2^-$ Doublet

In the simplest constituent quark model, the most natural $-$ and the oldest $-$ interpretation, is that this is a low-lying flavor singlet multiplet of three quarks (*uds*). Dynamical versions of this model, with two-body interactions between the quarks can describe the low mean energy of this multiplet, but not the 115 MeV splitting between them. This has led to suggestions that there may even be two different 1/2$^-$ states $-$ one dynamical low $\overline{K}N$resonance at 1405 MeV, and an unresolved higher state close to 1520 MeV [21]. If so, it is high time that the "missing" 1/2$^-$ higher-energy state be empirically identified. This problem indicates that the $\Lambda(1405)$ has a more complex multiquark structure. Modern lattice QCD (LQCD) calculations support the view that its structure is a $\overline{K}N$state [22]. In Skyrme's topological soliton model for the baryons, the low-lying $\Lambda(1405)$ state also appears naturally as mainly 5-quark state [23,24]. That model is consistent with QCD in the large color number limit. In purely hadronic model calculations this resonance appears as a $\overline{K}N$ bound state.

A counter argument is that there are similar low-lying flavor-singlet parity doublets in both the charm and bottom hyperon spectra: $\Lambda_c(1405) - \Lambda_c(2625)\ 1/2^- - 3/2^-$ and $\Lambda_b(1405) - \Lambda_b(2625)$ 1/2$^-$-3/2$^-$ doublets [1]. The ratio between the $1/2^- - 3/2^-$ splittings in these 3 doublets are 8.2:2.1:1, which is not far from the corresponding inverse ratios of the $K$, $D$ and $B$ mesons: 10.7:2.8:1. The latter is what one should expect from the gradual approach to heavy-quark symmetry with increasing meson (or constituent quark) mass if the quark structure of these three multiplets is similar. This pattern is also consistent with the large N$_C$ limit of QCD.

## 2.2 The Low Lying Positive Energy Resonances

In the spectra of the nucleon and the $\Lambda$ and $\Sigma$ hyperons, the lowest resonances all lie below the lowest negative-parity multiplets except for the flavor singlet doublet $\Lambda(1405) - \Lambda(1520)\ 1/2^- - 3/2^-$. This reversal of normal ordering cannot be achieved in the constituent quark model with purely color-spin-dependent quark interactions. These low-lying positive parity resonances are the $N(1440)$, $\Lambda(1600)$, and the $\Sigma(1660)$ 1/2$^+$ states. Their low energies do however appear naturally, if the interactions between the quarks are flavor dependent [25].

Present day LQCD calculations have not yet converged on whether these low-lying states can be described as having a main 3-quark structure [26]. This may reflect that there is a collective nature in the quark content of all these resonances, which has a low soft vibrational mode. Skyrme's topological soliton model for the baryons, which represents one version of the large color limit of QCD, describes these low-lying states as such vibrational states.

In the spectrum of the $\Xi$, the $\Xi(1690)$ may be such a 1/2$^+$ state as well, although the quantum numbers of that state are yet to be determined.

In the decuplet spectra corresponding a similar low-lying positive parity state has, however, so far only been definitely identified in the $\Delta(1232)$ spectrum: the $\Delta(1600)3/2^+$. In the spectrum of the $\Sigma(1385)$, $\Sigma(1840)3/2^+$ resonance very likely represents the corresponding positive parity state. It should be important to identify the corresponding $3/2^+$ state in the spectrum of the $\Xi^*$.

It is of course very probable that corresponding low-lying positive-parity states will be found in the spectra of the $\Lambda_c$ and $\Lambda_b$ hyperons, given the fact that they have low-lying negative parity states akin to those of the $\Lambda$ hyperon as described above. The experimental identification of those is an important task. Even if the still tentative resonance $\Lambda_c(2765)$ turns out to be a 1/2$^+$ state, its energy appears to be to high for being the equivalent of the $\Lambda(1600)$ in the charm hyperon spectrum.

In the spectrum of the $\Sigma_c$, the decuplet state $\Sigma_c(2520)$ is well established. The tentative resonance $\Sigma_c(2800)$ may, should it turn out to be a 1/2$^+$ state, correspond to the $\Sigma(1660)$ in the strange hyperon spectrum.

## 2.3 The Negative Parity Hyperon Resonances

In the spectrum of the nucleon, two well-separated groups of negative-parity resonaces appear above the 1/2$^+$ state $N(1440)$. In the 3 quark model, the symmetry of the lowest energy group is $[21]_{FS}[21]_F[21]_S$, i.e., it has mixed flavor (F) and spin (S) symmetry as well as mixed flavor-spin (FS) symmetry [25, 27]. This group consists of the $N(1535)1/2^-$ and the $N(1520)3/2^-$ resonances.

There is a direct correspondence in the spectrum of the $\Lambda$ hyperon to group of negative parity resonances in the $\Lambda(1670)1/2^-$ and the $\Lambda(1690)3/2^-$ resonances. There is also a repeat of this group in the spectrum of the $\Sigma$ hyperon in the two resonances $\Sigma(1620)1/2^-$ (tentative) and the $\Sigma(1670)3/2^-$ resonances.

These spin $1/2^-$ and $3/2^-$ states in the spectum of the nucleon have intriguing decay patterns.

The $N(1535)$ resonance has a large (32-52%) decay branch to $\eta N$, even though its energy lies very close to the $\eta N$ threshold. This pattern repeats itself in the case of the the $\Lambda(1670)$, which also has a substantial (10-25%) decay branch to the corresponding the $\Lambda\eta$ state, even though it lies even closer to the threshold for that decay. As the still uncertain $\Sigma(1620)1/2^-$ resonance is located almost exactly at the threshold for $\eta\Sigma$, there is naturally no signal for an $\eta\Sigma$ decay from it. The ratio of the $\eta$ decay widths of the $N(1535)$ and the $\Lambda(1670)$ is about 6:1, which suggests that the $\eta$ decay involves a pair of quarks rather than a single constituent quark as in the $\pi$ decay of the decuplet resonances.

In the spectrum of the $\Xi$ hyperon, none of the negative-parity multiplets are complete. The state $\Sigma(1820)3/2^-$ may be the analog in the $\Xi$ spectrum of the states $N(1520)$, $\Lambda(1670)$, and $\Sigma(1670)$. It should be important to identify the lowest $1/2^-$ resonance in the $\Xi$ spectrum. If that resonance lacks an $\eta$ decay branch, it would demonstrate that the $\eta$ decay of the $1/2^-$ resonances in the spectra of the nucleon, $\Lambda$ and $\Sigma$ involve two quarks.

It should also be important to determine whether the uncertain "bumps" referred to in the Particle Data Tables labelled $\Sigma(1480)$, $\Sigma(1560$, and $\Xi(1620)$ represent true resonances.

About 120 MeV above the $1/2^- - 3/2^-$ pair of nucleon resonances $N(1535)$ and $N(1520)$, the nucleon spectrum has three negative-parity resonances close in energy to one another. This multiplet is formed of the $N(1650)1/2^-$, $N(1700)3/2^-$, and $N(1675)5/2^-$ resonances. In the 3-quark model the symmetry configuration of these states are $[21]_{FS}[21]_F[21]_S$, i.e., their spin configuration is completely symmetric.

The analogs in the spectrum of the $\Lambda$ of the first and last of these nucleon resonances are the $\Lambda(1800)1/2^-$ and the $\Lambda(1830)5/2^-$ resonances. This correspondence remains uncertain, however, because the missing 3/2$^-$ state in this $\Lambda$ resonance multiplet has not yet been identified.

The analogs in the spectrum of the $\Lambda$ of the first and last of these nucleon resonances are the $\Lambda(1800)1/2^-$ and the $\Lambda(1830)5/2^-$ resonances. This correspondence remains uncertain, however, because the missing 3/2$^-$ state in this $\Lambda$ resonance multiplet has not yet been identified.

A common feature of all the 1/2$^-$ resonances in these multiplets have substantial $\eta$ decay branches.

The present knowledge of the spectrum of the $\Xi$ hyperons remains too incomplete to identify any member of the negative-parity multiplet with the symmetry structure $[21]_{FS}[21]_F[21]_S$.

## 2.4 Summary for the Brief Case

This overview shows that the present empirical knowledge of the spectrum of the strange hyperons remains remarkably incomplete. As a consequence the quark structure of even the lowest energy resonances remains uncertain. Only an experimental determination of the lowest energy positive- and negative-parity hyperon resonances and their decay branches would settle the main open issues.

In the spectrum of the $\Lambda$ hyperon, there remains a question of the existence of a 1/2$^-$ partner to the $\Lambda(1520)3/2^-$ resonance. In addition, it should be important to search for the missing 3/2$^-$ $\Lambda$ resonance near 1700 MeV. Equally important would be the search for the apparently "missing"

3/2$^-$ state near 1750 MeV in the spectrum of the $\Sigma$ hyperon.

Our present knowledge of the spectrum of the $\Sigma$ hyperons remains too incomplete to identify any member of the corresponding negative-parity multiplet formed of 1/2$^-$, 3/2$^-$, and 5/2$^-$ resonances.

It should also be important to determine, whether the uncertain "bumps" referred to in the Particle Data Tables labelled $\Sigma(1480)$, $\Sigma(1560)$, and $\Sigma(1620)$ represent true resonances [1].

# 3 Strange Hadrons from the Lattice

it is coming

Experimental knowledge of the hadron spectrum is incomplete: more excited states are expected to exist. In Fig. 1, baryon spectra from [28] are presented in units of $\Omega$ mass from LQCD calculations with ensemble $m_\pi = 391$ MeV (not yet at physical $m_\pi$). The experimental situation for higher orts to map out these states. Moreover, LQCD calculations show that there are many states with strong gluonic content in the positive-parity sector for all baryons, presented by symbols with thick borders. The reason why hybrid baryons have not attracted the same attention as hybrid mesons is mainly due to the fact that they lack manifest "exotic" character. Although it is diffcult to distinguish hybrid baryon states, there is signicant theoretical insight to be gained from studying spectra of excited baryons, particularly in a framework that can simultaneously calculate properties of hybrid mesons [28–31]. Therefore, this GlueX KLF program will be very much complementary to the GlueX physics program for hybrid mesons.

# 4 The Interest of the RHIC/LHC Community in Excited Hyperon Measurements

The relativistic heavy-ion community at RHIC and the LHC has recently embarked on specific analyses to address the issue of strangeness hadronization. LQCD calculations in the QCD crossover transition region between a deconfined phase of quark and gluons and a hadronic resonance gas have revealed a potentially interesting sub-structure related to the hadronization process. Studies of flavor-dependent susceptibilities, which can be equated to experimental measurements of conserved quantum number fluctuations, seem to indicate a slight flavor hierarchy in the three quark sector (u,d,s) in thermalized systems. Specifically, the ratios of higher order susceptibilities in the strange sector show a higher transition temperature than in the light sector [32]. Both pseudo-critical temperatures are still within the error bars of the quoted transition temperature based on all LQCD order parameters [33, 34], which is 154±9 MeV, but the difference of the specific susceptibilities is around 18 MeV and well outside their individual uncertainties.

This difference seems to be confirmed by statistical thermal model calculations that try to describe the yields of emitted hadrons from a QGP based on a common chemical freeze-out temperature. Although the yields measured by ALICE at the LHC in 2.76 TeV PbPb collisions can be described

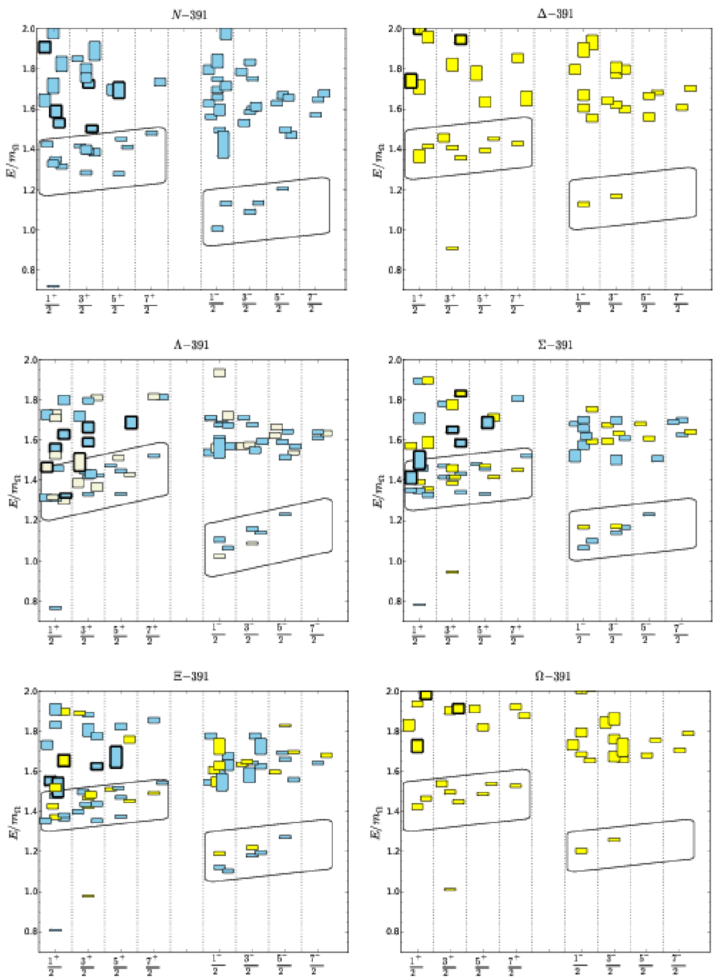


Figure 1: Results for baryon excited states using ensemble with $m_\pi = 391\ MeV$ are shown versus $J^P$ [28]. Colors are used to display the flavor symmetry of dominant operators as follows: blue for $8_F$ in $N$, $\Lambda$, $\Sigma$, and $\Xi$; beige for $1_F$ for $\Lambda$; yellow for $10_F$ in $\Delta$, $\Sigma$, $\Xi$, and $\Omega$. The lowest bands of positive and negative parity states are highlighted within slanted boxes. Hybrid states, in which the gluons play a substantive role, are shown for positive parity by symbols with thick borders.

by a common temperature of 156±2 MeV, with a reasonable $\chi^2$, the fit improves markedly if one allows the light quark baryons to have a lower temperature than the strange quark baryons [35]. A similar result has been found when the thermal fluctuations of particle yields as measured by STAR [36, 37], which can be related to the light quark dominated susceptibilities of the electric charge and the baryon number on the lattice, have been compared to statistical model calculations [38].

If one assumes that strange and light quarks indeed prefer different freeze-out temperatures, then the question arises how this could impact the hadronization mechanism and abundance of specific hadronic species. In other words, is the production of strange particles, in particular excited resonant states, enhanced in a particular temperature range in the crossover region? Strange ground-state particle production shows evidence of enhancement, but the most likely scenario is that the increased strange quark abundance will populate excited states; therefore, the emphasis of any future experimental program trying to understand hadron production is shifting towards strange baryonic resonance production. Furthermore recent LHC measurements in small systems, down to elementary proton-proton collisions, have revealed that even in these small systems there is evidence for deconfinement, if the achieved energy density, documented by the measured charged particle multiplicity is large enough [39]. Therefore future measurements in elementary collisions in the KLF experiment at JLab might well provide the necessary link to future analysis of strange resonance enhancements in heavy ion collisions at RHIC and the LHC and a deeper understanding of the hadronization process.

This statement is also supported by comparisons between the aforementioned LQCD calculations and model predictions based on a non-interacting hadronic resonance gas. The Hadron Resonance Gas (HRG) model [40–43] yields a good description of most thermodynamic quantities in the hadronic phase up to the pseudo-critical temperature. The idea that strongly interacting matter in the ground state can be described in terms of a non-interacting gas of hadrons and resonances, which effectively mimics the interactions of hadrons by simply increasing the number of possible resonant states exponentially as a function of temperature, was proposed early on by Hagedorn [44]. The only input to the model is the hadronic spectrum: usually it includes all well-known hadrons in the *Review of Particle Physics* (RPP), namely the ones rated with at least two stars. Recently, it has been noticed that some more differential observables present a discrepancy between lattice and HRG model results. The inclusion of not-yet-detected states, such as the ones predicted by the original Quark Model (QM) [45, 46] has been proposed to improve the agreement [47, 48]. A systematic study based on a breakdown of contributions to the thermodynamic pressure given by particles grouped according to their quantum numbers (in particular baryon number and strangeness) enables us to infer in which hadron sector more states are needed compared to the well-known ones from the RPP [49]. In case of a flavor hierarchy in the transition region one would expect the number of strange resonances to increase, due to a higher freeze-out temperature, compared to the number of light quark resonances. Figure 2 shows the effect of different strange hadron input spectra to the HRG model in comparison to LQCD. Fig. 2(upper plot) shows the number of states in PDG-2016 [1] , PDG-2016+ (incling one star states), the standard QM, and a Quark Model with enhanced quark interactions in the hadron (hyper central model hQM [50]). Fig. 2(lower plot) shows a comparison of the HRG results to a leading-order LQCD calculation of $\mu_s/\mu_B$, i.e., the ratio to strange to baryon number susceptibility [49]. .

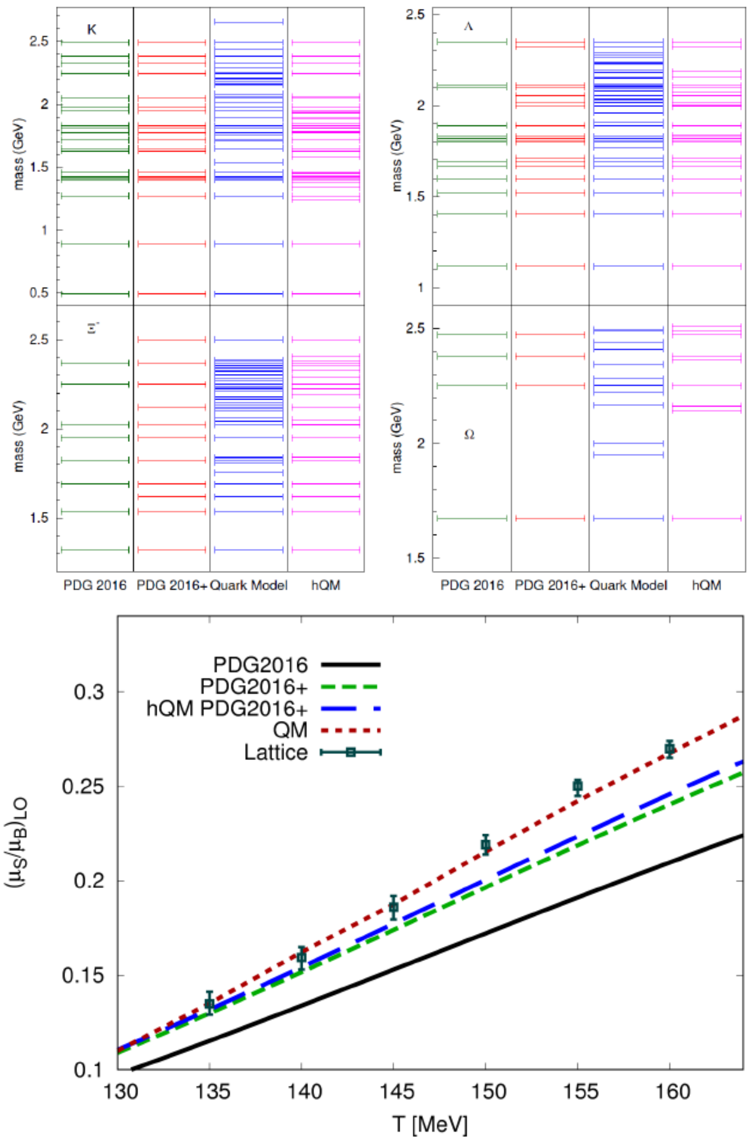


Figure 2: Upper plot: Comparison of predicted and measured excited strange hadronic states in PDG-2016, PDG-2016+ (including one star states), QM, and hQM. Lower plot: Lattice QCD calculation of the temperature dependence of the leading order susceptibility ratio ($\mu_s/\mu_B$) compared to results from HRG model calculations with varying number of hadronic states.

.

An interesting conclusion that arises from these studies is that the improvement in the listing of strange resonances between PDG-2008 [51] and PDG-2016 definitely brought the HRG calculations closer to the lattice QCD data. By looking at details in the remaining discrepancy, which is in part remedied by including one-star rated resonances in PDG-2016, it seems that the effect is more carried by singly strange resonances rather than multi-strange resonances, also in light of comparisons to quark models that include di-quark structures [52] or enhanced quark interactions in the baryon (hypercentral models [50]). This is good news for the experiments since the $\Lambda$ and $\Sigma$ resonances below 2 GeV/c$^2$ are will within reach of the KLF experiment and, to a lesser significance, the RHIC/LHC experiments. In this context it is also important to point out that the use of both hydrogen and deuterium targets in KLF is crucial since it will enable the measurement of charged and neutral hyperons. A complete spectrum of singly strange hyperon states is necessary to make a solid comparison to first-principle calculations.

In summary: Any comparisons between experimentally verified strange quark model states from YSTAR and LQCD will shed light on a multitude of interesting questions relating to hadronization in the non-perturbative regime, exotic particle production, the interaction between quarks in baryons and a possible flavor hierarchy in the creation of confined matter.

# 5 Previous Measurements

While a formally complete experiment requires the measurement, at each energy and angle, of at least three independent observables, the current database for $K_Lp \to \pi Y$ and $KY$ is populated mainly by unpolarized cross sections. Figure 3 illustrates this quite clearly.

As the first stage of the GlueX program, our favorite processes are two-body and quasi-two-body: elastic $K_Lp \to K_Sp$ and charge-exchange $K_Lp \to K^+n$ reactions, then two-body reactions producing $S = -1$ ($S = -2$) hyperons as $K_Lp \to \pi^+\Lambda$, $K_Lp \to \pi^+\Sigma^0$, and $K_Lp \to \pi^0\Sigma^+$ ($K_Lp \to K^+\Xi^0$). Most of previous measurements, induced by a $K_L$ beam, were collected for $W = 1454$ and up to 5054 MeV. Experiments were performed between 1961 and 1982 with mostly hydrogen bubble chambers at ANL, BNL, CERN, DESY, KEK, LRL, NIMROD, NINA, PPA, and SLAC. Note that some of data were taken at EM facilities at NINA [54] (a short overview about NINA experiments is given by Albrow recently [55]) and SLAC [56]. The goal of the Manchester University group that worked at the Daresbury 5-GeV electron synchrotron NINA was CP-violation, which was a hot topic back to mid 1960s. The main physics that the SLAC group addressed was a study of the systematics of particle anti-particle processes through the intrinsic properties of the K-longs.

The first paper that discussed the possibility that a useful neutral kaon beam could be made at an electron synchrotron by photoproduction was being considered, and a 1965 prediction for SLAC by Drell and Jacob was optimistic [57]. Nowadays high-quality EM facilities, such as JLab [13], are able to realize a full hyperon spectroscopy program.

The overall systematics of previous $K_L$p experiments varies between 15% and 35% and the energy binning is much broader than hyperon widths. The limited number of $K_L$ induced measurements 2426 $d\sigma/d\Omega$, 348 $\sigma^{tot}$, and 115 $P$ observables [53] do not allow to feel comfortable with the hyperon spectroscopy results today. There were no measurements using polarized targets, which means that there were no double polarized measurements that are critical for a complete experimental program. Additionally, we are not aware of any data on a "neutron" target.

Our knowledge about the non-strange sector is more advanced vs. the strange one [1]. For the non-strange case, for instance, phenomenology has access to 51k data of $\pi N \to \pi N$ and 39k data of $\gamma N \to \pi N$ below $W = 2.5$ GeV [58].

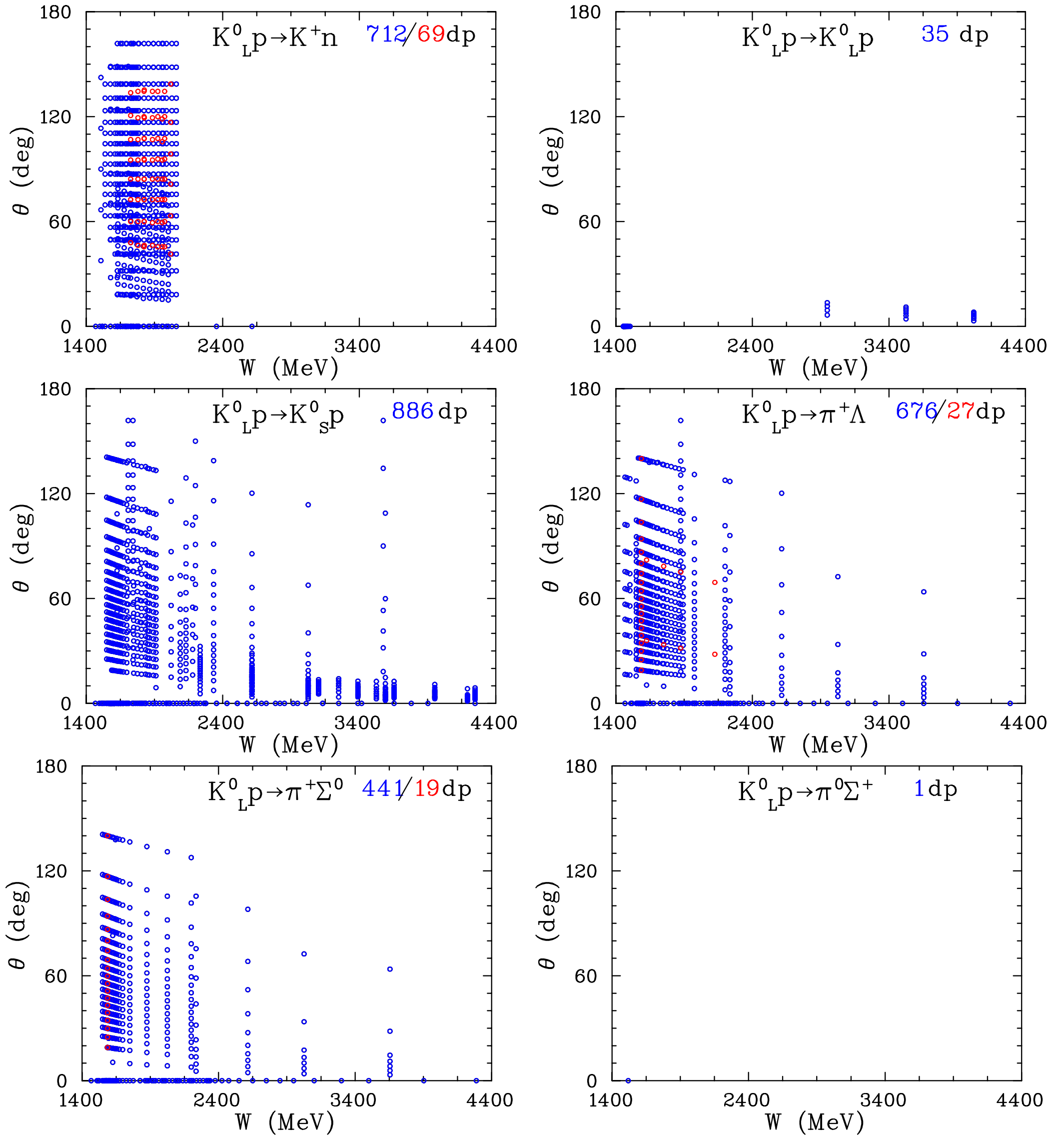


Figure 3: Experimental data available for $K_L p \to K^+ n$, $K_L p \to K_L p$, $K_L p \to K_S p$, $K_L p \to \pi^+ \Lambda$, $K_L p \to \pi^+ \Sigma^0$, and $K_L p \to \pi^0 \Sigma^+$ as a function of c.m. energy W [53]. The number of data points (dp) is given in the upper righthand side of each subplot [blue (red) shows amount of unpolarized (polarized) observables]. Total cross sections are plotted at zero degrees.

# 6 Phenomenology / Partial-Wave Analysis

Here, we summarize some of the physics issues involved with such processes. Following Ref. [59], the differential cross section and polarization for $K_L p$ scattering are given by

$$\frac{d\sigma}{d\Omega} = \lambdabar^2(|f|^2 + |g|^2), \tag{1}$$

$$P\frac{d\sigma}{d\Omega} = 2\lambdabar^2 \mathrm{Im}(fg^*), \tag{2}$$

where $\lambda\!\!\!^- = \hbar/k$, with $k$ the magnitude of c.m. momentum for the incoming meson. Here $f = f(W,\theta)$ and $g = g(W,\theta)$ are the usual spin-nonflip and spin-flip amplitudes at c.m. energy $W$ and meson c.m. scattering angle $\theta$. In terms of partial waves, $f$ and $g$ can be expanded as

$$f(W,\theta) = \sum_{l=0}^{\infty}[(l+1)T_{l+} + lT_{l-}]P_l(\cos\theta), \tag{3}$$

$$g(W,\theta) = \sum_{l=1}^{\infty}[T_{l+} - T_{l-}]P_l^1(\cos\theta), \tag{4}$$

where $l$ is the initial orbital angular momentum, $P_l(\cos\theta)$ is a Legendre polynomial, and $P_l^1(\cos\theta)$ is an associated Legendre function. The total angular momentum for the amplitude $T_{l+}$ is $J = l+\frac{1}{2}$, while that for the amplitude $T_{l-}$ is $J = l - \frac{1}{2}$. For hadronic scattering reactions, we may ignore small CP-violating terms and write

$$K_L = \frac{1}{\sqrt{2}}(K^0 - \overline{K^0}), \tag{5}$$

$$K_S = \frac{1}{\sqrt{2}}(K^0 + \overline{K^0}). \tag{6}$$

We may generally have both $I = 0$ and $I = 1$ amplitudes for $KN$ and $\overline{K}N$ scattering, so that the amplitudes $T_{l\pm}$ can be expanded in terms of isospin amplitudes as

$$T_{l\pm} = C_0 T^0_{l\pm} + C_1 T^1_{l\pm}, \tag{7}$$

where $T^I_{l\pm}$ are partial-wave amplitudes with isospin $I$ and total angular momentum $J = l \pm \frac{1}{2}$, with $C_I$ the appropriate isospin Clebsch-Gordon coefficients.

We plan to do a coupled-channel PWA with new GlueX data in combination with available and new J-PARC $K^-$ measurements when they will come. Then the best fit will allow determine data driven (model independent) partial amplitudes and associated resonance parameters (pole position, residual, Breit-Wigner (BW) parameters and so on) as the SAID group does, for instance, for analysis of $\pi N$-elastic, charge-exchange, and $\pi^- p \to \eta n$ data [60].

## 6.1 $KN$ and $\overline{K}N$ Final States

The amplitudes for reactions leading to $KN$ and $\overline{K}N$ final states are

$$T(K^-p \to K^-p) = \frac{1}{2}T^1(\overline{K}N \to \overline{K}N) + \frac{1}{2}T^0(\overline{K}N \to \overline{K}N), \tag{8}$$

$$T(K^-p \to \overline{K^0}n) = \frac{1}{2}T^1(\overline{K}N \to \overline{K}N) - \frac{1}{2}T^0(\overline{K}N \to \overline{K}N), \tag{9}$$

$$T(K^+p \to K^+p) = T^1(KN \to KN), \tag{10}$$

$$T(K^+n \to K^+n) = \frac{1}{2}T^1(KN \to KN) + \frac{1}{2}T^0(KN \to KN), \tag{11}$$

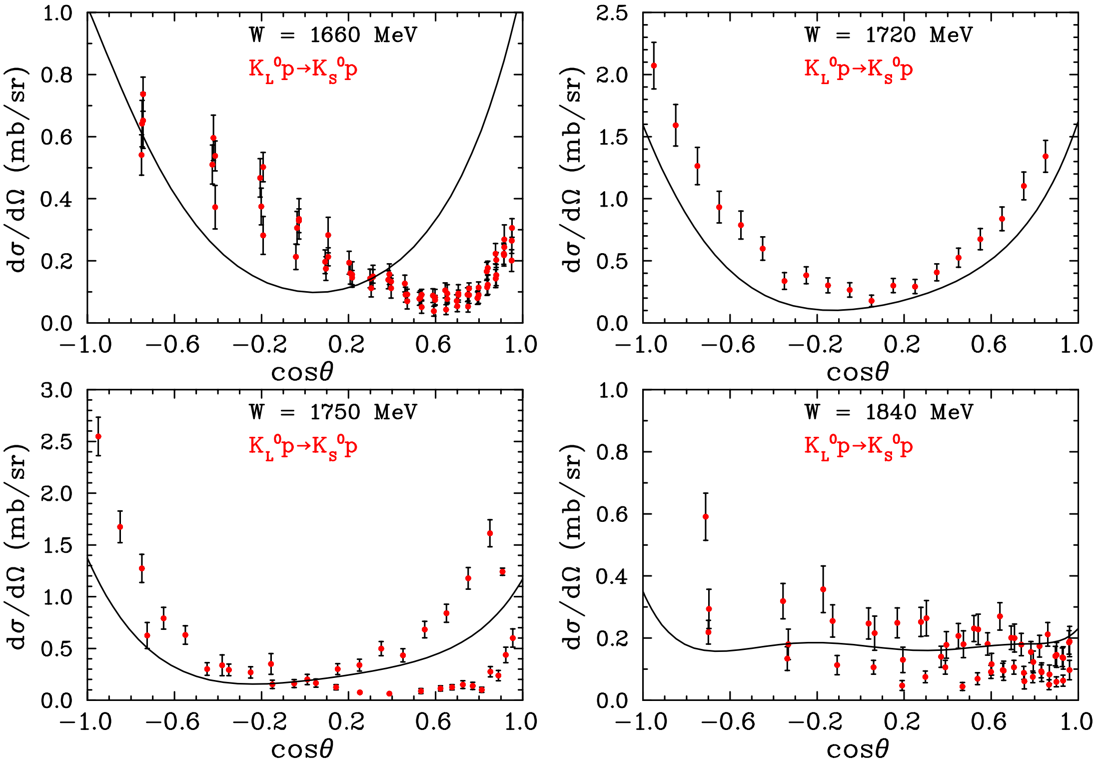


Figure 4: Selected differential cross section data for $K_L p \to K_S p$ at W = 1660 MeV, 1720 MeV, 1750 MeV, and 1840 MeV, from Ref. [61]. The plotted points from previously published experimental data are those data points within 20 MeV of the kaon c.m. energy indicated on each panel [58]. Plotted uncertainties are statistical only. The curves are predictions using amplitudes from the recent PWA of $\overline{K}N \to \overline{K}N$ data [62, 63], combined with $KN \to KN$ amplitudes from the SAID database [58].

$$T(K_L p \to K_S p) = \frac{1}{2}\left(\frac{1}{2}T^1(KN \to KN) + \frac{1}{2}T^0(KN \to KN)\right) - \frac{1}{2}T^1(\overline{K}N \to \overline{K}N), \quad (12)$$

$$T(K_L p \to K_L p) = \frac{1}{2}\left(\frac{1}{2}T^1(KN \to KN) + \frac{1}{2}T^0(KN \to KN)\right) + \frac{1}{2}T^1(\overline{K}N \to \overline{K}N), \quad (13)$$

No differential cross section data are available for $K_L p \to K_L p$ below $W \sim 2948$ MeV. A fair amount of data are available for the reaction, $K^+ n \to K^0 p$, measured on a deuterium target. Figure 4 shows a sample of available differential cross sections for $K_L p \to K_S p$ compared with predictions determined from our recent partial-wave analysis (PWA) of $\overline{K}N \to \overline{K}N$ data [62, 63], combined with $KN \to KN$ amplitudes from the SAID database [58]. The predictions at lower and higher energies tend to agree less well with the data.

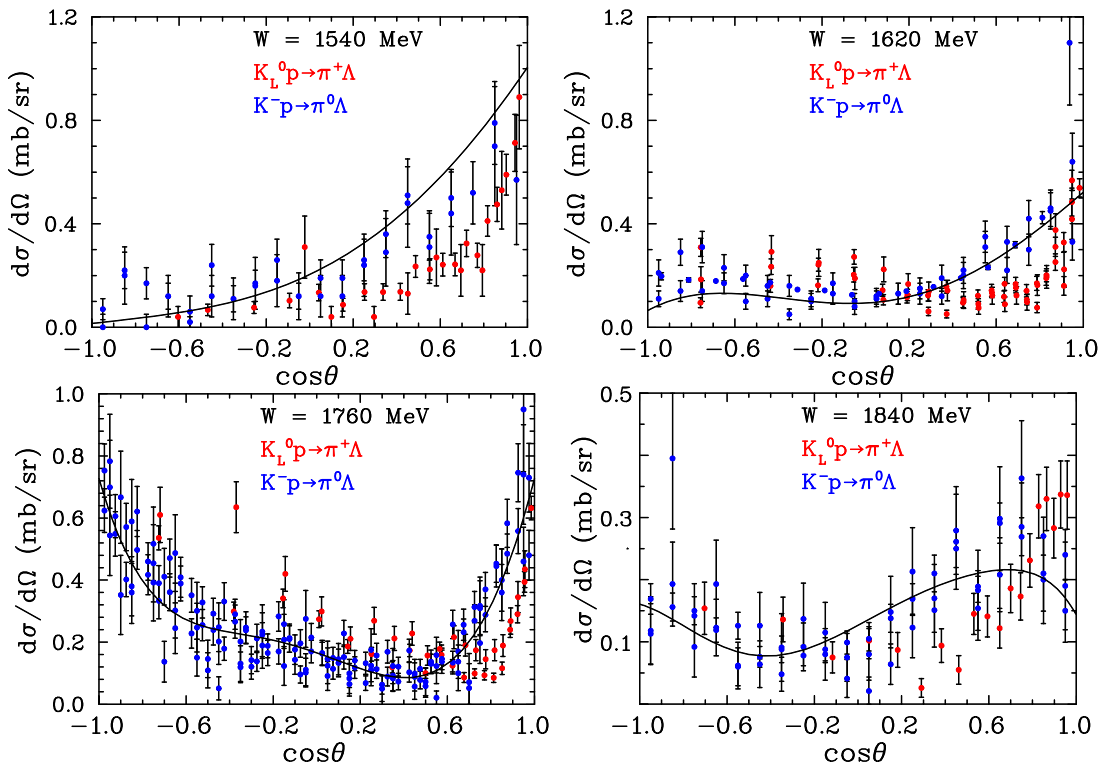


Figure 5: Comparison of selected differential cross section data for $K^-p \to \pi^0\Lambda$ and $K_Lp \to \pi^+\Lambda$ at W = 1540 MeV, 1620 MeV, 1760 MeV, and 1840 MeV, from Ref. [61]. The plotted points from previously published experimental data are those data points within 20 MeV of the kaon c.m. energy indicated on each panel [58]. Plotted uncertainties are statistical only. The curves are from the recent PWA of $K^-p \to \pi^0\Lambda$ data [62, 63].

## 6.2 $\pi\Lambda$ Final States

The amplitudes for reactions leading to $\pi\Lambda$ final states are

$$T(K^-p \to \pi^0\Lambda) = \frac{1}{\sqrt{2}}T^1(\overline{K}N \to \pi\Lambda), \quad (14)$$

$$T(K_Lp \to \pi^+\Lambda) = -\frac{1}{\sqrt{2}}T^1(\overline{K}N \to \pi\Lambda). \quad (15)$$

The $K^-p \to \pi^0\Lambda$ and $K_Lp \to \pi^+\Lambda$ amplitudes imply that observables for these reactions measured at the same energy should be the same except for small differences due to the isospin-violating mass differences in the hadrons. No differential cross section data for $K^-p \to \pi^0\Lambda$ are available at c.m. gies $W < 1540$ MeV, although data for $K_Lp \to \pi^+\Lambda$ are available at such energies. At 1540 MeV and higher energies, differential cross section and polarization data for the two reactions are in fair agreement, as shown in Figs. 5 and 6.

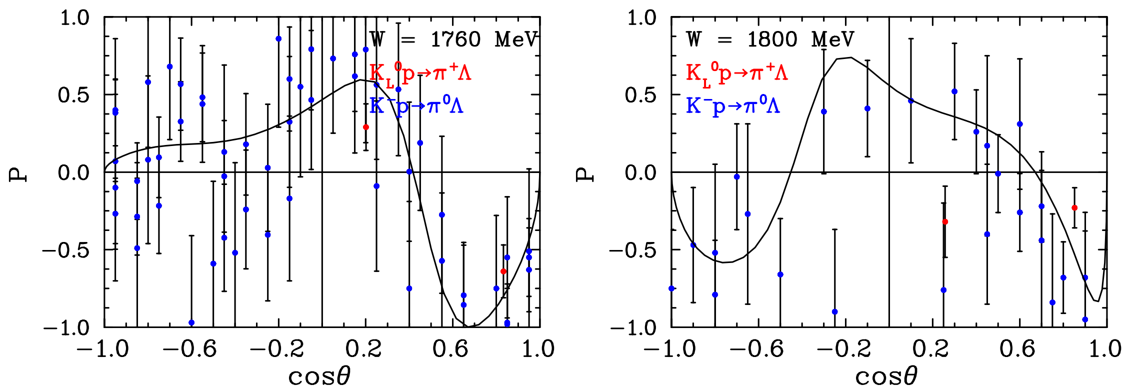


Figure 6: Comparison of selected polarization data for $K^-p \to \pi^0\Lambda$ and $K_Lp \to \pi^+\Lambda$ at W = 1760 MeV and 1880 MeV, from Ref. [61]. The plotted points from previously published experimental data are those data points within 20 MeV of the Kaon c.m. energy indicated on each panel [58]. The curves are from the recent PWA of $K^-p \to \pi^0\Lambda$ data [62, 63].

### 6.3 $\pi\Sigma$ Final States

The $SU(3)$ flavor symmetry allows as many $S = -2$ baryon resonances, as there are $N$ and $\Delta$ resonances combined ($\sim 27$); however, until now only three ground states $\Xi(1382)1/2^+$, $\Xi(1538)4/2^+$, and $\Xi(1820)3/2^-$ have their quantum numbers assigned and few more states have been observed [1].

The amplitudes for reactions leading to $\pi\Sigma$ final states are

$$T(K^-p \to \pi^-\Sigma^+) = -\frac{1}{2}T^1(\overline{K}N \to \pi\Sigma) - \frac{1}{\sqrt{6}}T^0(\overline{K}N \to \pi\Sigma), \quad (16)$$

$$T(K^-p \to \pi^+\Sigma^-) = \frac{1}{2}T^1(\overline{K}N \to \pi\Sigma) - \frac{1}{\sqrt{6}}T^0(\overline{K}N \to \pi\Sigma), \quad (17)$$

$$T(K^-p \to \pi^0\Sigma^0) = \frac{1}{\sqrt{6}}T^0(\overline{K}N \to \pi\Sigma), \quad (18)$$

$$T(K_L^0p \to \pi^+\Sigma^0) = -\frac{1}{2}T^1(\overline{K}N \to \pi\Sigma), \quad (19)$$

$$T(K_L^0p \to \pi^0\Sigma^+) = \frac{1}{2}T^1(\overline{K}N \to \pi\Sigma). \quad (20)$$

Figure 7 shows a comparison of differential cross section data for $K^-p$ and $K_Lp$ reactions leading to $\pi\Sigma$ final states at $W = 1660$ MeV (or $P_{\rm lab} = 716$ MeV/$c$). The curves are based on energy-dependent isospin amplitudes from a recent PWA [62, 63]. No differential cross section data are available for $K_Lp \to \pi^0\Sigma^+$. As this example shows, the quality of the $K_Lp$ data is comparable to that for the $K^-p$ data. It would therefore be advantageous to combine the $K_Lp$ data in a new coupled-channel PWA with available $K^-p$ data. Note that the reactions $K_Lp \to \pi^+\Sigma^0$ and $K_Lp \to \pi^0\Sigma^+$ are isospin selective (only $I = 1$ amplitudes are involved) whereas the reactions $K^-p \to \pi^-\Sigma^+$ and $K^-p \to \pi^+\Sigma^-$ are not. New measurements with a $K_L$ beam would lead to a better understanding of $\Sigma^*$ states and would help constrain the amplitudes for $K^-p$ scattering to $\pi\Sigma$ final

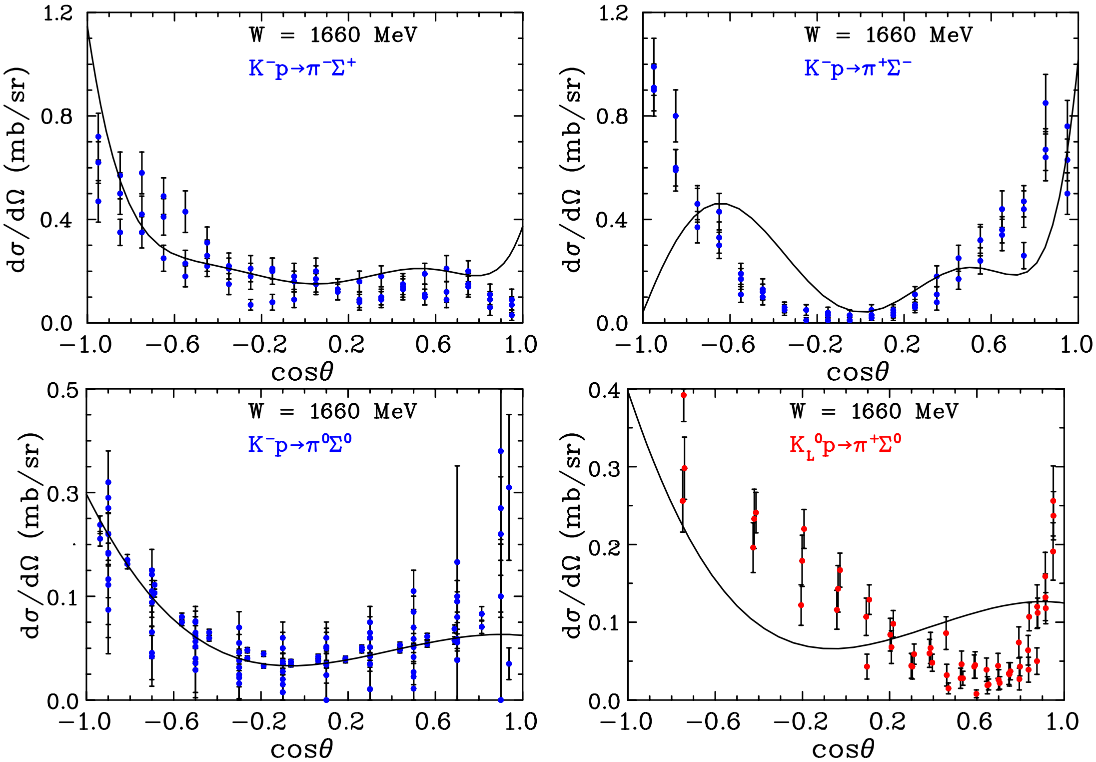


Figure 7: Comparison of selected differential cross section data for $K^-p \to \pi^-\Sigma^+$, $K^-p \to \pi^+\Sigma^-$, $K^-p \to \pi^0\Sigma^0$, and $K_Lp \to \pi^0\Sigma^+$ at W = 1660 MeV, from Ref. [61]. The plotted points from previously published experimental data are those data points within 20 MeV of the Kaon c.m. energy indicated on each panel [58]. The curves are from the recent PWA of $K^-p \to \pi\Sigma$ data [62, 63].

states.

## 6.4 $K\Xi$ Final States

The amplitudes for reactions leading to $K\Xi$ final states are

$$T(K^-p \to K^0\Xi^0) = \frac{1}{2}T^1(\overline{K}N \to K\Xi) + \frac{1}{2}T^0(\overline{K}N \to K\Xi), \quad (21)$$

$$T(K^-p \to K^+\Xi^-) = \frac{1}{2}T^1(\overline{K}N \to K\Xi) - \frac{1}{2}T^0(\overline{K}N \to K\Xi), \quad (22)$$

$$T(K_Lp \to K^+\Xi^0) = -\frac{1}{\sqrt{2}}T^1(\overline{K}N \to K\Xi). \quad (23)$$

The threshold for $K^-p$ and $K_Lp$ reactions leading to $K\Xi$ final states is fairly high ($W_{\text{thresh}} = 1816$ MeV). In Fig. 8(right)(left), we present the cross section for $\Xi$ production using a $K^-$-beam [66]. There are no differential cross section data available for $K_Lp \to K^+\Xi^0$ and very few (none recent) for $K^-p \to K^0\Xi^0$ or $K^-p \to K^+\Xi^-$. Measurements for these reactions would be very helpful, especially for comparing with predictions from dynamical coupled-channel (DCC) models [64, 65]. The *Review of Particle Physics* [1] lists only two states with branching fractions (BF) to $K\Xi$, namely, $\Lambda(2100)7/2^-$ (BF $<$ 3%) and $\Sigma(2030)7/2^+$ (BF $<$ 2%).

## 6.5 $KK\Omega$ Final States

The experimental situation with $\Omega^{-*}$s is even worse than the $\Xi^*$ case, there are very few data for excited states. The reason for such a scarce dataset in the multi-strange hyperon domain is mainly due to very low cross section in indirect production with pion or in particular photon beams. In Fig. 8(right), we present the cross section for $\Omega$ production using a $K^-$-beam [66].

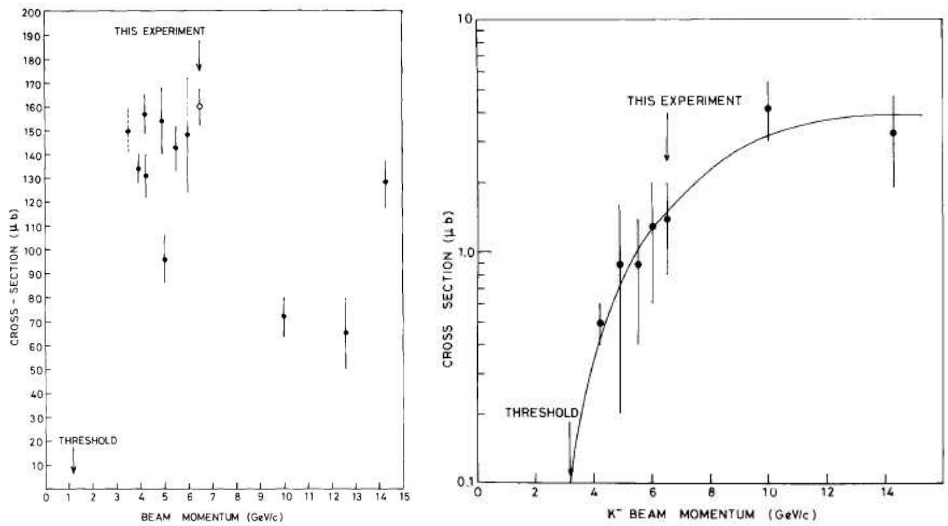


Figure 8: Left panel: Cross section of $\Xi^-$ production, $K^-p \to \Xi^-X$, as a function of $K^-$ momentum [66]. Right panel: Cross section of $\Omega^-$ production, $K^-p \to \Omega^-K^+K^0$, as a function of $K^-$ momentum [66]. The curve is a fit by eye to the data.

A major effort in LQCD calculations involves the determination of inelastic and multi-hadron scattering amplitudes, and the first calculation to study an inelastic channel was recently performed [67, 68]. For lattice calculations involving baryons that contain one or more strange quarks an advantage is that the number of open decay channels is generally smaller than for baryons comprised only of the light $u$ and $d$ quarks.

## 6.6 Summary for PWA

Pole positions have been determined (no uncertainties) for several $\Lambda^*$s and $\Sigma^*$s but information about pole positions has not been determined for $\Xi$ or $\Omega$ hyperons [1]. Our plan is to do a coupled-channel PWA with new GlueX KLF data in combination with available and new J-PARC $K^-p$ measurements when they will be available. Then the best fit will allow the determination of data-driven (model independent) partial-wave amplitudes and associated resonance parameters (pole positions, residues, BW parameters, and so on. Additionally, PWAs with new GlueX data will allow a search for "missing" hyperons via looking for new poles in complex plane positions. It will provide a new benchmark for comparisons with QCD-inspired models and LQCD calculations.

# 7 Analysis of Three Body Final States

The understanding baryon properties is hardly possible without analysis of reactions with two mesons in the final state. Already in the mass region above 1600 MeV the excited $\Lambda$-hyperons decay strongly into the $\Sigma(1385)\pi$ [69, 70] final state while the $\Sigma$-hyperons decay strongly into the $\Sigma(1385)\pi$ [69] and $\Lambda(1405)\pi$ [71] channels. Above 1800 MeV almost all known $\Lambda$ and $\Sigma$ hyperons have the dominant decay mode defined by the production of the vector meson $K^*(890)$ [70]. In the $\Sigma$-sector number of resonances were seen in the analysis of the $\Delta(1230)\bar{K}$ final state. It is natural to expect the decay of $J^P = 3/2^+$ states into the $\Lambda(1520)\pi$ [72] channel.

The reactions with two meson final states provide a vital information for the analysis of single meson production reactions. The singularities which correspond to the opening of the resonance-meson threshold (branching points) can produce structures in other channels which can simulate a resonance-like signal [73]. Let us mention that the situation is notably more severe in the hyperon sector than in the sector of non-strange baryons. Due to rather small widths of low mass excited hyperons and meson resonances with $s$-quark such singularities are situated much closer to the physical region and can influence notably the data. Therefore a combined analysis of the channels with single and two-mesons in the final state is a must for the search of the missing resonances.

The combined analysis should help to understand the structure of the resonances with masses up to 2.5 GeV and their decay properties. One of the important task is to find nonet partners of the nucleon states observed in the photo-production reactions in the mass region around 1900 MeV [74]. These states have strong couplings to the $\rho(770) - N$ final state and it is naturally to expect that their hyperon partners can be found in the analysis of the $K^*(890) - N$ channel.

The analysis of the three body final state should be done in the framework of the event-by-event maximum likelihood method which allows us to take into account all amplitude correlations in the multidimensional phase space. It is very important to extract the polarization observables from the decay of the final hyperons in the $KN \to \Lambda\pi\pi$ and $KN \to \Sigma\pi\pi$ reactions. One of a possible simplification can be connected with an extraction of the $K^*(890)N$ state from the $KN \to K\pi N$ reaction where analysis can be done in the framework of the density matrix elements approach. However, the analysis should take into account the rescattering of the particles in the final state: triangle diagrams which leads to the logarithmic singularities in the scattering amplitude. Due to small widths of the intermediate states such singularities can play a more important role than in the case of nucleon and $\Delta$-excitations. It would be also very important to include in the analysis the CLAS photoproduction data with $K\pi\Lambda$ and $K\pi\Sigma$ final states: there is a chance to observe states with a small $KN$ coupling in these reactions.

# 8 Determination of Pole Position

In spite of their model and reaction dependence, partial-wave Breit-Wigner parameters have in hadron spectroscopy for quite some time been the preferred connection between experiment and QCD. However, since recently, they have been justifiably replaced with pole parameters as more, but still not completely model independent quantities, and this fact has also been recognized by the Particle Data Group (PDG) in their recent editions [1]. Therefore, the pole extraction from experimental data become the procedure of utmost importance.

Extraction of pole parameters is performed in two ways: (a) in an energy-dependent way (ED); or (b) in an energy-independent procedure through single-energy PWAs (SE). In an ED procedure (a) one measures as many observables as possible to be close to the complete set and then fits the observables with parameters of a well-founded theoretical model that describes the reaction in question. Continuity in energy is enforced by the features of the theoretical model. In a SE procedure (b) one again measures as many observables as possible but attempts to extract partial waves at an isolated single energy fit therefore eliminating any theoretical input. A discreet set of partial waves is obtained, and the issues of achieving continuity in energy have recently been extensively discussed either by introducing the constraints in analyticity [75] or through angle- and energy-dependent phase ambiguity [76].

In energy-dependent models, pole parameters have been extracted in various ways. The most natural way is the analytic continuation of theoretical model solutions into the complex energy plane. In spite of the fact that this method looks like a natural and only possible way, it has quite some drawbacks. First of all, analytic continuation of the analytic function is unique only if the function on the real axes is known up to the infinite precision in infinite number of points. As it is never, and can never be the case, analytic continuation is inherently model dependent. As it is also known that analytic continuation is in addition rather instable, other, alternative methods for pole identification have introduced. Simpler single-channel pole extraction methods have been developed such as the speed plot [77], time delay [78], the N/D method [79], regularization procedures [80], and Pade approximants [81], but their success has been limited. In single-energy analyses the situation is even worse: until recently for the extraction of pole parameters absolutely no adequate method has been available. All single-channel methods involve first- or higher-order derivatives, so partial-wave data had to be either interpolated or fitted with an unknown function, and that introduced additional, very often uncontrolled model dependencies.

That situation has recently been overcame when a new Laurent+Pietarinen method applicable to both, ED and SE models, has been introduced [82–86]. The driving concept behind the single-channel (and later multi-channel) L+P approach was to replace solving an elaborate theoretical model and analytically continuing its solution into the full complex energy plane, with a local power-series representation of partial-wave amplitudes with well defined analytic properties on the real energy axis, and fitting it to the given input. In such a way, the global complexity of a model is replaced by much simpler model-independent expansion limited to the regions near the real energy axis which is sufficient to obtain poles and their residues. We never claim that we know the solution of the true theoretical model, instead we only give the simplest analytic function with known analitic structure which fits the data. Formally, the introduced L+P method is based on the

Mittag-Leffler expansion[1] of partial-wave amplitudes near the real energy axis, representing the regular, but unknown, background term by a conformal-mapping-generated, rapidly converging power series called a Pietarinen expansion[2]. In practice we have represented the regular background part with three Pietarinen expansion series each representing the most general function having a branch point at $x_{bp}$ , and fitted all free parameters in our approach to the chosen channel input. The first Pietarinen expansion with branch-point $x_P$ was restricted to an unphysical energy range and represented all left-hand cut contributions, and next two Pietarinen expansions described background in the physical range with branch points $x_Q$ and $x_R$ defined by the analytic properties of the analyzed partial wave. A second branch point was usually fixed to the elastic channel branch point, and the third one was either fixed to the dominant channel threshold value or left free. Thus, solely on the basis of general physical assumptions about analytic properties of the fitted process (number of poles and number and position of conformal mapping branch-points) the pole parameters in the complex energy plane are obtained. In such a way, the simplest analytic function with a set of poles and branch points that fits the input is actually constructed. This method is equally applicable to both theoretical and experimental input[3], and represents the first reliable procedure to extract pole positions from experimental data, with minimal model bias.

The transition amplitude of the multi-channel L+P model is parametrized as

$$T^a(W) \;=\; \sum_{j=1}^{N_{pole}} \frac{g_j^a}{W_j - W} + \sum_{i=1}^{3} \sum_{k_i=0}^{K_i^a} c_{k_i}^a \left( \frac{\alpha_i^a - \sqrt{x_i^a - W}}{\alpha_i^a + \sqrt{x_i^a - W}} \right)^{k_i}, \tag{24}$$

where $a$ is a channel index, $W_j$ are pole positions in the complex $W$ (energy) plane, $g_i^a$ coupling constants. The $x_i^a$ define the branch points, $c_{k_i}^a$, and $\alpha_i^a$ are real coefficients. $K_i^a$, $i = 1, 2, 3$ are Pietarinen coefficients in channel $a$. The first part represents the poles and the second term three branch points. The first branch point is chosen at a negative energy (determined by the fit), the second is fixed at the dominant production threshold, and the third branch point is adjusted to the analytic properties of fitted partial wave.

To enable the fitting we define a reduced discrepancy function $D_{dp}$ as

$$\begin{aligned} D_{dp} &= \sum_{a}^{all} D_{dp}^a; \\ D_{dp}^a &= \frac{1}{2\,N_W^a - N_{par}^a} \times \sum_{i=1}^{N_W^a} \left\{ \left[ \frac{\mathrm{Re}\,T^a(W^{(i)}) - \mathrm{Re}\,T^{a,exp}(W^{(i)})}{Err_{i,a}^{\mathrm{Re}}} \right]^2 \right. \\ &+ \left. \left[ \frac{\mathrm{Im}\,T^a(W^{(i)}) - \mathrm{Im}\,T^{a,exp}(W^{(i)})}{Err_{i,a}^{\mathrm{Im}}} \right]^2 \right\} + \mathcal{P}^a, \end{aligned}$$

[1]Mittag-Leffler expansion [87] is the generalization of a Laurent expansion to a more-than-one pole situation. For simplicity, we will simply refer to this as a Laurent expansion.

[2]A conformal mapping expansion of this particular type was introduced by Ciulli and Fisher [88,89], was described in detail and used in pion-nucleon scattering by Esco Pietarinen [90, 91]. The procedure was denoted as a Pietarinen expansion by Höhler in [59].

[3]Observe that fitting partial wave data coming from experiment is even more favorable.

where

$$\mathcal{P}^a = \lambda^a_{k_1} \sum_{k_1=1}^{K^a} (c^a_{k_1})^2 \, {k_1}^3 + \lambda^a_{k_2} \sum_{k_2=1}^{L^a} (c^a_{k_2})^2 \, {k_2}^3 + + \lambda^a_{k_3} \sum_{m=1}^{M^a} (c^a_{k_3})^2 \, {k_3}^3$$

is the Pietarinen penalty function which ensure fast and optimal convergence. $N^a_W$ is the number of energies in channel $a$, $N^a_{par}$ the number of fit parameters in channel $a$, $\lambda^a_c, \lambda^a_d, \lambda^a_e$ are Pietarinen weighting factors, $Err^{\mathrm{Re,\,Im}}_{i,a}$..... errors of the real and imaginary part, and $c^a_{k_1}, c^a_{k_2}, c^a_{k_3}$ real coupling constants.

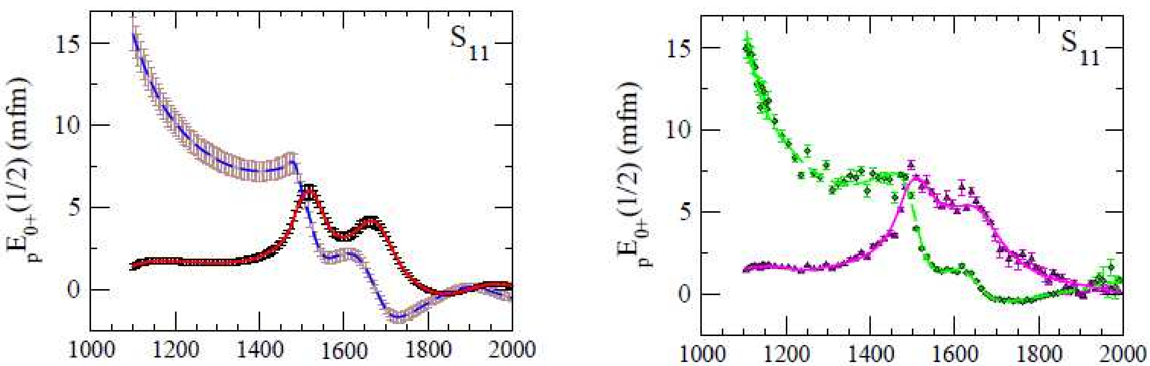


Figure 9: L+P fit to GWU/SAID CM12 pion photoproduction $_pE_{0+}$ ED and SE solutions [92].

In order to get reliable answers in L+P model we have to build the knowledge about analytic structure of the fitted partial wave into the fitting procedure. As we are looking for poles, we only have to define which branch-points to include. Their analytic form will be determined by the number of Pietarinen coefficients. As we have only three branch-points at our disposal we expect that the first branch-point will describe all subthreshold and left-hand cut processes, second one is usually fixed to the dominant channel opening, and the third one is to effectively represent background contributions of all channel openings in the physical range. So, in addition to choosing the number of relevant poles, our anticipation of the analytic structure of the observed partial wave is of great importance for the stability of the fit.

The L+P model is successfully applied to both, theoretical models and discreet partial-wave data. As an example, in Fig. 9, we give the achieved quality of the fit for the CM12 GWU/SAID pion photoproduction amplitudes [92].

In summary: Methods of described L+P model will be used for extraction of pole parameters for both, ED solutions obtained by the method described in Section 6, and SE solutions developed independently.

# 9 Statistics Tools for Spectroscopy of Strange Resonances

Several statistical aspects concerning the analysis of $K_L$ data are discussed in the following. The proposed experiment will be capable of producing a large body of consistent data, which is a prerequisite to carry out statistical analyses. So far, the data in the strangeness $S = -1$ sector were produced in many different experiments, often from the 80's or earlier, with different systematic uncertainties that are, moreover, unknown in many cases. The problems resemble the situation in pion-induced inelastic reactions [93, 94]. This makes any kind of analysis difficult but statistical tests, e.g., on the significance of a claimed resonance signal, are indispensable to carry out meaningful baryon spectroscopy. Indeed, the search for *missing resonances* is not only a problem of implementing physical principles such as unitarity in the amplitude, but, to a large extent a statistical one. This becomes especially relevant once one searches for states beyond the most prominent resonances.

## 9.1 Minimizing Resonance Content

Partial-wave analysis, discussed in Section 6 is needed to extract the physically relevant information from data. For resonance spectroscopy, one needs the energy dependence of the amplitude to determine resonance positions and widths. Therefore, energy-dependent (ED) parametrizations of the partial waves are fitted either to data or to single-energy (SE) solutions, generated by conducting partial-wave analysis in narrow energy windows. The resonance content is usually determined by speed-plot techniques or analytic continuation of the ED parametrization to complex scattering energies, where resonances manifest themselves as poles [95].

Yet, the ED parametrization itself contains, almost always, resonance plus background terms in one implementation or another. A problem arises if resonance terms are needed to model missing background dynamics. Then, false positive resonance signals could be obtained [96]. Adding resonance terms will always lower the $\chi^2$ in a given fit, but the question is how significant this change is.

We plan to address this well-known, yet poorly addressed problem by applying several statistical analysis tools to the amplitude parametrization. Some techniques have been used, so far, to address this problem. For example, in so-called mass scans, the $\chi^2$ dependence on the mass of an additional resonance is studied [97, 98]. If, potentially in many reaction channels at once, the $\chi^2$ drops by a certain amount at some energy, a resonance state might be responsible.

Beyond mass scans, there exist *model selection* techniques referring to the process of selecting the simplest model with the most conventional explanation. Here, the conventional/simple explanation is an (energy-dependent) background and/or threshold cusps, while the algorithm should penalize unconventional explanations such as resonances.

Minimizing the resonance content in a systematic way is thus a goal within partial-wave analysis. For this, the Least Absolute Shrinkage and Selection Operator (LASSO) technique for model selection can be applied (which provides a Bayesian posterior-mode estimate), in combination with cross validation and/or information theory to control the size of the penalty parameter $\lambda$ [99–101].

The combination of these techniques effectively suppresses the emergence of resonances except for those really needed by the data. The numerical implementation is especially simple because it affects only the calculation of the $\chi^2$. Trial-and-error techniques, sometimes still applied to check for resonances in different partial waves, will become obsolete. Here, one simply starts with an over-complete resonance set plus flexible backgrounds, and the algorithm will remove all those resonances not needed by data, without manual intervention. Apart from cross validation, we will also consider information theory to regulate $\lambda$ as proposed in Ref. [102]. In particular, the Akaike and Bayesian information criteria provide easy-to-use model selection. Results should be independent of the choice of the criterion.

In 2017, the LASSO technique was, for the first time, used in pion photoproduction at low energies for the "blindfolded" selection of the relevant multipoles and their simplest parametrization to describe the available data [103]. The analysis of kaon-induced reactions is closely related. For a recent application in a different but related context see Ref. [104]. Once the model selection process is finished, uncertainties on resonance parameters can be obtained by the usual re-sampling techniques.

The existing and proposed partial-wave analysis tools use different construction principles: resonances are included in the form of bare states, $K$-matrix poles, or generated from hadron dynamics itself. For the first two classes of approaches, one has at one's disposal the coupling constants that tune the interaction of a bare singularity with the meson-baryon continuum. Those are fit parameters that can explicitly be included in the penalization term. If resonances are generated from the meson-baryon dynamics itself, the case is a bit more complicated, because there are no directly accessible tuning parameters. This parametrization, practiced by the GW/SAID group for many years (see, e.g., Ref. [105]), is, in principle, the cleanest analysis tool, because resonance generation does not require manual intervention. Yet, even here the emergence of resonance terms can be penalized, e.g., through the value of contour integrals on the second Riemann sheet where resonance poles are located (a value of zero corresponds then to the absence of poles).

It should be stressed that the information theory criteria do *not* require a good fit in a frequentist's sense because they merely compare the relative quality of models. This is especially relevant when it comes to the analysis of many different data sets (such as kaon-induced reactions) in which, e.g., the systematic errors might be underestimated such that a $\chi^2/\mathrm{d.o.f.} \approx 1$ is difficult to achieve.

Systematic uncertainties can be treated as in the GW/SAID approach [60] in which the $\chi^2$ is defined as

$$\chi^2 = \sum_i \left(\frac{N\Theta_i - \Theta_i^{\mathrm{exp}}}{\epsilon_i}\right)^2 + \left(\frac{N-1}{\epsilon_N}\right)^2, \tag{25}$$

where $\Theta_i^{\mathrm{exp}}$ is an experimental point in an angular distribution and $\Theta_i$ is the fit value. Here the overall systematic error, $\epsilon_N$, is used to weight an additional $\chi^2$ penalty term due to renormalizaton of the fit by the factor $N$. The statistical error is given by $\epsilon_i$. Note that the fit function is penalized, rather than the data, to avoid the bias discussed in Ref. [106]. See also Ref. [107] for a further discussion of the topic.

## 9.2 Goodness-of-Fit Tests

The $\chi^2$ per degree of freedom, $\chi^2_{d.o.f.}$, is usually considered as a criterion for a good fit, but becomes meaningless if thousands of data points are fitted (and should be replaced by Pearson's $\chi^2$ test). Statistical $\chi^2$ tests will become possible through the new data, putting resonance analysis on a firmer ground. While $\chi^2$ tests are sensitive to under-fitting, they are insensitive to over-fitting. Here, the $F$-test [108] is suitable to test the significance of new fit parameters. That test, can, thus, be applied to reduce the number of internal parameters in partial-wave parametrization, resulting in more reliable estimates of uncertainties of extracted resonance parameters, such as masses, widths, and hadronic branching ratios.

With increased consistency of data through the KLF experiment, other goodness-of-fit criteria can also be applied, such as Smirnov-Kolmogorov or Anderson-Darling tests for normality [109, 110] or run tests from non-parametric statistics. For pion photoproduction, these tests are applied and extensively discussed in Ref. [103].

A prerequisite to carry out classical statistical tests is data consistency. As discussed before, this is unfortunately not always the case in the $S = -1$ sector. The KLong experiment will produce, for the first time, a body of measurements large enough to enable such tests reliably.

## 9.3 Representation of Results

As mentioned, ED parametrizations are needed to extract resonance parameters, but single-energy (SE) fits are useful to search for narrow structures, or for other groups to test theoretical models of hadron dynamics. The question arises how the partial waves can be presented to allow the theory community to carry out their fits. As recently demonstrated [111], SE solutions by themselves carry only incomplete statistical information, mainly because they are correlated quantities. We plan to provide the analysis results in a similar form as recently done in Ref. [111] for elastic $\pi N$ scattering. With this, the theory community can fit partial waves through so-called *correlated $\chi^2$ fits* obtaining a $\chi^2$ close to the one obtained in a fit directly to data (see Ref. [111] for an extended discussion). This format ensures that the maximal information from experiment is transmitted to theory, allowing to address the *missing resonance problem* in the wider context of questions related to confinement and mass generation, that have been paramount problems in hadronic physics for decades.

<u>In summary:</u> With a large consistent data set from the KLF experiment, an entire class of statistical tools will become applicable that is needed to conduct rigorous baryon spectroscopy. With the new data, the quantitative significance of resonance signals and the quantitative uncertainties of resonance parameters can be determined.

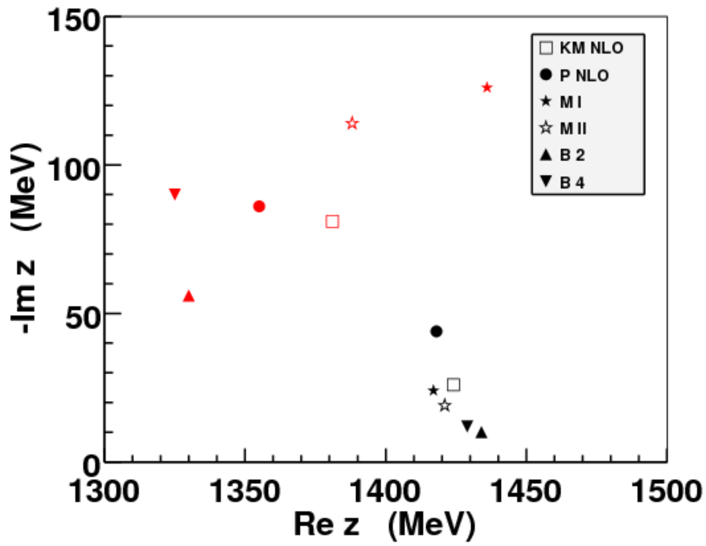


Figure 10: Pole positions for chiral unitary approaches - $KM$ from Ref. [115], $B$ from Ref. [114], $M$ from Ref. [116] and $P$ from Ref. [117] as compared in Ref. [118]. Each symbol represents the position of the first (black) and second (red) pole in each model.

## 10 Theory for "Neutron" Target Measurements

Antikaon-nucleon scattering is predominantly analyzed in the so-called coupled-channel Chiral Unitary approaches (UChPT). These models successfully describe the properties of the sub-threshold resonance in the isospin $I = 0$ channel, the $\Lambda(1405)1/2^-$. Furthermore, such models lead to the prediction that the scattering amplitude has two poles in the complex energy plane for the quantum numbers of this resonance ($I = 0, L = 0, S = -1$). This coins the so-called the two-pole structure of the $\Lambda(1405)$, see the current review by the Particle Data Group [1] for more details.

In the most recent formulation, the aforementioned UChPT approaches rely on a chiral amplitude for the meson-baryon scattering up to next-to-leading chiral order. Whereas the unitarity constraint is usually imposed via the Bethe-Salpeter equation either in the full off-shell formulation [112,113] or in the so-called on-shell approximation, e.g, [114–116]. For the analysis of data the former is quite intricate, while as it was shown in [113] the off-shell effects are rather small. Therefore, it is meaningful to use the latter formulation. Recently, a direct quantitative comparison of the on-shell models [114–117] was performed in Ref. [118]. It was found there that various models, which typically have many free parameters, adjusted to the same experimental data, predict very different behavior of the scattering amplitude on and off the real energy-axis. This systematic uncertainty becomes evident, when comparing the pole positions of the $\Lambda(1405)$ in these models (see Fig. 10). The position of the narrow (first) pole seems to be constrained at least in the real part rather well, while the predictions for the position of the broad (second) pole cover a very wide region of the complex energy-plane. This uncertainty is present even within models of the same type. This ambiguity can be traced back to the fact that the experimental data used to fix the parameters of the models are rather old and imprecise. It is expected that the proposed experiment with $K_L$ beams

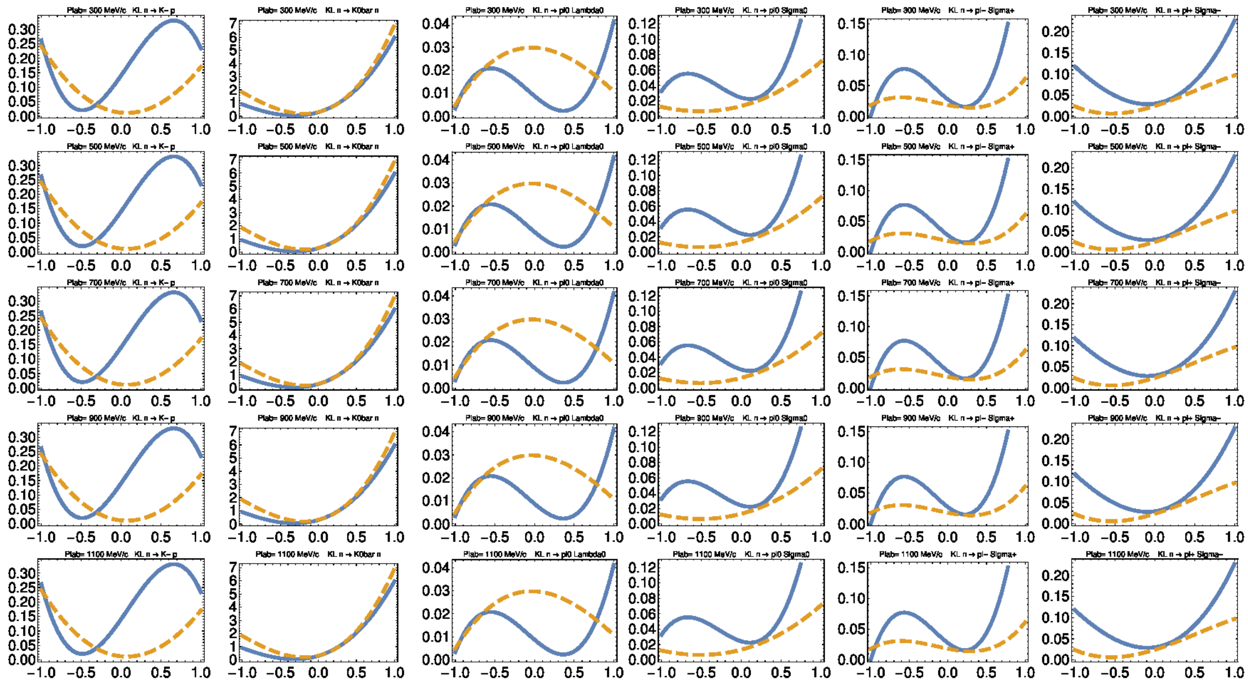

Figure 11: Theoretical predictions for differential cross sections, $d\sigma/d\Omega$, for reactions (columns) $K_L n \to K^- p$, $K_L n \to \bar{K}^0 n$, $K_L n \to \pi^0 \Lambda$, $K_L n \to \pi^0 \Sigma^0$, $K_L n \to \pi^- \Sigma^+$, and $K_L n \to \pi^+ \Sigma^-$ as a function of c.m. $\cos$ of production angle. Each row associated with kaon lab-momentum of 300, 400,... 1000 MeV/$c$ of initial neutral kaon beam. Orange dashed and blue solid lines show predictions withim Model-B2 and Model-B4, respectively (see text for details).

will lead to an improvement of this situation, as it will be described below.

The $K_L$ beam can be scattered on a "neutron" target, while measuring the strangeness $S = -1$ final meson-baryon states (see, e.g., Sec. 6). In such a setup, the proposed experiment can become a new and very strongly desired new source of experimental data to pinpoint the properties of the antikaon-nucleon scattering amplitude. To make this statement more quantitative we compare predictions of both solutions of the model[4] from Ref. [114]. These solutions agree with all presently available scattering, threshold as well as the photoproduction data for the $\Sigma\pi$ line shapes by the CLAS Collaboration [119]. The predicted differential cross sections ($d\sigma/d\Omega$) as well as polarized ones ($Pd\sigma/d\Omega$) for the $K_L n$ scattering with the final states $K^- p, \bar{K}^0 n, \pi^0 \Lambda, \pi^{0/+/-}\Sigma^{0/-/+}$ are presented in Figs. 11 and 12, respectively. There is very little agreement on the prediction of these observables in the energy range aimed to study in the proposed $K_L$ experiment. The latter is very encouraging, meaning that the actual data can sort out one (or maybe both) solutions as unphysical, which was not possible by the present experimental data.

In summary, the proposed KLF experiment will lead to new constraints on the antikaon-nucleon models. Thus, this data will allow to sharpen our understanding of the long debated nature of

[4] The choice of this model for the present analysis is justified by the fact that it includes the p-wave interaction in the kernel of the Bethe-Salpeter equation explicitly.

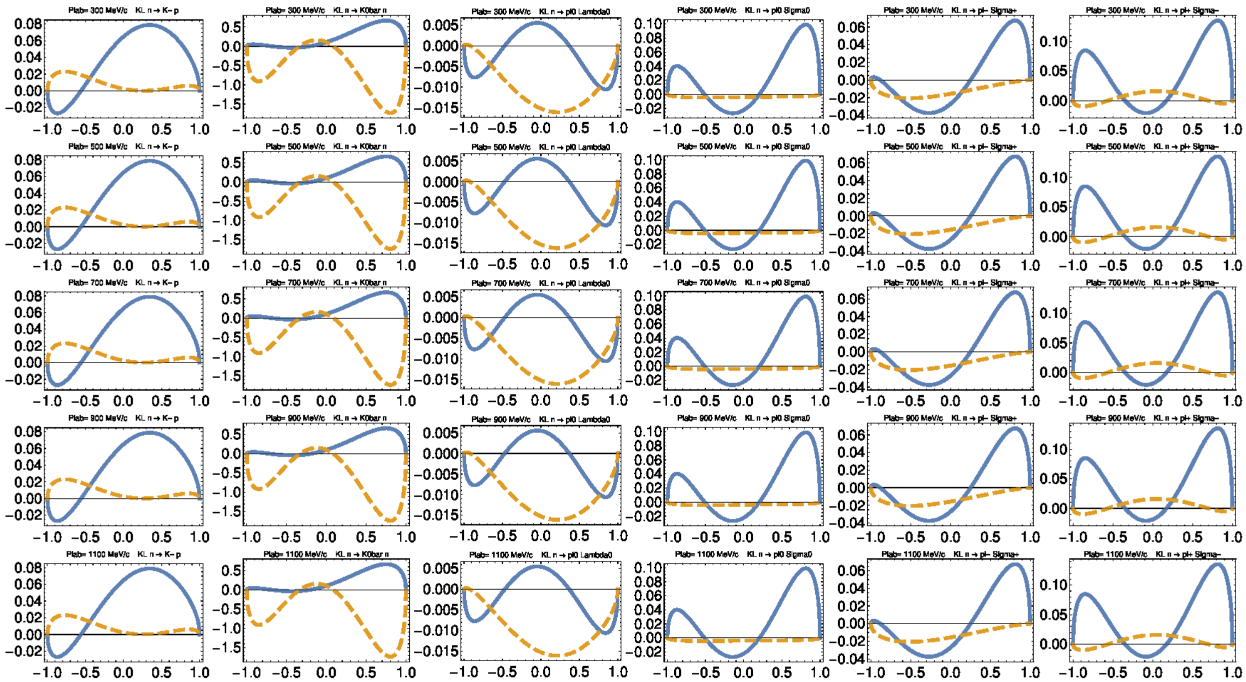

Figure 12: Theoretical predictions for polarized differential cross sections, $Pd\sigma/d\Omega$. The notation is the same as in Fig. 11.

strangeness $S = -1$ resonances.

## 11 Strange Meson Spectroscopy: $K\pi$ Interaction

The main source of our knowledge of kaon scattering amplitudes comes from kaon beam experiments at SLAC in the 1970s and 80s. The scattering amplitudes for $\pi K$ final state were extracted from reactions using a proton target by extrapolating to small momentum transfer, *t*, dominated by nearly-on-shell pion exchange. Phase-shift analysis of the flavor exotic isospin-3/2 amplitudes extracted from $K^+p \to K^+\pi^+n$ and $K^-p \to K^-\pi^-\Delta^{++}$ reactions by Estabrooks *et al.* [120] indicates a weak repulsive interaction in S-wave and very weak attractive interactions in P-wave and higher waves. In isospin-1/2, in addition to Estabrooks *et al.*, there is a considerable set of $\pi K$ scattering data provided by LASS experiment [121]. Reactions with the final states $\pi K$, $\eta K$ and $\pi\pi K$ final states have been measured. In the PWA of $\pi K \to \pi K$, a peaking amplitude in S-wave is interpreted as a broad $K^*(1430)$ resonance which appears to saturate unitarity. The narrow elastic vector resonance, $K^*(892)$, manifests itself as a rapid rise in the P-wave phase-shift. The D-wave amplitude has a peak, well below the unitarity limit, that can be interpreted as an inelastic $K_2^*(1430)$ resonance. Further resonances in the "natural parity" series ($J^P = 3^-, 4^+$, and $5^-$) are observed at higher energies.

The $\eta K$ is another inelastic channel to open, but LASS reports no significant amplitude into $\eta K$

for $W < 2$ GeV in S, P, and D waves. Indeed the inelasticity in P, D-waves and higher appears to come first from $\pi\pi K$ final state, where a significant amplitude is seen in $1^-$ above 1.3 GeV and a peak in $2^+$ at the $K_2^*(1430)$. The $\pi\pi K$ also couples to the "unnatural parity" series, notably to $J^P = 1^+$, where peaking behavior is observed that is commonly described in terms of two axial resonances, $K_1(1270), K_1(1400)$. Much higher statistics is needed to improve our knowledge on all these states.

Recently lattice QCD studies with $m_\pi = 391$ MeV were performed to search for resonances in coupled $\pi K$ and $\eta K$ scattering [67]. Scalar $\pi\pi/\overline{K}K$ and $K\pi/K\eta$ form factors have been calculated within a variety of approaches using (unitarized) chiral perturbation theory [122–129] and dispersion relations [128, 130, 131], in many cases using the former to constrain polynomial ambiguities of the latter.

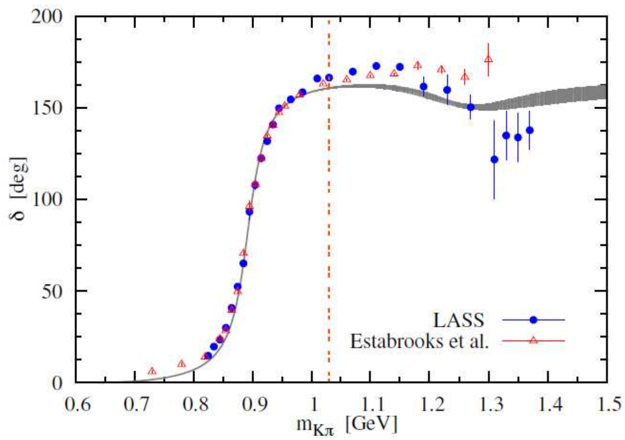


Figure 13: I=1/2 $K\pi$ scattering P-wave phase shift together with experimental results from LASS [121] and Estabrooks *et al.* [120]. The opening of the first inelastic $\pi K^*$ channel is indicated by dashed vertical line. The grey band represents the fit results from Boito *et al.* [136].

The study of $\pi K$ scattering provides a possibility not only to study scalar and vector $K^*$ states, including S-wave $\kappa(800)$ state (see [132, 133]), which is not yet well established, but it is also necessary to get precise vector and scalar $\pi K$ form factors as an input for extraction of Cabibbo-Kobayashi-Maskawa (CKM) matrix element $V_{us}$ from $\tau \to K\pi\nu$ decay. $\pi K$ scattering amplitudes with high precision are needed to study CP violation from Dalitz plot analyses of both open charm D-mesons [134] and charmless decay of B-mesons [135] into $K\pi\pi$ final state.

In Fig. 13, we present the phase of the form factor $F_+(s)$ with experimental results of LASS Estabrooks [120, 121] together with the fit of Boito *et al.* to $\tau$ decay data [136].

As one can see first of all experimental data obtained at SLAC have very poor statistics above 1.2 GeV and secondly do not span to higher energies which are even more important for B-meson decays. Moreover direct comparison of charged $K^\pm\pi^\mp$ with $\tau$ assumes isospin invariance as in the $\tau$ decay one has $K_s\pi^\pm$ final state depending on the sign of $\tau$ lepton.

Similrarly, as one can see from the following Figure 14, $I = 1/2$ and $I = 3/2$ S-wave, and $I = 3/2$ P-wave phase shifts are very poorly measured and need more experimental data.

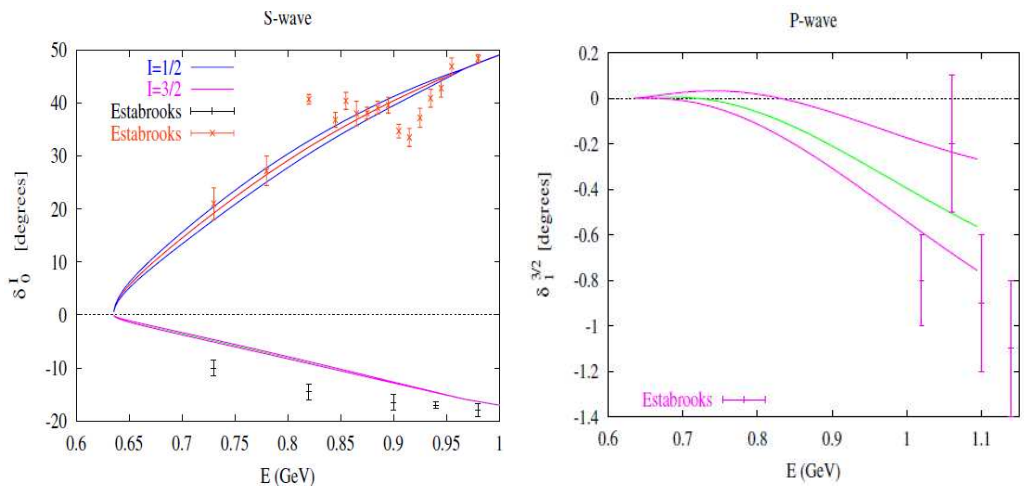


Figure 14: Left panel: $I = 1/2$ S-wave phase shift (curves and data in the upper half of the figure) and the $I = 3/2$ S-wave phase shift (curves and data in the lower half). Experimental data are from SLAC experiments as in previous figure. The curves are obtained from central, upper and lower values of parameters in the Roy-Steiner solutions ellipse [137]. Right panel: Same as in previous figure for $I = 3/2$. Data points are from Estabrooks *et al.* [120].

Significantly more intensive beam flux of proposed $K_L$ beam will provide high statistics data on both charged $K\pi$ as well as with final state neutral kaon in reactions:

- $K_Lp \to K^{\pm}\pi^{\mp}p$ (simultaneously measurable with $K_L$ beam).
- $K_Lp \to K_s\pi^+n$ on a proton target *for the first time*.
- $K_Ln \to K_s\pi^-p$ on a deuteron target *(for the first time)*.

In summary: Experimental data obtained in the proposed experiment with $K_L$ beam at JLab will provide valuable data to search for yet not well understood and possibly incomplete scalar, vector and tensor resonances in strange sector through a phase-shift analysis of $\pi K$ and $\eta K$ scattering amplitudes.

# 12 Proposed Measurements

We propose to use the KL Facility with the GlueX spectrometer, in JLab Hall D, to perform precision measurements of $K_Lp \to KY$ from liquid hydrogen and deuterium cryotarget ($LH_2/LD_2$) in the resonance region, $W = 1490$ – 4000 MeV and c.m. $\cos\theta$ from $-0.95$ to 0.95. It will operate at a neutral kaon flux of $3 \times 10^4$ $K_L/s$. The ability of GlueX to measure over wide ranges in $\theta$ and $\phi$ with good coverage for both charged and neutral particles, together with the $K_L$ energy information from the KL Facility, provide an ideal environment for these measurements.

## 12.1 $K_L$ Beam in Hall D

A schematic view of the Hall D beamline for KLF is presented in Fig. 15. At the first stage, $E = 12$ GeV electrons produced at CEBAF will scatter in a radiator at CPS, generating intensive beam of bremsstrahlung photons (we will not need in the Hall D Broadband Tagging Hodoscope). At the second stage, bremsstrahlung photons, created by electrons at a distance about 75 m upstream, hit the Be target, located in the cave, and produce neutral kaons along with neutrons and charged particles. Finally, $K_L$s will reach the $LH_2/LD_2$ cryotarget within GlueX settings.

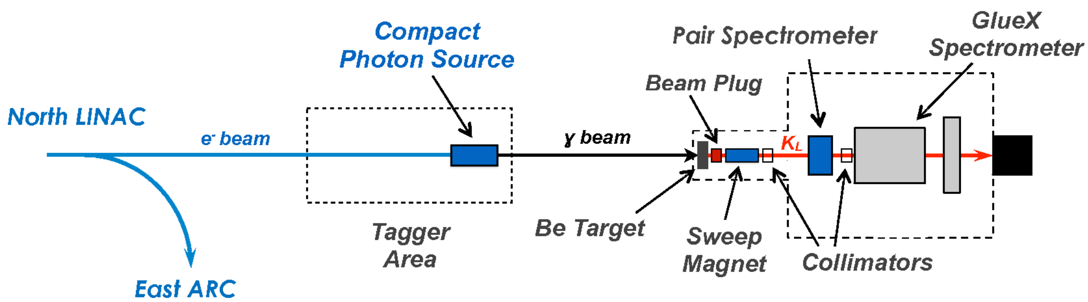


Figure 15: Schematic view of Hall D beamline on the way $e \to \gamma \to K_L$. Electrons are hitting the tungsten radiator, then photons are hitting the Be target, and, finally, neutral kaons are hitting the $LH_2/LD_2$ cryotarget. Main components are CPS, Be target, with beam plug, sweeping magnet, and pair spectrometer. See text for an explanation.

Our calculations have been performed for Jefferson Lab Hall D setup geometry. Primary $K_L$-production target has been placed in Hall D collimator cave. For the target material, we selected beryllium as for thick targets $K_L$-yield roughly proportional to the radiation length and density, which gives beryllium as the best candidate. Beam plug and sweeping magnet are placed right after the target. For our calculations, we took a simple beam plug: 15 cm thick piece of lead. Sweeping magnet is cleaning up charged component and has a field integral 2 Tesla·meter, which is enough to remove all charged background coming out of the beam plug. Vacuum beam pipe has 7 cm diameter and preventing neutron rescattering in air. Where are two collimators: one placed before the wall between collimator cave and experimental hall, another - in front of the Hall D detector. Distance between primary Be target and $LH_2/LD_2$ target (located inside Hall D detector) has been taken 16 m in our calculations, it can be increased upto 20 m.

### 12.1.1 Compact Photon Source: Conceptual Design

An intense high energy gamma source is a prerequisite for the production of the $K_L$ beams needed for the new proposed experiments at Hall D [138]. Here we describe a new approach to designing such photon sources. A possible practical implementation adjusted to the parameters and limitations of the available infrastructure is discussed. The vertical cut of the Compact Photon Source (CPS) model design, and the plan view of the present Tagger vault area with CPS installed are shown in Fig. 16.

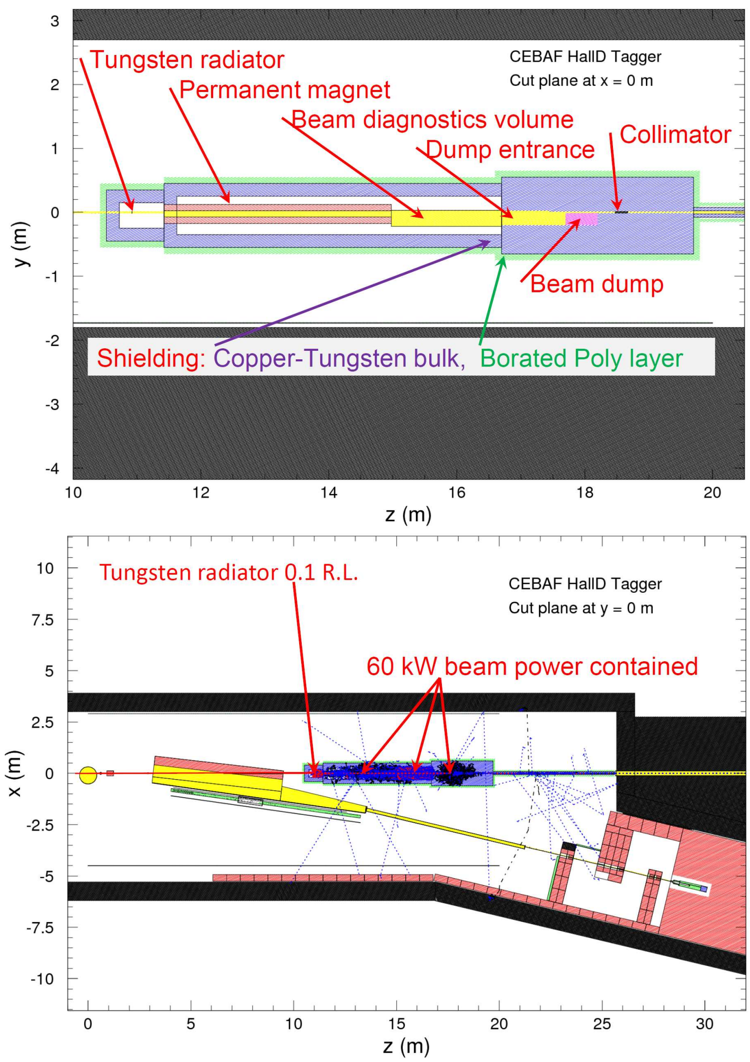


Figure 16: Elements of the design are indicated in the top panel (Vertical cut plane of the GEANT3 model of the CPS). The bottom panel shows the CPS assembly in the Tagger vault and simulations of 2000 beam electrons at 12 GeV.

The new design combines in a single properly shielded assembly all elements necessary for the production of the intense photon beam, such that the overall dimensions of the setup are limited and the operational radiation dose rates around it are acceptable. Compared to the alternative, the proposed CPS solution presents several advantages, including much lower radiation levels, both prompt and post-operational due to the beam line elements' radioactivation at the vault; much less disturbance of the available infrastructure at the Tagger Area and better flexibility in achieving high-intensity photon beam delivery to Hall D. The new CPS solution will satisfy proposed $K_L$ beam production parameters; we do not envision big technical or organizational difficulties in the implementation of the conceptual design.

The new setup utilizes the Hall D Tagger vault, properly shielded by design to accomodate the medium power beam dump capable of accepting up to 60 kW of 12 GeV beam, assuming the proper local shielding is set around the dump. The presently installed dump is shielded behind the iron labyrinth walls, and is surrounded by a massive iron shielding, made of iron blocks available at the time of construction. The present setup is optimized for operations using very thin radiators producing relatively low intensity photon beam such that the beam electrons losing energy to photon production in the radiator may be detected and counted in the tagger hodoscope counters. The present setup is not suitable for production of massively more intense photon beams needed for the $K_L$ production, due to the expected overwhelming radiation and activation levels in the vault.

The new proposed CPS solution solves the problem by incorporating the new thick radiator and the new beam dump in one assembly installed along the straight beam line exiting from the tagger magnet (presently the line is used as the photon beam line). The new CPS device should be capable of taking the same beam power of 60 kW, using optimized shielding made of high-Z material, which would make the necessary equivalent shielding compact, requiring less total weight of the shielding. Qualitatively, if one needs a sphere of iron (8 g/cm$^3$) of 2 m radius for the shielding, it may be roughly replaced by a sphere of 1 m radius made of tungsten-copper (16 g/cm$^3$), with its weight actually four times smaller. The optimized design is shown to be able to limit the prompt radiation dose rates around the CPS to the present operational levels, also significantly limiting the post-operational doses around the heavily shielded assembly. Of course, the inner parts of the CPS device will be activated to high levels, preventing immediate access and disassembly, so the engineering requirements to the reliability of all parts inside must be strict. The overhead shielding at the CPS location in the tagger vault is about the same thickness (13 feet) of concrete and berm as at the present dump location. It will keep the radiation doses outside and at the CEBAF boundary within the design limits for the site.

The proposed CPS solution is just conceptual, and full cycle of engineering design is required before the final optimized solution is found. The cost and space limitations will determine the choice of sielding materials for the CPS. Details of the dump and magnet design also will be included in the overall optimization process, taking into account the considerations of cost and reliability of the fnal device. There might be options for the Collaboration with other experimental projects at JLab interested in implementing similar designs for their experiments [139].

### 12.1.2 Simulations Study of $K_L$ Beam Production

We simulated neutral kaon production in a photon bremstruhlung beam produced by the 12 GeV electron beam in the Hall D CPS. We analyzed $K_L$ production via $\phi$-meson photoproduction in detail. This is one of the main mechanisms of $K_L$ production in our energy range. It gives the same number of $K^0$ and $\overline{K^0}$. Another mechanism is hyperon photoproduction (which gives only $K^0$), which was not studied in our simulations separately. Instead, we have taken as an alternative model the Pythia generator [140], which includes hyperon production. $\phi$-meson photoproduction total and differential cross sections on proton and complex nuclei (coherent and incoherent) data were taken from Refs. [141,142]. The angular distributions for $\phi \to K_L K_S$ decay that we used are from Ref. [142–144]. Our calculations show that $\phi$ decay in its rest frame is mostly perpendicular to the axis of $\phi$ momentum. Since $K_L$s need to stay along the original photon beam direction to get to the $LH_2/LD_2$ cryotarget, this condition requires that the $\phi$ production and decay angles in the laboratory frame should be about the same. That means that we will have only $K_L$s from $\phi$-mesons produced at relatively high transfer momentum $t$ at the $LH_2/LD_2$ target. It suppresses the number of "useful" $K_L$s by factor of $\sim 3$ or more (in comparison with the case if $K_L$ and $K_S$ momenta are parallel to the $\phi$ momentum). $K_L$ absorption, used in our calculations, was studied in Ref. [145] very well. Finally, about 80% of produced $K_L$s will be absorbed in the Be target and followed a tungsten and water beam plug. The value of absorbed $K_L$s can be reduced by optimizing the beam plug setup.

### 12.1.3 $K_L$ Beam Parameters

One of the main $K_L$-beam parameters is momentum distribution (momentum spectrum is a function of the distance and angle) [146]. Results of our simulations for $K_L$ momentum spectrum for $K_L$ reaching the $LH_2/LD_2$ cryotarget is shown in Fig. 17. The spectrum first has increasing shape since $\phi$ decay cone angle decreasing at higher $\gamma$-beam and $K_L$ momentum. This selecting lower $\phi$ production $t$ values, which are more favorable according to the $\phi$ differential cross section. At a certain point, the highest possible $\gamma$-beam momentum is reached and $K_L$ momentum spectrum then dies out pretty fast. For comparison, we selected part of the $K_L$ spectrum from the Pythia generator originated only from $\phi$ decays and showed it on the same plot (red histogram). .

Pythia calculations show that $\phi$ decays give about 30% of $K_L$s. The number of $K^0$ exceeds the number of $\overline{K^0}$ by 30% according to this generator for our conditions. Their momentum spectra are shown in Fig. 18 separately. To estimate the expected rate of $K_L$s at the $LH_2/LD_2$ cryotarget, we used the following conditions: electron beam current is 3.2 $\mu$A, Tagger radiator thickness is 1% R.L., Be target thickness is 40 cm, distance between Be and $LH_2/LD_2$ targets is 16 m, and radius of the cryotarget is 2 cm. Our MC calculations are related to the $K_L$ flux at that distance and solid angle. Pythia calculations give 100 $K_L$/s for the $\phi$ photoproduction and 240 $K_L$/s from all sources for $K_L$-beam intensity under the above conditions. There is a reservation to increase the $K_L$-beam intensity by increasing tagger radiator thickness and size of the Be target, electron beam current and other parameters. Increasing $LH_2/LD_2$ target radius will increase the number of $K_L$s reaching it proportionally to the solid angle. Finally, we generated $6 \times 10^9$ 12-GeV electrons for the $LH_2/LD_2$ cryotarget radius 4 cm, electron beam current 5 $\mu$A, 10% R.L. tungsten radiator and

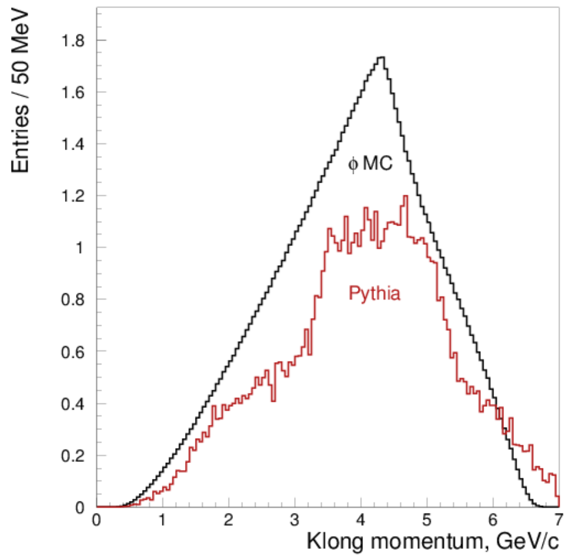


Figure 17: $K_L$ momentum spectra originated from $\phi$ decays: black histogram - our simulations using GEANT [147], red - Pythia generator result [140].

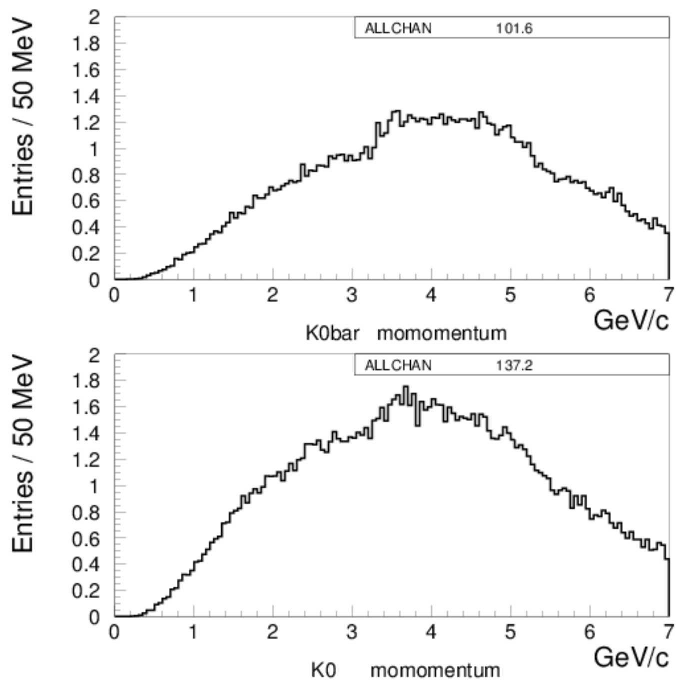


Figure 18: Momentum spectra from Pythia generator [140]. Top plot for $\overline{K^0}$. Bottom plot for $K^0$.

increased Be target sizes, we shall be able to obtain beam rate about $10^4$ $K_L$/s from all production mechanisms at $LH_2/LD_2$ target (Fig. 19).

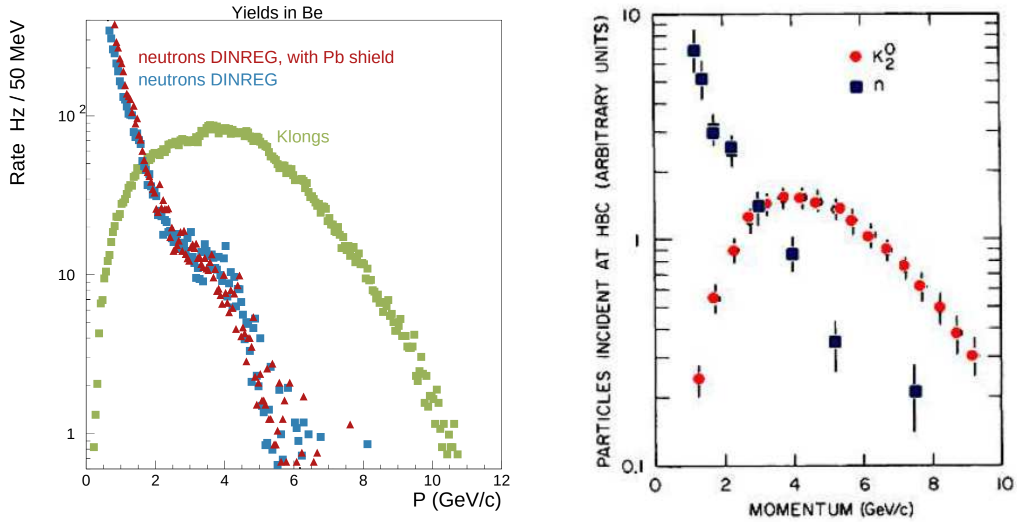


Figure 19: $K_L$ and neutron momentum spectra. Left plot: MC calculations using JLab package DINREG [147]. The rate of $K_L$ (green filled squares) and neutrons (black open diamonds) on $LH_2/LD_2$ cryogenic target of Hall D as a function of their event MC generators with $10^4$ $K_L$/s. Right plot: Experimental data from SLAC measurements at 16 GeV/$c$ electrons from Ref. [56]. The rate of $K_L$ (black filled squareds) and neutrons (red filled circles).

We have to point out that our MC simulations for the JLab 12 GeV case (Fig.19(left)) agreed quite well with $K_L$ yields measured by SLAC at 16 GeV (Fig. 19(right)).

#### 12.1.4 $K_L$ Beam Background: Gammas, Muons, and Neutrons

Background conditions is one of the most important parameter of the $K_L$ beam for the JLab GlueX KL Facility [146].

1. **Gamma Background**

   After passing through 30% R.L. tungsten beam plug and swiping out charged background component, we will have some residual $\gamma$ background and neutrons produced by EM showers. Momentum spectrum of residual $\gamma$s shown on Fig. 20 (left). It decreases exponentially with increasing energy of photons. For the rates, we obtained $\sim 10^5\ s^{-1}$ for $\gamma$s with energy above 50 MeV and $\sim 10^3\ s^{-1}$ for $\gamma$s with energy above 500 MeV. Overall, gamma flux for the KLF experiment is tolerable.

2. **Muon Background**

   Following to Keller [148], our Geant4 [149] simulations included Bethe-Heitler muon background from the Be-production target and photon dump, both background into the detector and muon dose rate outside Hall D. Obviously, most of the muons are produced in the photon dump. Our calculations show that muons will be swiped out of the $K_L$ beam line thus

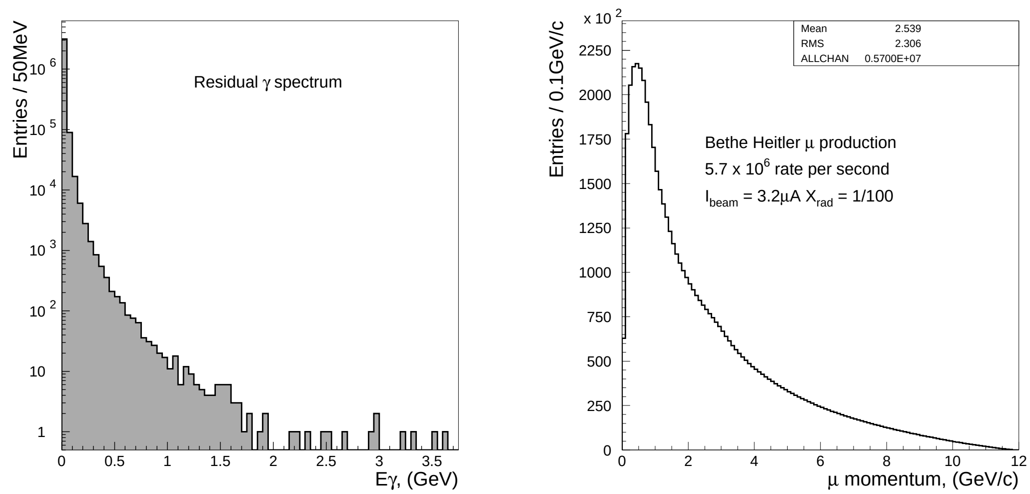


Figure 20: Left panel: Momentum spectrum of residual $\gamma$s. Right panel: Muon momentum spectrum for Bethe-Heitler production.

they are not our background. But since their high penetration ability, it might be important for purposes of the shielding. We taken into account only the Bethe-Heitler muon production process. Muons from pion decays and other productionmechanisms will increase total muon yield only slightly. They were not included in our model. Number of produced muon in the Be target and lead beam plug is about the same, lead originating muons have much softer momentum spectrum. Estimated number of produced muons is $\sim 6 \times 10^6\ s^{-1}$. Their momentum spectrum is shown on Fig. 20(right).

To summarize: Half of muons have momenta higher than 2 GeV/$c$, $\sim 10\%$ of muons have momenta higher than 6 GeV/$c$, and $\sim 1\%$ of muons with momenta above 10 GeV/$c$. Overall, the muon flux for the KLF experiment is tolerable.

3. **Neutron Background**

To calculate the neutron yield from the Be target and other sources, we used the JLab program package DINREG [147]. We generated $6 \times 10^9$ 12-GeV electron (electron current is 5 $\mu$A) which hit the 10% R.L. tungsten plus water radiator (Fig. 19(left)). The exiting is about $10^{13}\ s^{-1}$ 99% of them associated with neutron momentum $p < 420$ MeV/$c$ ($E < 90$ MeV), while 0.6% of them are for $p > 500$ MeV/$c$. The angular and energy distributions of neutrons produced from the Be target shown in Figs. 21 and 22.

Overall, our MC simulations for 12 GeV (Fig.19(left)) agreed quite well with neutron yields measurements that SLAD did for 16 GeV (Fig. 19(right)). Note that with a proton beam, the $n/K_L$ ratio is $10^3 - 10^4$ (see, for instance, Table 2 in Appendix A1 (Sec 15), while in the JLab case, this ratio is less than 10 as Fig. 23 shows.

For the following neutron calculations (Fig. 24), we used the MCNP6 NParticle (MCNP) Transport code [150]. It takes into account multiple scattering processes of neutrons as well. We will ignore the GlueX setting in these calculations. Horizontal view of the neutron flux using MCNP6 transport code calculations shown on Fig. 25.

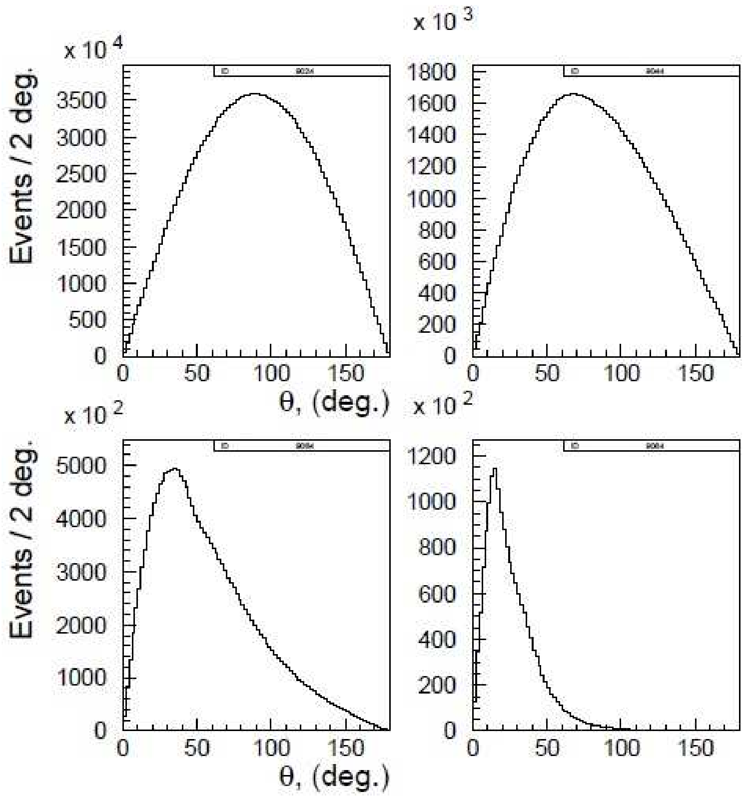


Figure 21: Angular distributions of neutron produced from the Be-target and other sources. DIN-REG [147] outcome: Top left: E = 1 – 5 MeV, Top right: E = 20 – 50 MeV, Bottom left: E = 120 – 150 MeV, and Bottom right: E = 500 – 1000 MeV.

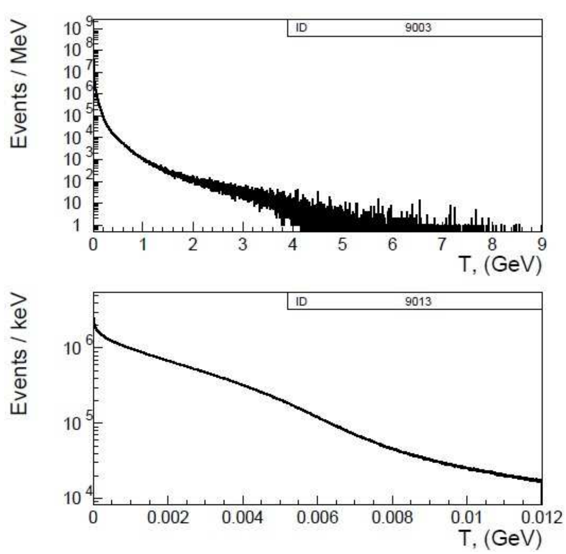


Figure 22: Energy distributions of neutrons produced from the Be-target and other sources. DIN-REG [147] outcome. Bottom plot is zoom of top one to show very low energies in details.

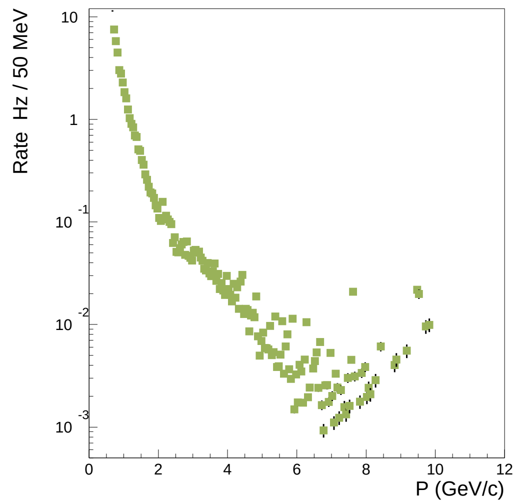


Figure 23: The $n$ to $K_L$ ratio associated with Fig. 19(left).

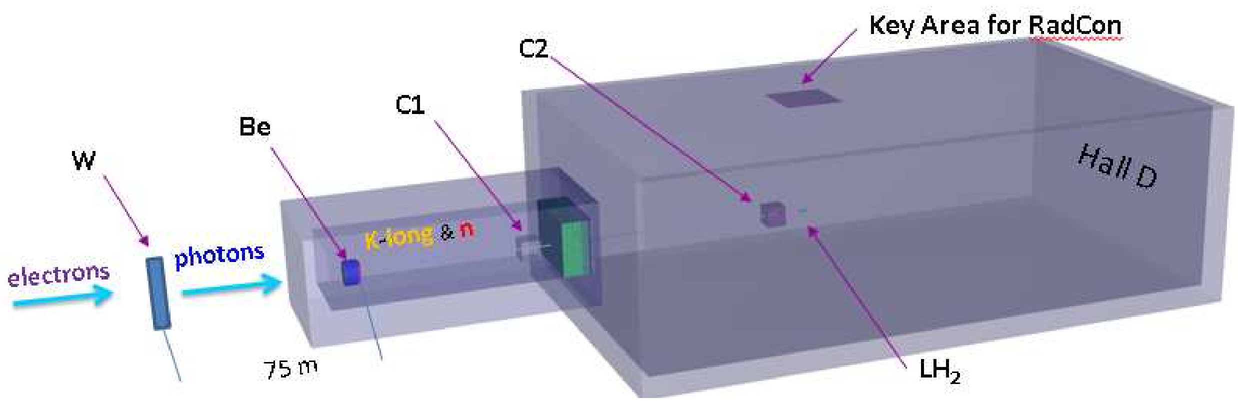


Figure 24: Schematic view of Hall D setting for MCNP6 transport code [150] calculations. Beam goes from left to right. Collimators presented as semitransparent for the demonstration purpose. This 3D plot is similar as Fig. 15 shows.

Energy distribution of neutrons emitted from Be target (in N/($MeV \cdot s \cdot cm^2$) units) shown in Fig. 26.

Overall, neutron flux for KLF experiment is tolerable and below the RadCon limit.

we have to accomplish this subsec

### 12.1.5 $K_L$ Momentum Determination and Beam Resolution

The mean lifetime of the $K_L$ is 51.16 ns ($c\tau = 15.3$ m) whereas the mean lifetime of the $K^-$ is 12.38 ns ($c\tau = 3.7$ m) [1]. For this reason, it is much easier to perform measurements of $K_Lp$ scattering at low beam energies compared with $K^-p$ scattering.

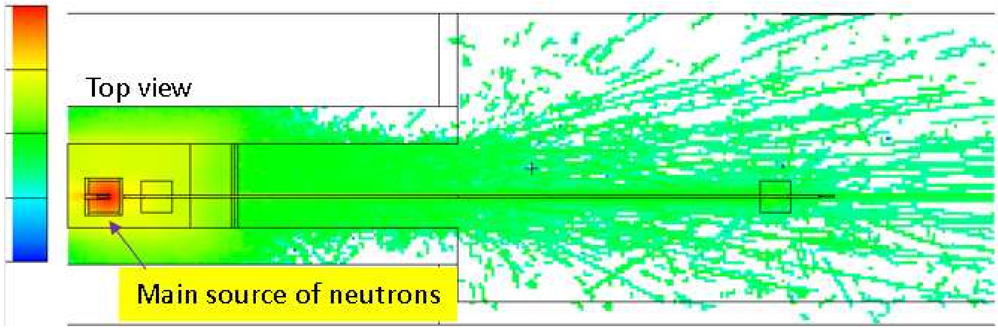


Figure 25: Horizontal view of the neutron flux using MCNP6 transport code [150] calculations (arbitrary units) following geometry at Fig. 24. Beam goes from left to right.

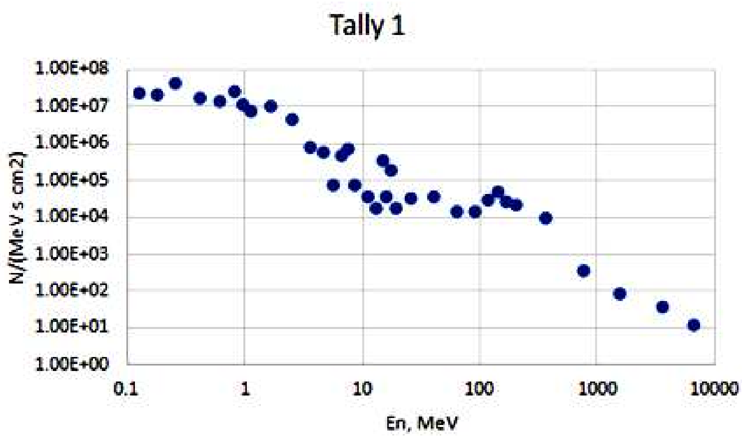


Figure 26: Neutron emitted from Be-target calculations using MCNP6 transport code [150].

The momentum of a $K_L$ beam can be measured using TOF - the time between the accelerator bunch (RF signal from CEBAF) and the reaction in the $LH_2/LD_2$ target as detected by the Start Counter (SC). Hall D Broadband Tagging Hodoscope timing cannot be used at such high intensity conditions. Thus TOF resolution is a quadratic sum of accelerator time and SC time resolutions. Since the accelerator signal has a very good time resolution ($\sim 150$ ps or better), TOF resolution will be defined by the SC. The Hall D SC has a resolution of $\sim 250 - 300$ ps. This value can hopefully be improved by upgrading the counter design, which reflected on its parameters (more details are in Sec. 12.1.6). In our calculations, we used the value 250 ps for the SC time resolution. We plan to improve its time resolution and details are given in Sec. 12.1.6. Of course, to get TOF information, the electron beam needs to have a narrow bunch time structure with a bunch spacing of, at least, 60 ns. In order to be able to measure the roughly 20 ns ToF of the elastic protons, the beam for the G0 experiment at Hall C has 32 ns between electron bunches (in contrast to the usual 2 ns spacing for each experimental hall) using a 31.1875 MHz pulsed laser to operate the electron source [151]. One cannot expect a problem with a 60 ns time structure to delivery an electron beam to any Hall, A, B, or C [152].

The uncertainty in a neutral kaon production position at lower momenta (p < 0.5 GeV/$c$) affects timing resolution caused by the TOF difference between the photon and kaon time traversing Be-

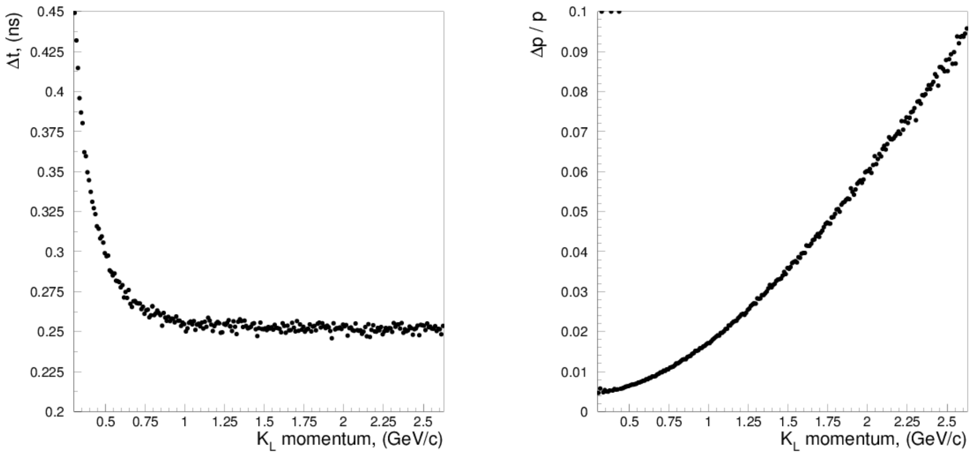


Figure 27: Left plot: Time resolution, $\Delta t$, for $K_L$-beam as a function of $K_L$ momentum. Right plot: Momentum resolution, $\Delta p/p$, as a function of momentum.

target, however as $\Delta p/p = \gamma^2 \Delta T/T$ momentum resolution is below 1% at lower momenta. Figure 27 shows TOF, $\Delta t$ (FWHM), (left) and beam momentum resolution, $\Delta p/p$ (FWHM) (right) as a function of the $K_L$ beam momentum, respectively.

The TOF resolution is flat for momenta higher than 1 GeV/$c$. Momentum resolution is growing with momentum value, for 1 GeV/$c$ it is ~1.7%, for 2 GeV/$c$ it is ~6%.

Figure 28 shows that for $W < 2.1$ GeV, $\Delta W <$ 20 MeV, which is suitable for studying low-lying hyperons with widths of $\Gamma = 30$ – 50 MeV [1].

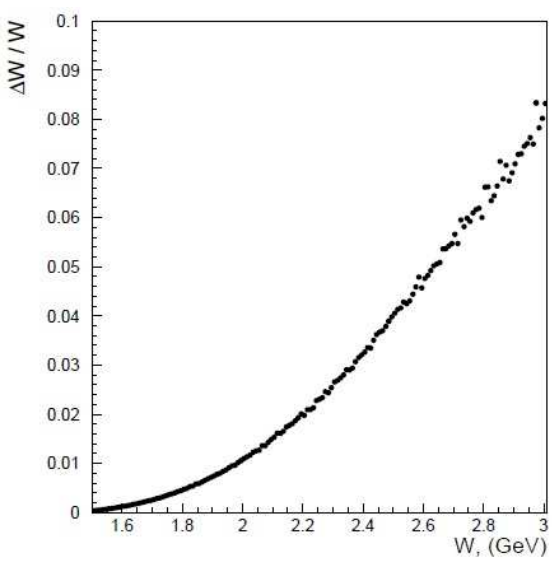


Figure 28: Energy resolution, $\Delta W/W$, as a function of energy.

### 12.1.6 Start Counter Time Resolution

The $K_L$ beam momentum and time resolution is governed by the time resolution provided by the GLUEX detector from the reconstruction of charged particles produced in the $LH_2/LD_2$ target. There are three detector systems which can provide precision timing information for reconstructed charged particles in GLUEX: the Start Counter (ST), Barrel Calorimeter (BCAL), and Time of Flight (TOF) detectors. The aforementioned detectors, and the charged particle time resolutions they provide, are discussed in this section.

The GLUEX Start Counter is a cylindrical plastic scintillator detector surrounding the $LH_2/LD_2$ target, with 3 mm thick scintillator bars and a tapered nose region which bends toward the beamline at the downstream end. The scintillation light from each of the 30 scintillator bars are detected by an array of 4, $3 \times 3$ $\mathrm{mm}^2$ Hamamatsu S10931-050P surface mount silicon photomultipliers (SiPMs) [153]. The time resolution of the ST was determined to be 250 ps during the 2016 and 2017 GLUEX run periods, as shown in Fig. 29, and thus provided adequate separation of the 250 MHz photon beam bunch structure delivered to Hall D during that time. This performance was achieved using the recommended operating gain and bias voltages supplied by Hamamatsu to provide both the FADC 250 analog signals and precision F1TDC discriminator signals used in the GLUEX reconstruction. For the $K_L$ program we propose to increase the gain of the ST SiPMs, thereby increasing the number of detected photoelectrons, as well as modify the pulse shape processing electronics. Similar gain and readout electronic customization were implemented in the GLUEX Tagger Microscope, which utilizies an identical SiPM readout system, provided timing resolutions of 200 ps. Moreover, the GLUEX Coarse Pair Spectrometer scintillators, also utilizing an identical SiPM readout system, achieved timing resolutions of 120 ps. Implementation of these non-invasive modifications to the ST will significantly improve the timing resolution. In simulations of the GLUEX detector performance we therefore assume a 150 ps resolution as the baseline ST performance which may be achieved with modifications to the current device.

Future improvements to the start counter to further reduce the time resolution will be studied to increase both the light production in the scintillators and the light collection efficiency. The long term goal would be to reach a time resolution of 50-100 ps for the ST, which may require invasive modifications to the current device, or a complete replacement. Increased light production could come through an increase of the scintillator bar thickness, or a different choice of scintillator material with a higher light yield and shorter decay time such as EJ-204. Improved photodetectors, including Microchannel Plate PMTs which also perform well in high magnetic field environments, could provide higher gain and better efficiency than the current SiPMs, and will be investigated to assess their potential impact on the ST performance.

The GLUEX BCAL is a scintillating fiber calorimeter, which provides timing information for both neutral and charged particles. The measured time resolution of the BCAL for charged particles depends on the reconstructed BCAL energy, but has an average value of $\sim 220$ ps during the GLUEX Spring 2017 run period. For charged particles with large scattering angles ($11^\circ < \theta < 120^\circ$) this additional measure of the interaction time will improve the overall $K_L$ time resolution when combined with the ST measurement. The GLUEX TOF is composed of two planes of 2.5 cm thick scintillator bars. The measured TOF time resolution is 100 ps from the GLUEX Spring 2017 run period, well below the assumed performance of the ST. Therefore, for reactions with a charged

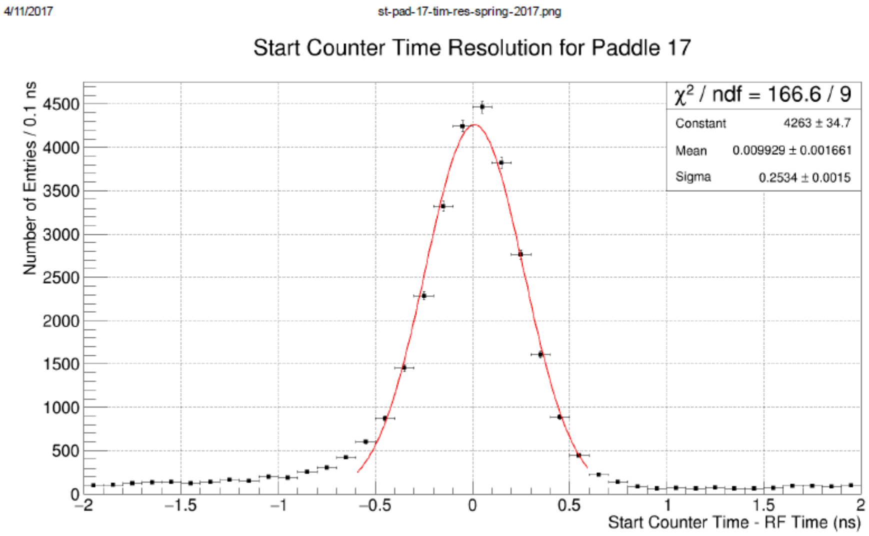


Figure 29: Time difference between the measured and expected ST time from the Spring 2017 GLUEX run period. The data are fit with a Gaussian to determine the current time resolution of $\sim 250$ ps.

particle which is produced in the forward region $\theta < 11°$, the TOF will be used to provide a better $K_L$ momentum determination than the ST.

To summarize, the current ST performance has been demonstrated to reach a $\sim 250$ ps time resolution and the current device is expected to be capable of providing a time resolution of $\sim 150$ ps once fully optimized for the $K_L$ facility. The simulation studies in this proposal (See Sec. 13) have assumed a time resolution of 150 ps, which is adequate for the proposed physics program. With the current detector, the overall $K_L$ momentum resolution will be improved by utilizing the timing information from the BCAL and TOF detectors, to ensure the 150 ps specification is achieved. Finally, we are exploring potential upgrades to significantly improve the ST time resolution however, further study is required to understand the impact of such improvements on the extracted resonance parameters for the proposed hyperon spectroscopy program.

#### 12.1.7 Measurement of $K_L$ Flux

The $K_L$ has four dominant decay modes [1]:

1. $K_L \to \pi^+\pi^-\pi^0, BR = 12.6 \pm 0.6\%$.
2. $K_L \to \pi^0\pi^0\pi^0, BR = 21.5 \pm 0.9\%$.
3. $K_L \to \pi^\pm e^\mp \bar{\nu}_e, Br = 38.8 \pm 1.6\%$.
4. $K_L \to \pi^\pm \mu^\mp \bar{\nu}_\mu, BR = 26.8 \pm 1.2\%$.

In addition, there are several rare decay modes, including CP-violating $K_L \to 2\pi$ mode. In three of the four principal decay modes of the $K_L$, two charged particles are emitted. To measure the flux of $K_L$ beam at GlueX we will measure the rate of of $K_L$ decays to two oppositely charged tracks in the Hall D Pair Spectrometer [154] upstream of the GlueX physics target. The timing information from the pair spectrometer will be used to estimate time of flight elapsed between the creation of a $K_L$ in Be target and its decay to measure momenta of decayed kaons. In a long run with high statistics $2\pi$ decay mode also can be used for a reference to measure independently a flux and momenta of decayed kaons and reconstruct the flux of incoming kaons. This experiment will employ similar technique used in the most precise measurements of $K_L$ flux (see for example [155–157]). Overall, expectated $K_L$ flux measurement will be accurate to 5%.

## 12.2 $LH_2/LD_2$ Cryotarget for Neutral Kaon Beam at Hall D

The proposed experiment will utilize the existing GlueX liquid hydrogen cryotarget (Fig. 30), modified to accept a larger diameter target cell [158]. The GlueX target comprises a kapton cell containing liquid hydrogen at a temperature and pressure of about 20 K and 19 psia. The 100 ml cell is filled through a pair of 1.5 m long stainless steel tubes (fill and return) connected to a small container where hydrogen gas is condensed from two room temperature storage tanks. This condenser is cooled by a pulse tube refrigerator with a base temperature of 3 K and cooling power of about 20 W at 20 K. A 100 W temperature controller regulates the condenser at 18 K.

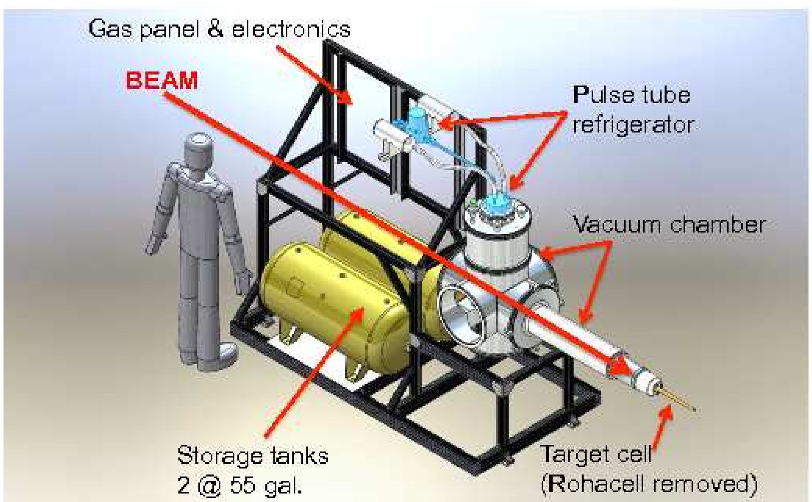


Figure 30: The GlueX liquid hydrogen target.

The entire target assembly is contained within an "L"-shaped, stainless steel and aluminum vacuum chamber with a Rohacell extension surrounding the target cell. The SC for the GlueX experiment fits snugly over this extension. The vacuum chamber, along with the hydrogen storage tanks, gas handling system, and control electronics, is mounted on a custom-built beamline cart for easy insertion into the Hall D solenoid. A compact I/O system monitors and controls the performance of the target, while hardware interlocks on the target temperature and pressure and on the chamber vacuum ensure the system's safety and integrity. The target can be cooled from room temperature and filled with liquid hydrogen in about 5 hours. For empty target runs, the liquid can be boiled from the cell in about twenty minutes (the cell remains filled with cold hydrogen gas), and then refilled with liquid in about forty minutes.

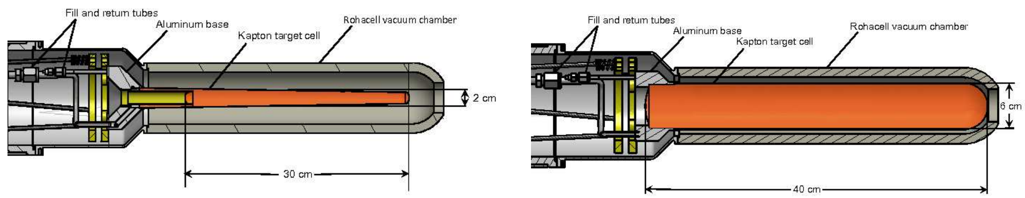


Figure 31: Left plot: Kapton target cell for the GlueX $LH_2/LD_2$ target. Right plot: Conceptual design for a larger target cell for the proposed $K_L$ beam in Hall D.

The GlueX cell (Fig. 31) is closely modeled on those utilized in Hall B for more than a decade and is a horizontal, tapered cylinder about 38 cm long with a mean diameter of 2 cm. The cell walls are 130 $\mu$m kapton glued to an aluminum base. A 2 cm diameter reentrant beam window defines the length of $LH_2/LD_2$ in the beam to be about 30 cm. Both entrance and exit windows on the cell are 75 $\mu$mkapton. In normal operation the cell, the condenser, and the pipes between them are all filled with liquid hydrogen. In this manner the liquid can be subcooled a few degrees below the vapor pressure curve, greatly suppressing bubble formation in the cell. In total, about 0.4 liter of $LH_2$ is condensed from the storage tanks, and the system is engineered to safely recover this quantity of hydrogen back into the tanks during a sudden loss of insulating vacuum, with a maximum allowed cell pressure of 49 psia [159].

A conceptual design for the neutral kaon beam target is also shown in Fig. 31. The proposed target cell has a diameter of 6 cm and a 40 cm length from entrance to exit windows, corresponding to a volume of about 1.1 liter, which will require filling the existing tanks on the target cart to about 50 psia. The collaboration will work with the JLab Target Group to investigate alternative materials and construction techniques to increase the strength of the cell. As an example, the $LH_2$ target cell recently developed for Hall A is 6.3 cm in diameter, 18 cm long and has a wall thickness of approximately 0.2 mm. The cell is machined from a high-strength aluminum alloy, AL7075-T6, and has a maximum allowed pressure of about 100 psia. It is expected that minor modifications to the cryotarget's piping systems will also be required to satisfy the increased volume of condensed hydrogen.

The proposed system is expected to work equally well with liquid deuterium, which condenses at a slightly higher temperature than hydrogen (23.3 K versus 20.3 K at atmospheric pressure). The expansion ratio of $LD_2$ is 13% higher, implying a storage pressure of about 60 psia. Therefore the new target cell must be engineered and constructed to work with either $H_2$ or $D_2$.

## 13 Running Condition

Short para for here ??

## 13.1 Event Identification, Reconstruction, Acceptances

The $K_L$ beam is generated by sampling the momentum distribution of $K_L$ particles coming from the decays of $\phi$ mesons produced by interactions of a photon beam with a beryllium target 16 m upstream of the $LH_2$/$LD_2$ cryotarget. The $K_L$ beam profile was assumed to be uniform within a 2 cm radius at the $LH_2$/$LD_2$ cryotarget. Due to the very strong $t$-dependence in the $\phi$ photoproduction cross section [160] and a $P$-wave origin of the $\phi \to K_L K_S$ decay majority of kaons flight at very small angle.

### 13.1.1 Simulations and Reconstruction of Various Channels Using GlueX Detector

The GlueX detector is a large acceptance detector based on a solenoid design with good coverage for both neutral and charged particles. The detector consists of a solenoid magnet enclosing devices for tracking charged particles and detecting neutral particles and a forward region consisting of two layers of scintillators (TOF) and a lead-glass EM calorimeter (FCAL). A schematic view of the GlueX detector is shown in Figure 32. The magnetic field at the center of the bore of the magnet for standard running conditions is about 2 T. The trajectories of charged particles produced by interactions of the beam with the 40-cm $LH_2$/$LD_2$ cryotarget at the center of the bore of the magnet are measured using the Central Drift Chamber (CDC) for angles greater than $\approx 20^\circ$ with respect to the beam line. Forward-going tracks are reconstructed using the Forward Drift Chambers (FDC). The timing of the interaction of the kaon beam with the $LH_2$ cryotarget is determined using signals from the SC, an array of 30 mm thin (3 mm thick) scintillators enclosing the target region. Photons are registered in the central region by the Barrel Calorimeter (BCAL). Detector performance and reconstructions techniques were evaluated during the main GlueX programme. Details can be found elswhere [161].

This section describes some simulations of events generated by $K_L$ beam particles interacting with a $LH_2$/$LD_2$ cryotarget at the center of the solenoid [162]. The GlueX detector is used to detect one or all of the final state particles. We will be focusing on a few of the simple two-body reactions, namely $K_Lp \to\ K_Sp$, $K_Lp \to \pi^+\Lambda$, $K_Lp \to K^+\Xi^0$, and $K_Lp \to K^+n$.

For each topology, one particle (the proton for the $K_Sp$ channel, the $\pi^+$ for the $\Lambda\pi^+$ channel and the $K^+$ for the $K^+\Xi^0$ channel) provides a rough determination for the position of the primary vertex along the beam line that is used in conjunction with the SC to determine the flight time of the $K_L$ from the beryllium target to the hydrogen target. Protons, pions, and kaons are distinguished using a combination of $dE/dx$ in the chambers and time-of-flight to the outer detectors (the Barrel Calorimeter (BCAL) and two layers of scintillators (TOF)) (see Appendix A3 (Sec 17) for further details).

### 13.1.2 $K_Lp \to K_Sp$ Reaction

The total production cross section, shown in Fig. 33, is reasonably large; however, for the differential cross section there is a fair amount of tension in the existing data sets between different measurements, and the angular coverage in some bins is sparse. Figure 34 shows the existing dif-

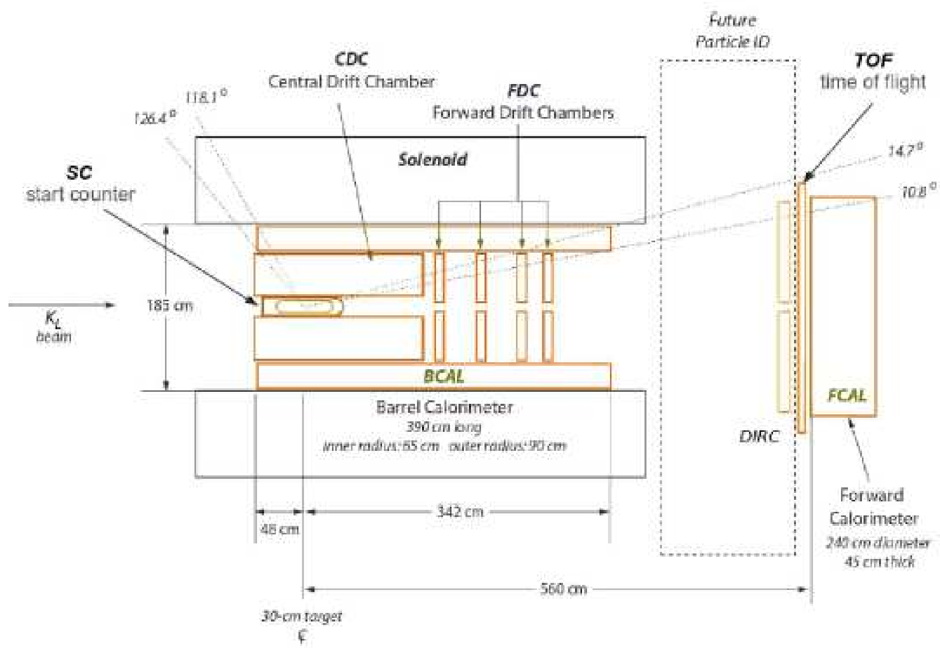


Figure 32: Schematic view of the GlueX detector.

ferential cross section data for several bins in $W$. The cross section as a function of $\cos\theta_{CM}$ was parametrized using a set of Legendre polynomials (blue curves in Fig. **??**); the weights of each polynomial in the set depended on $W$. This parametrization was used to generated $pK_L \to pK_S$ events that were passed through a full GEANT3-based Monte Carlo of the GlueX detector. The final state particles were constructed using the standard GlueX reconstruction code. We reconstructed the $K_S$ in its $\pi^+\pi^-$ channel. More details about the reconstruction of this channel can be found in Appendix A3 (Sec 17.1.1). Estimates for statical errors in the measured cross section for 100 days of running at $3 \times 10^4\ K_L/s$ as a function of $\cos\theta_{CM}$ for several values of $W$ are shown in Fig. 35. We estimate that for $W < 3$ GeV with an incident $K_L$ rate of $3 \times 10^4/s$ on a 40-cm long LH2 target, we will detect on the order of 8M $pK_S$ events in the $\pi^+\pi^-$ channel.

### 13.1.3 $K_L p \to \pi^+\Lambda$ Reaction

The $K_L p \to \pi^+\Lambda$ along with $K_L p \to \pi^+\Sigma$ is the key reaction to disentangle the weak exchange degeneracy of the $K^*(890)$ and $K^*(1420)$ trajectories. A general discussion is described in Sections **??**). The first time measurement of this reaction had been carried out at Stanford Linear Accelerator Center (SLAC) in 1974 [164] for $K_0$ beam momentum range between 1 GeV/$c$ to 12 GeV/$c$, which is shown in Fig. 36. However, the total number of $\pi^+\Lambda$ event had been collected with very limited statistics which is about 2500 event.

In our proposal in K-long Facility at Hall-D JLab, we expect good statistics of $K_L p \to \pi^+\Lambda$ with very wide range of $K_L$ beam momentum. Figure 37 shows the $K_L$ beam momentum distributions from the generated (left) and reconstructed (right) with requiring $\beta_{K_L} > 0.95$ in time-of-flight.

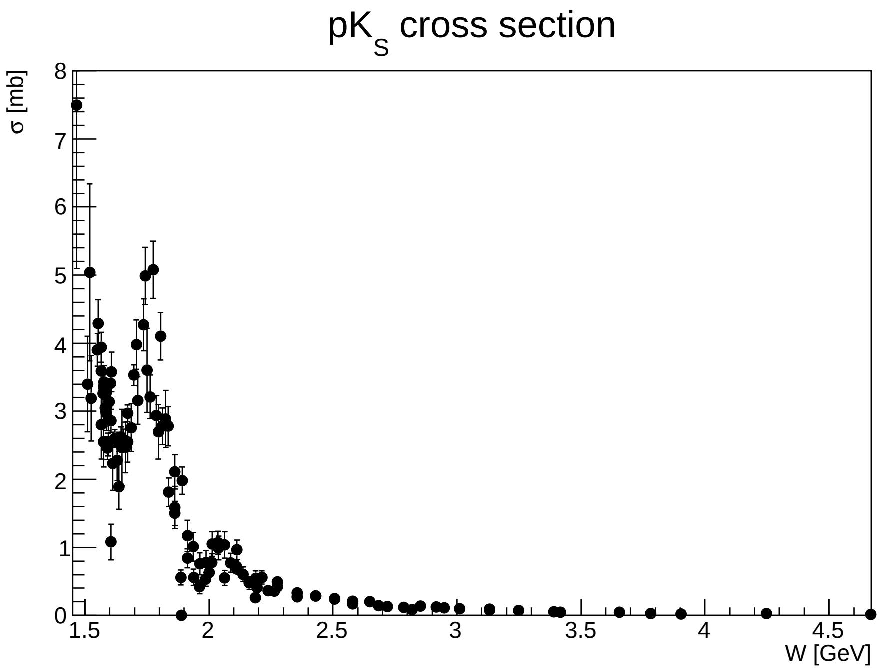


Figure 33: Total cross section for $K_L p \to pK_S$ as a function of $W$. The measured points are from [163] and references therein.

We have generated the $K_L p \to \pi^+ \Lambda$ reaction in phase-space with taking into account the realistic $K_L$ beam momentum distribution in the event-generator. This momentum spectrum is a function of the distance and angle. Then we went through the standard Hall-D full GEANT simulation with GlueX detector and momentum smearing. Finally, we utilized the JANA for particle reconstruction that we simulated. Figure 38 shows an example of the reconstructed the $\Lambda$ particle for invariant mass (left) and missing mass (right). As it shown in the simulation, we obtained the 5 MeV of invariant mass resolution and 150 MeV of missing mass resolution. We estimate the expected total number of $pi^+\Lambda$ events as final state particle within topology of $1\pi^+$, $1\pi^-$, and 1 proton. In 100 days beam time with $3 \times 10^4$ $K_L/s$ on the liquid hydrogen target, we expect to detect around 24M $K_L p \to \pi^+ \Lambda$ events for $W < 3$ GeV. Such an unprecedent statisitics will improve the our knowledge on these states through partial wave analysis.

Moreover, Figure 39 (left) shows the correlation between $\Lambda$ invariant mass from its decay particles ($p$, $\pi^-$) and missing mass of $\pi^+ X$. On the right plot in the Fig. 39, it shows the $\Lambda$ invariant mass as a function of pion angular distribution ($\theta_{\pi^+}$). All these plots are based on the 150 ps time resolution of the start counter.

The $K_L p \to \pi^+ \Lambda$ has relatively high production cross-section order of few mb in our proposed $K_L$ momentum range (1 – 6 GeV/$c$). The beam resolution has been calculated at the time-of-flight vertex time resolution of start counter (TOF-ST), 150 ps. The variation of invariant mass resolution as a function of $W$ for various TOF-SC timing resolution (100, 150, 300 ps) is similar as one from other reactions [165].

Figure 40 shows the estimation of the statistical uncertainty of the $\pi^+\Lambda$ total cross section as a

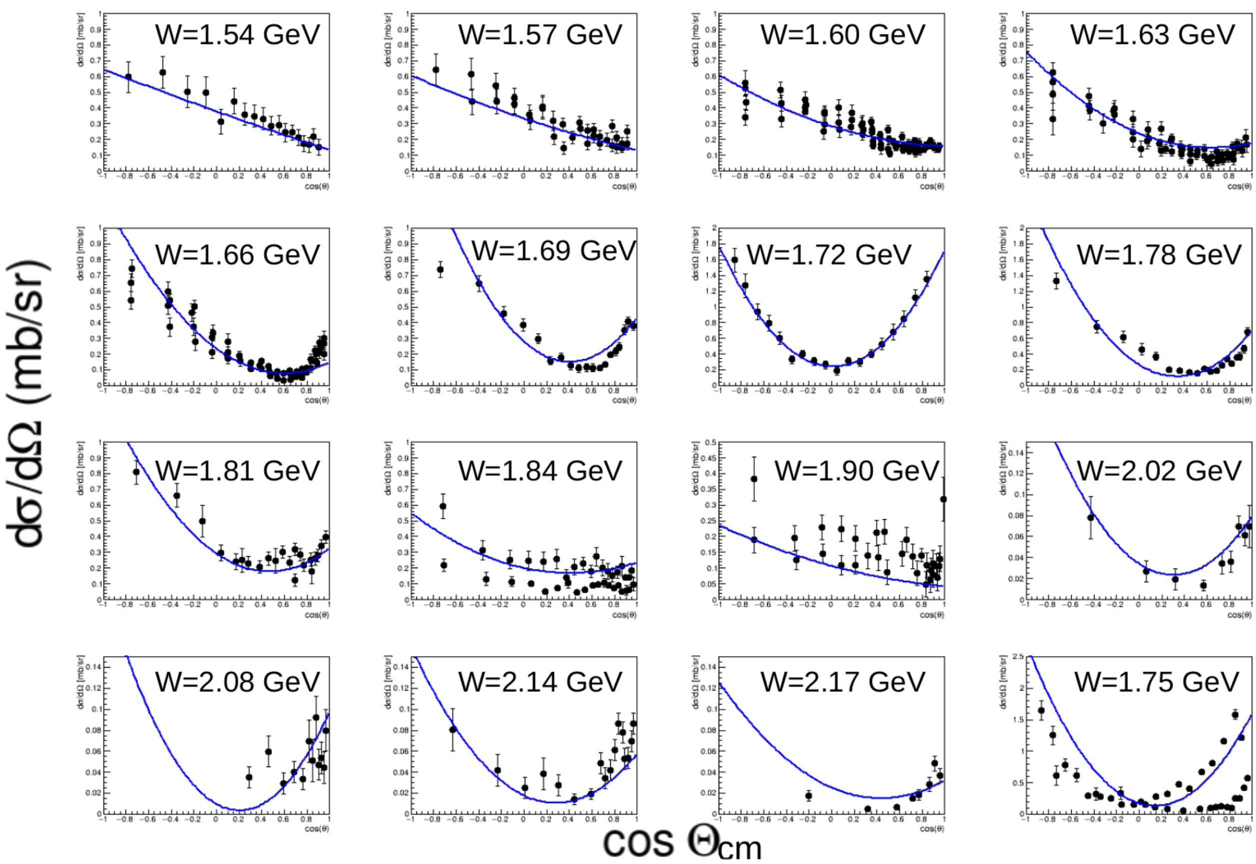


Figure 34: Differential cross section plots for $K_L p \to p K_S$ as a function of $W$. The blue curves are the result of a parametrization of the cross section in terms of Legendre polynomials. The measured points are from [163].

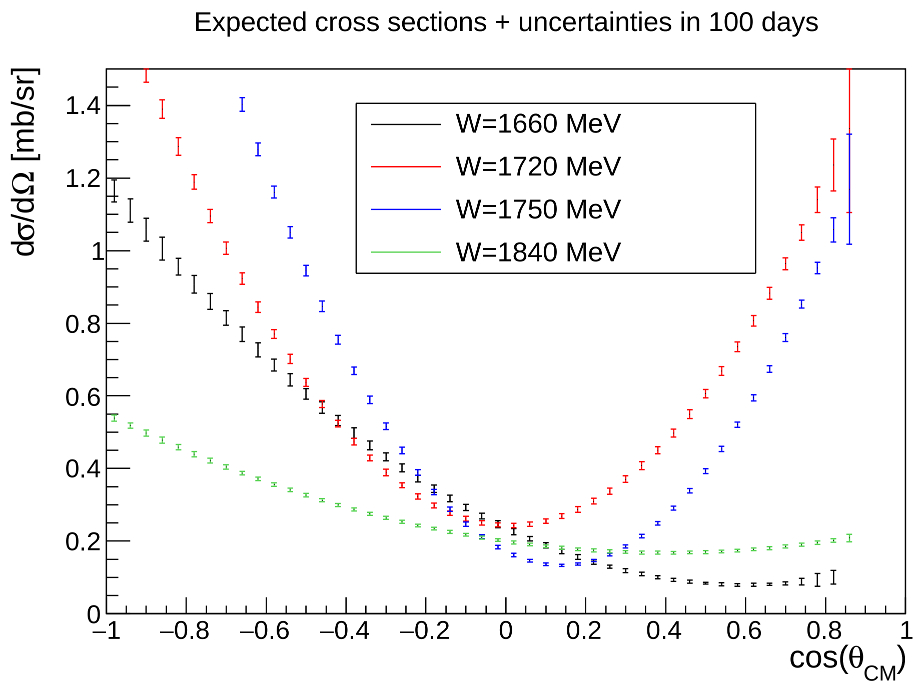


Figure 35: Reconstructed differential cross sections for various values of $W$ for 100 days of running.

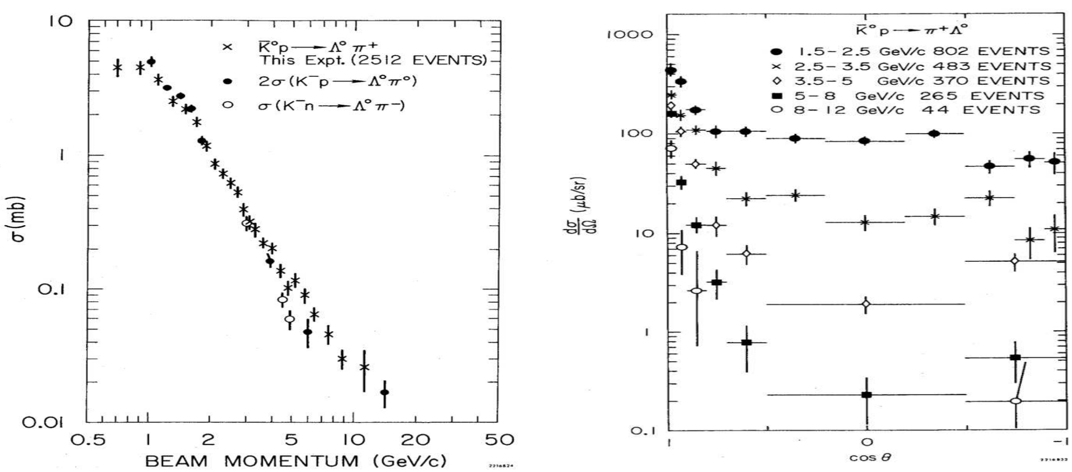


Figure 36: The total cross-section for $K_L p \rightarrow \pi^+\Lambda$ reaction as a function of beam momentum [164] (left) and the $\cos\theta$ dependent cross-sections for various beam momentum ranges.

function $K_L$ beam momentum. We keep the same momentum bin size as one from the SLAC data. The box shape error bars in the MC points (red triangles) are increased by factor of 10 for comparison with the SLAC data. As we see the proposed measurement will provide an unprecedent statistical accuracy to determine the cross section for wide range of $K_L$ momentum.

The major source of systematic uncertainty for this reaction would be misPID among $\pi^+$, K$^+$,

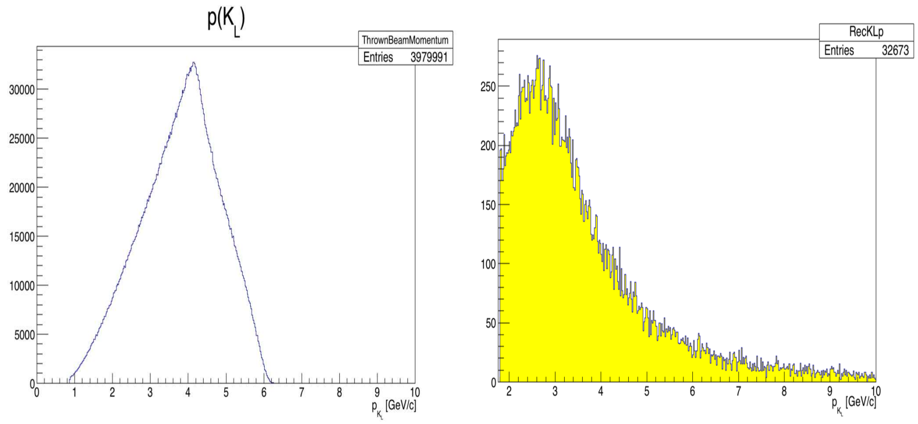


Figure 37: Beam particle ($K_L$) momentum distribution in MC simulation, generated (left) and reconstructed (right).

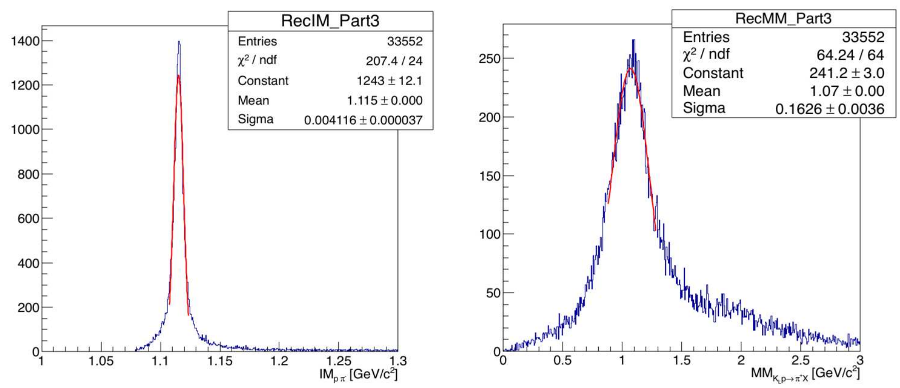


Figure 38: The $\Lambda$ invariant mass from reconstructing the its decay particles, proton and pion(-) (left), and the missing mass of $\pi^+X$ (right).

and proton in the final state. However, by requiring the reconstructed $\Lambda$ and side-band subtraction technique for background will improve this unceratinty substantially.

### 13.1.4 $K_Lp \to K^+\Xi^0$ Reaction

The study of cascade data will allow us to place stringent constraints on dynamical coupled channels models. In addition, cascade data will provide us with long-sought information on missing excited $\Xi$ states and the possibility to measure their quantum numbers of the already established $\Xi(1690)$ and $\Xi(1820)$ from a double-moments analysis. The large data sample expected allows us to determine the induced polarisation transfer of the cascade with unprecedented precision placing stringent constraints on the underlying dynamics of the reaction. Polarisation measurement of hyperons shed light on the contribution from individual quarks to the overall polarisation of

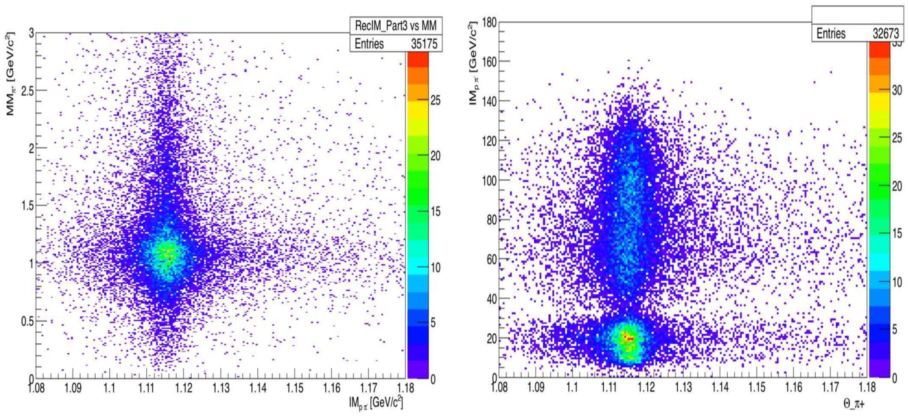


Figure 39: The $\Lambda$ invariant mass versus missing mass of $\pi^+X$ (left) and the $\theta_{\pi^+}$ angle distribution versus $\Lambda$ invariant mass (right).

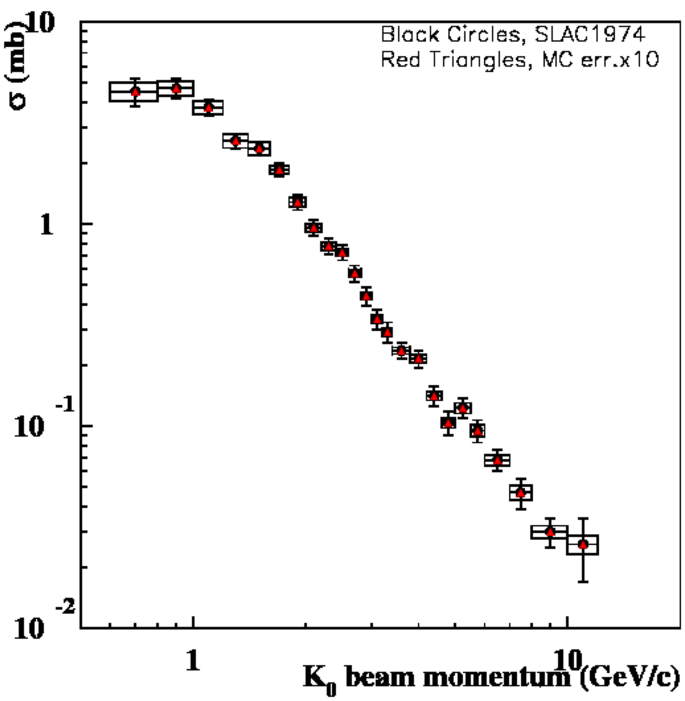


Figure 40: The total cross section unceratinty estimation (only statistical error) for $K_L p \rightarrow \pi^+\Lambda$ reaction as a function of $K_0$ beam momentum in comparison with SLAC data [164]. The experimental unceratinty have tick marks at the end of error bars. The box shape error bars in the MC points are increased by factor of 10.

these states. The polarisation of the ground state cascade can be measure from its weak decay in a straight forward way. With a $K_L$ beam the study of the reaction $K_L p \rightarrow K^+\Xi^0$ is quite simple and an unprecedented statistical sample can be easily obtained.

Several topologies can be used to reconstruct $K_Lp \to K^+\Xi^0$ events enhancing the available statistics. The biggest contribution results from requiring the reconstruction of only the $K^+$ in the final state and reconstructing the reaction using the missing-mass technique. The $\Xi^0$ decays almost 100% of the time to $\Lambda\pi^0$. Utilising the large branch ratios for $\Lambda \to p\pi^-$ and $\pi^0 \to \gamma\gamma$ we can also fully reconstruct the $\Xi^0$'s in the final state using four-momenta of the detected final state particles. Figure 41 shows the expected W resolution of $W$ for this reaction, depending on the accuracy of the time-of-flight for 300 ps (black), 150 ps (cyan), 100 ps (red), and when W is determined from all detected final state particles (blue).

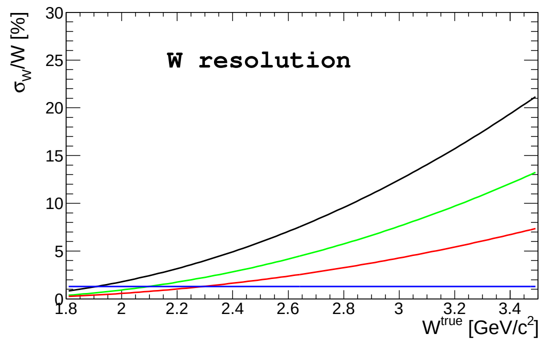


Figure 41: W resolution of $\sigma W/W$, depending on the accuracy of the time-of-flight for 300 ps (black), 150 ps (cyan), 100 ps (red), and when W is determined from all detected final state particles (blue).

In 100 days of beamtime with $3 \times K_L/s$ on the target, we expect $9 \times 10^6$ $K_Lp \to K^+\Xi^0$ events. From this, the available reconstructed events expected is $4 \times 10^6$ for Topology 1 $K_Lp \to K^+X$, $3 \times 10^5$ for Topology 2 $K_Lp \to K^+\Lambda X$, and $4 \times 10^4$ for Topology 3 $K_Lp \to K^+\Xi^0$. Figure 42 compares the statistical uncertainties of the total and differential cross sections for the reaction $K_Lp \to K^+\Xi^0$ with existing data taken from [166] for the three different topologies (column 1: only $K^+$ reconstructed, column 2: $K^+\Lambda$ reconstructed, and column 3: $K^+\Xi^0$ reconstructed).

This statistics also allows us to precisely determine the cascade induced polarisation utilising the fact that the cascade is self-analysing with an analysing power of $-0.406$ [1]. Figure 43 shows the statistical uncertainty estimates of the induced polarisation of the cascade by simple fits to the acceptance-corrected yields of the pion angular distribution in the $\Xi^0$ rest frame.

The main background for this reaction would come from the reaction $K_Lp \to K^+n$ and $K_Lp \to \pi^+\Lambda$, where the $\pi^+$ is miss-identified as a kaon. The former reaction has an order of magnitude higher cross section than the $K_Lp \to K^+\Xi^0$, however, the $W$ resolution below 2.5 GeV/$c^2$ allows a clean separation of these two reactions. Detection and reconstruction of the $\Lambda$ places additional constraints that reduce any background contributions significantly. Neutron induced reactions are not expected to contribute significantly to background and with missing-mass, invariant-mass, and time-of-flight cuts such background contributions can be eliminated.

The $K_L$ facility can be utilised to study excited cascade states $K_Lp \to K^+\Xi^*$ with $\Xi^* \to \Xi\pi$ and $\Xi^* \to \Xi\gamma$. These excited states should be easily identified and isolated using the missing-mass and invariant-mass techniques. A double-moment analysis can be employed by reconstructing the

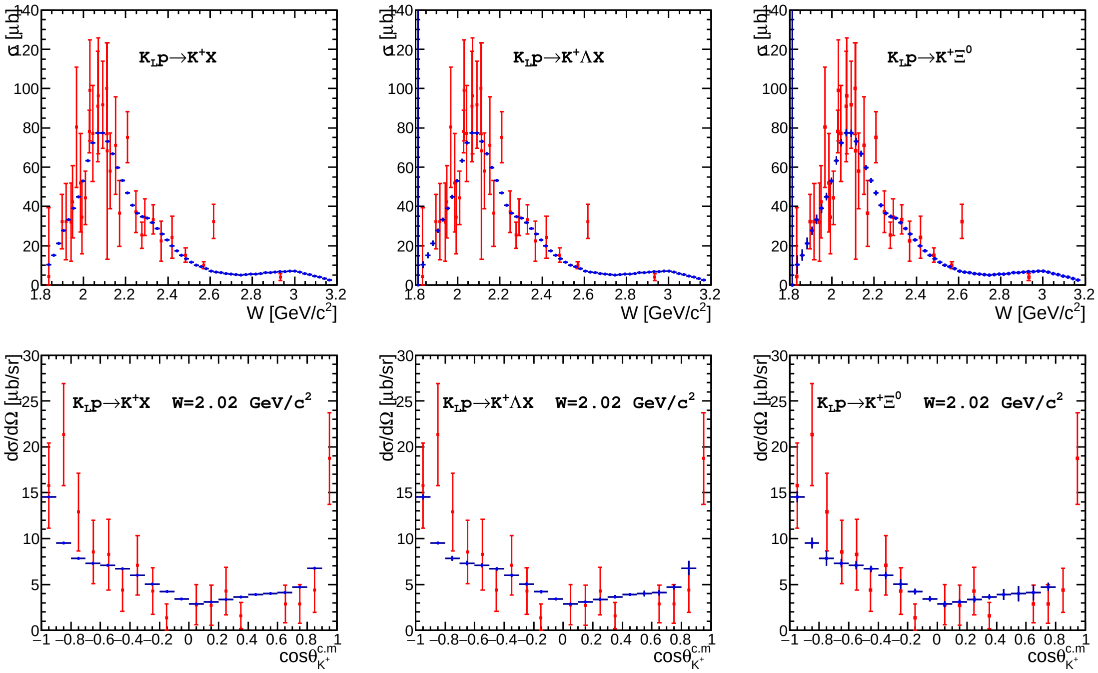


Figure 42: Total and differential cross section statistical uncertainty estimates (blue points) for the three topologies (column 1: only $K^+$ reconstructed, column 2: $K^+\Lambda$ reconstructed, and column 3: $K^+\Xi^0$ reconstructed) in comparison with data taken from Ref. [166] (red points).

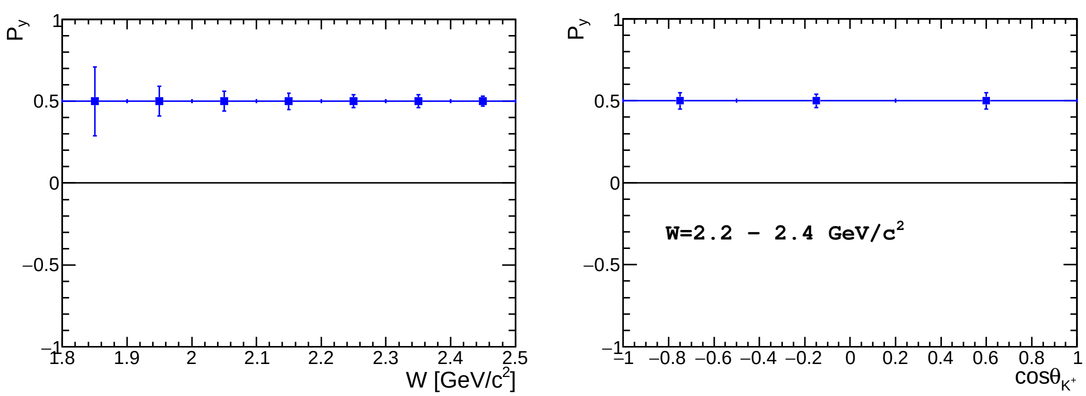


Figure 43: Estimates of the statistical uncertainties of the induced polarisation of the cascade as a function of W (one-fold differential) and $\cos\theta_{K^+}$ (two-fold diferential).

whole decay chain and establish the spin and parity of these excited states [167].

### 13.1.5 $K_L p \to K^+ n$ Reaction

The $K_L^0 p \to K^+ n$ reaction is a very special case in kaon nucleon scattering process. Due to strangeness conservation, formation of intermediate resonances is forbidden for this reaction. The main contribution comes from various non-resonant processes, which can be studied in a clean and controlled way. Similar non-resonant process can be seen in other reactions where they can interfere with hyperon production amplitudes distorting hyperon signals. That is why the knowledge of the non-resonant physical background is important, not only for the kaon-induced reactions but for all reactions with strangeness. The non-resonant nature of the reaction does not guarantee the absence of bumps in the total cross section: kaons and/or nucleons can be excited in the intermediate stage, producing bumps in the total cross section.

The reaction $K_L^0 p \to K^+ n$ is simple and it has a very high production cross section, see Fig. 44(left); nevertheless, the data on this reaction are scarce. It is a bit simpler to perform a positive kaon beam scattering for the inverse reaction, but the necessity of a neutron target with unavoidable many-body and FSI-effects complicates the data analysis. That is why the inverse reaction is also not so well known. There are a fair sample of differential cross section data in the range $0.5 < p_{K_L} < 1.5$ GeV/$c$ predominantly from bubble chambers, see Ref. [168], and a few measurements at high energies $p_k = 5.5$ GeV/$c$ [169], $p_k = 10$ GeV/$c$ [170]. In the energy range $2 < W < 3.5$ GeV, which can be covered by the KLF experiment with very high statistics, there are no data on this reaction at all.

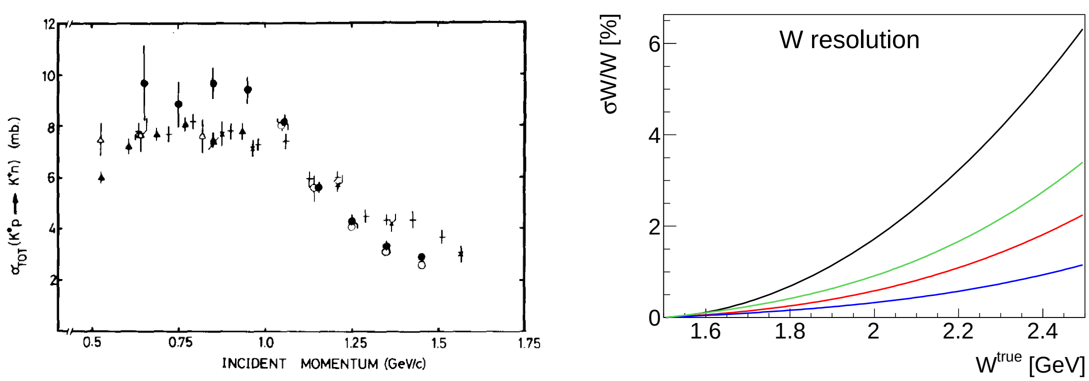


Figure 44: The total cross section for $K_L p \to K^+ n$ reaction as a function of $K_L$ momentum from Ref. [168] (left) and expected W resolution, $\sigma W/W$, depending on time-of-flight accuracy (right) for 300 ps (black), 150 ps (green), 100 ps (red), and 50 ps (blue), respectively.

It is enough to reconstruct the charged kaon to determine the reaction fully, provided that the beam resolution is good enough. The beam energy is determined by TOF technique utilizing the 16-m flight path between the kaon production beryllium target and the reaction hydrogen target. The beam resolution in this case is driven by the SC time resolution. The present SC time resolution leads to a 300 ps vertex time resolution. This time resolution can be easily improved to 150 ps or even 100 ps during a foreseen upgrade. In Fig. 44(right) one can see the expected $W$ resolution, $\Delta W/W$, for 300 ps (black), 150 ps (green), 100 ps (red), and 50 ps (blue) time resolutions. A full MC was performed for these simulations.

In addition to a kaon one could also detect a neutron; however, due to the poor neutron detection efficiency and the large systematic uncertainties associated with neutron detection we do not expect any improvement in reaction reconstruction in this case.

In 100 days of beamtime with $3 \times 10^4$ $K_L$/s on the target, we expect to detect around 200M $K_L p \to K^+ n$ events. A typical example of the expected statistics in comparison to previous data can be seen in Fig. 45(left). The highest flux is expected around $W = 3$ GeV, where we had to increase statistical errors by a factor of 10 to make them visible, see Fig. 45(right).

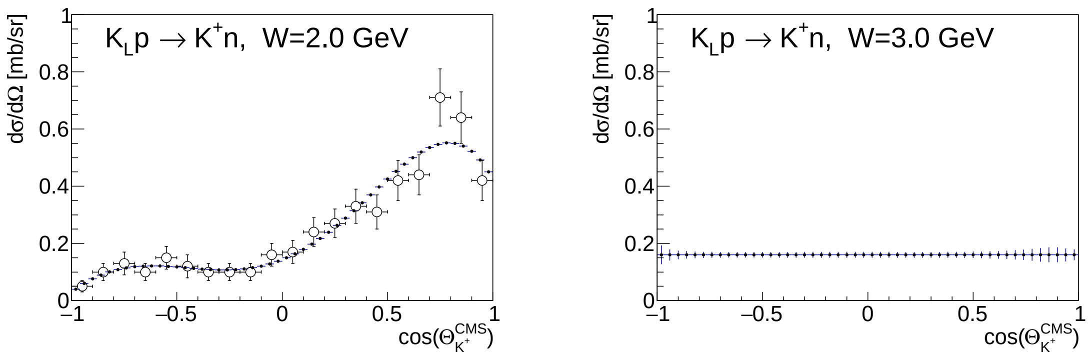


Figure 45: The cross section uncertainty estimates (statistics only) for $K_L p \to K^+ n$ reaction for the $W = 2$ GeV (left) in comparisson with data from Ref. [168] and $W = 3$ GeV (right). The errorbars for the right plot are increased by factor of 10 to make them visible.

There are three major sources of background: $np \to K^+ nn$, $np \to \pi^+ nn$, and $K_L p \to K^+ \Xi$. Neutron flux drops exponentially with energy (see Sec. 12.1.5.3 for details) and generally the high energy neutron flux is small, but non vanishing. If neutrons and $K_L$s have the same velocity they cannot be separated by time of flight. Neutron-induced reactions have high cross sections, which is why it is necessary to consider them as a possible source of background. Fortunately, neutron-induced kaon production contributes at the low level of $10^{-3}$, which, with missing-mass cuts, can be reduced below $10^{-4}$. Some of the pions from $np \to \pi^+ nn$ reaction can be misidentified as kaons, but with missing mass and time-of-flight cuts we can reduce the contribution of this background to a sub-per mill level. Detailed description of various backgrounds can be found in Appendix A3 (Sec 17). $K_L p \to K^+ \Xi$ has 100 times smaller cross section compared to $K_L p \to K^+ n$ and below $W < 2.3$ GeV can be completely filtered out by a $3\sigma$ $K^+$ missing-mass cut. At high $W$, there is some overlap. One can use conventional background subtraction techniques to eliminate it. The $\Xi$ often has charged particles in its decay chain, which can be used to veto the channel. Our studies show that the background from $\Xi \to \Lambda \pi^0 \to n \pi^0 \pi^0$ can be reduced below $10^{-4}$ level as well.

#### 13.1.6 Reaction $K_L p \to K \pi X$ (X = p or n)

It has to come soon.

## 13.2 Summary and Beam Time Request

Precise new data (both differential cross section and measuring recoil polarization of hyperons) for $K_Lp$ scattering with good kinematic coverage could significantly improve our knowledge of $\Lambda^*$, $\Sigma^*$, and $\Xi^*$ resonances. Clearly, a complete understanding of three-quark bound states requires learning about baryon resonances in the "strange" sector. Although not the focus of this stage of the KLF project, a $K_L$ beam facility would also be advantageous for studying $\Xi^*$ and $\Omega^*$ states via production processes. Polarization data are very important to measure in addition to differential cross sections to help remove ambiguities in PWAs. Unfortunately, the current data base for $K_Lp$ scattering includes very few polarization data. As noted here, several $K_Lp$ reactions are isospin-1 selective, which would provide a useful constraint for a combined PWA of $K_Lp$ and $K^-p$ reactions. Finally, the long lifetime of the $K_L$ compared with the $K^-$ would allow a larger beam flux on target, which would allow $K_Lp$ measurements to be made at lower energies than easily measurable with $K^-$ beams. It would be advantageous to combine all $K_Lp$ data in a new coupled-channel PWA with available and new J-PARC $K^-p$ data. We will also significantly improve world data for $K\pi$ PWA with an impact on other fields of particle physics. In Table 1, we summarize the expected statistics below $W = 3$ GeV during 100 days of the beam time.

Table 1: Expected statistics for different reactions with $LH_2$ and below W = 3 GeV during 100 days of the beam time.

| Reaction | Statistics (events) |
|---|---|
| $K_Lp \to K_Sp$ | 8M |
| $K_Lp \to \pi^+\Lambda$ | 24M |
| $K_Lp \to K^+\Xi^0$ | 4M |
| $K_Lp \to K^+n$ | 200M |
| $K_Lp \to K\pi X$ | ??M |

There are no data on the "neutron" target and for this reason, it is hard to make a realistic estimation of statistics specifically that there is so dramatical difference between model predictions (Sec. 10). Our assumption is that we may have similar statistics as proton target will give us. Then, we are asking PAC to double our beam time request – 100 days with $LH_2$ and 100 days with $LD_2$.

Ricent results for the open-flavor strong decays of strange baryons into a baryonvector/pseudoscalar meson pair [171] give us additional input in our study.

# 14 Cover Letter for KLF Proposal Submission to PAC45

This Proposal follows the Letter of Intent LoI12–15–001, *Physics Opportunities with Secondary $K_L$ beam at JLab* presented to PAC43 in 2015. The Issues and Recommendations included in the PAC43 Final Report document read as follow:

**Issues:** *It is not clear what this experiment can do that the J-PARC charged kaon program cannot* *do substantially better. An experimental concern is the transverse size of the KLF beam that must impinge on a 2-3 cm target. Backgrounds from neutrons and KLF outside the target acceptance may be important in event rates and signal to background rejection.*

**Recommendation:** *Any proposal would require full simulations of the beam line and detector to determine the effect of backgrounds from neutrons and kaons outside the target acceptance. But it is not clear to the committee if this experiment would in any way be competitive with J-PARC or a potential Fermilab or CERN program in this energy range. The superiority of a neutral beam and/or the GlueX detector for these measurements would need to be demonstrated before a future proposal would be considered favorably.*

The KLF Collaboration believes that this proposal addressed all the concerns following the recommendations expressed by the PAC43:

1. **Q1:** *It is not clear what this experiment can do that the J-PARC charged kaon program cannot do substantially better.*
   **A1:** The proposed $K_L$ beam intensity is similar to the proposed charged kaon beam intensity at J-PARC, so there is no reason to expect that J-PARC will do *substantially better*. Using different probes ($K_L$ for JLab and $K^-$ for J-PARC), in principle, we and J-PARC (if charged kaon beam proposal is approved) will be able to collect data for different reactions. To have full experimental information with different final states is important for the coupled channel analysis (here we have extensive experience) to determine hyperon parameters. The JLab and J-PARC measurements will be complementary.
   (i) As $c\tau(K^-) = 3.7$ m, while $c\tau(K_L) = 15.4$ m higher rate of low momenta kaons with $K_L$ beam may be an advantage.
   (ii) The proposed experiment will have $K_L$ beam with all momenta simultaneously ("kaon strahlung"), while J-PARC has to make many thousand settings to scan the full range of W distributions in different reactions.
   (iii) In the best case of scenario, J-PARC can start hyperon program in 2024. In Appendix A1 (Sec 15), we have presented the ability of other possible facilities as FNAL, J-PARC, Belle, BaBar, $\overline{P}$ANDA, and COMPAS to do a hyperon spectroscopy. We do not see a competition factor here for two reasons: a) some of above mentioned facilities may, but do not have yet have secondary kaon beams; b) even if such beams on these facilities are approved and constructed it will happen in a decade scale from today.

2. **Q2:** *An experimental concern is the transverse size of the KLF beam that must impinge on a 2-3 cm target. Backgrounds from neutrons and KLF outside the target acceptance may be important in event rates and signal to background rejection.*
   **A2:** First of all the collimated beam of $K_L$ will impinge on the cell of the $LH_2/LD_2$ target with $R = 3\ cm$ radius. All kaons outside of solid angle defined by collimators will be absorbed in a 4 m iron shielding in the sweeping magnet and concrete shielding in front of GlueX setup. Secondly, as it was shown by our detailed simulations, the rate of neutrons on GlueX target at momenta p > 1 GeV/$c$ are smaller than that of $K_L$. On the other hand, production of strange mesons with neutrons at low momenta kinematically can not occur due to the threshold, as to conserve the strangeness at least two kaons in the final state have to be produced. Therefore physics background from reactions initiated by neutrons are negligible.

The rate of neutrons irradiating GlueX setup outside of the target acceptance will be total on the level of $\sim$100/s with 90$\%$ in the range of energies below 20 MeV, therefore can not cause any background either.

From radiation point of view our MCNP6 transport code calculations have shown that the effect of radiation caused by neutrons is below the RadCon limit.

3. **Q3:** *Any proposal would require full simulations of the beam line and detector to determine the effect of backgrounds from neutrons and kaons outside the target acceptance.*
   **A3:** See our answers **A1** and **A2**.

4. **Q4:** *But it is not clear to the committee if this experiment would in any way be competitive with J-PARC or a potential Fermilab or CERN program in this energy range.*
   **A4:** See our answer **A1**.

5. **Q5:** *The superiority of a neutral beam and/or the GlueX detector for these measurements would need to be demonstrated before a future proposal would be considered favorably.*
   **A5:** Our MC simulations have shown that the proposed experiment will be able to improve available world proton target data by two orders of magnitude in statistics. The proposed experiment will provide first measurements on a neutron using $LD_2$ target. Coupled channel analysis using both proton and neutron target data promise to find many "missing" hyperons. We will also significantly improve world data on $K\pi$ PWA with an impact on other fields of particle physics.

   The summary of the potential of other facilities is summarized in Appendix A1 (Sec 15).

# 15 Appendix A1: Current Hadronic Projects

Past measurements involving kaon scattering measurements were made at a variety of laboratories, mainly in the 1960s and 1980s when experimental techniques were far inferior to the standards of today (short summary is given in Sec. 5). It is important to recognize that current projects are largely complementary to the proposed Jlab KL hadron beam facility. We summarize the status of the FNAL, J-PARC, Belle, BaBar, $\overline{P}$ANDA, and COMPAS efforts here.

## 15.1 Project X, USA

A status of Project X at FNAL [172, 173] is following: First stage of Project X aims for neutrinos. Proposed $K_L$ beam can be used to study rare decays and CP-violation [174]. It may be impossible to use FNAL $K_L$ beam for Hyperon Spectroscopy because of momentum range and $n/K_L$ ratio (columns 4 and 6 at Table 2). In particular, the 8-yr old FNAL LoI addressed to the CP-violation study proposed to have a neutral kaon beam rate of $10^{10}$/hr for high energies and very broad energy binning [175].

Table 2: Comparison of the $K_L$ production yield. The BNL AGS kaon and neutron yields are taken from RSVP reviews in 2004 and 2005. The Project X yields are for a thick target, fully simulated with LAQGSM/MARS15 into the KOPIO beam solid angle and momentum acceptance from Ref. [173].

| Project | Beam energy (GeV) | Target ($\lambda_I$) | p($K_L$) (MeV/$c$) | $K_L$/s (into 0.5 msr) | n/$K_L$ ($E_n$ >10 MeV) |
|---|---|---|---|---|---|
| BNL AGS | 24 | 1.1 Pt | 300–1200 | $60 \times 10^6$ | $\sim 1 : 1000$ |
| Project X | 3 | 1.0 C | 300–1200 | $450 \times 10^6$ | $\sim 1 : 2700$ |

## 15.2 J-PARC, Japan

While J-PARC has a whole program of charged strange particle and hypernuclear reactions, photon beam at GlueX KLF allows unique access to other channels J-PARC provides separated secondary beam lines up to 2 GeV/$c$ (Table 3). The operation of the Hadron Experimental Facility resumed in April of 2015 following to a two-year suspension to renovate the facility after the accident that occurred in May of 2013 [177]. The primary beam intensity is currently 25 kW, and will be increased to 100 kW in a while. This will correspond to $\sim 10^9$ ppp (particles per pulse) for pion beam intensity and to $\sim 10^6$ ppp for kaon beam flux. The $K/\pi$ ratio is expected to be close to 10, which is realized with double-stage electrostatic separators. One of the main problems in the $K/\pi$ separation is a high duty-factor of the J-PARC Complex.

Table 3: J-PARC Beam line specifications from Ref. [176].

| Beamline | Paricle | Momentum Range | Typical Beam Intensity (40 kW MR operation) |
|---|---|---|---|
| K1.8BR | $\pi^\pm$, $K^\pm$, and p,$\overline{p}$ (separated) | <1.1 GeV/$c$ | $1.5 \times 10^5$ $K^-$/spill at 1 GeV/$c$ |
| K1.8 | $\pi^\pm$, $K^\pm$, and p,$\overline{p}$ (separated) | <2.0 GeV/$c$ | $5 \times 10^5$ $K^-$/spill at 2 GeV/$c$ |
| K1.1 | $\pi^\pm$, $K^\pm$, and p,$\overline{p}$ (separated) | <1.1 GeV/$c$ | $1.5 \times 10^5$ $K^-$/spill at 1 GeV/$c$ |
| High-p | $\pi^\pm$, $K^\pm$, and p,$\overline{p}$ (unseparated) | up to 20 GeV/$c$ | $>\sim 10^7$ $\pi^-$/spill at 20 GeV/$c$ |
| | | | $>\sim 10^6$ $K^-$/spill at 7 GeV/$c$ |
| | Primary Proton | 30 GeV | $\sim 10^{11}$ proton/spill |

With $K^-$ beams, currently there is no proposal specific for $S = -1$ hyperons, but the cascades will be studied in the early stage of E50 [178], hopefully in this year, 2018. The $\Delta p/p$ is a few percent which is not good to look for narrow hyperons. One can think that the systematic study for $S = -1$ hyperons even with charged kaons is desirable and J-PARC folks think that such study is definitely needed but currently there is no room to accept a new proposal to require a long beam line. J-PARC is focusing on hypernuclei physics [179]. Unfortunately, the current J-PARC Hyperon Program does not propose to do polarized target measurements.

There is no $K_L$ beam line for hyperon physics at J-PARC. It is 100% dedicated to the study of CP-violation. The momentum is spread out from 1 to 4 GeV/$c$, there is no concept of $\Delta p/p$ since the beam cannot be focused with EM devices.

## 15.3 Belle, Japan

Belle Collaboration at KEK has plenty of $e^+e^-$ data, and people in Belle [Belle Nuclear Physics Consortium (Belle NPC)] are now extracting various charm-baryon decay processes, which can be used for cascade resonance spectroscopy, from those "raw" $e^+e^-$ data [180].

## 15.4 BaBar, USA

BaBar Collaboration at SLAC studied, for instance, properties of the $\Xi(1530)^0$ in the decay of $\Lambda_C^+ \to (\pi^+\Xi^-)K^+$ and $\Xi(1690)^0$ in the decay of $\Lambda_C^+ \to (\overline{K^0}\Lambda)K^+$ [181] (see, for instance, a recent overview by Ziegler [182]).

## 15.5 $\overline{P}$ANDA, Germany

The $\overline{P}$ANDA experiment [183] will measure annihilation reactions of antiprotons with nucleons and nuclei in order to provide complementary and in part uniquely decisive information on a wide range of QCD aspects. The scientific scope of $\overline{P}$ANDA is ordered into several pillars: hadron spectroscopy, properties of hadrons in matter, nucleon structure and hypernuclei. Antiprotons are produced with a primary protons beam, collected and phase-space cooled in the CR (Collector Ring), and then transferred to the HESR (High Energy Storage Ring) where they are stacked, further phase-space cooled, and then directed onto an internal target located at the center of the $\overline{P}$ANDA detector. The facility will start with a luminosity of $10^{31}\ cm^2/s$ and a momentum resolution of $\Delta p/p = 10^{-4}$, and later improve to $2 \times 10^{32}$ and $4 \times 10^{-5}$, respectively. The large cross section into baryon- antibaryon final states (e.g., $\sim 1\ \mu b$ for $\Xi\overline{\Xi}$ or $0.1\ \mu b$ for $\Omega\overline{\Omega}$) make spectroscopic studies of excited multi-strange hyperons a very compelling part of the initial program of $\overline{P}$ANDA, which is expected to commence by 2025 [184].

## 15.6 COMPAS, Switzerland

COMPASS is thinking of the physics using an RF separated beam of charged kaons. It is in the stage of discussion. The rates, which were presented as a very first guess by the CERN beamline group were very interesting for a strangeness physics program via diffractive production of strange resonances [185]. However, the cost of a RF seperated beam is high. But, something like this had been built in the past.

Charged kaons could be used to extend the XhiPT investigations into the strangeness sector (e.g., Primakoff) and the spectroscopy program. At present, COMPAS filters out kaons in the COMPASS charged pion beam via Cherenkovs but they make up only about 2.6% of all beam particles.

The energy of the kaon beam would probably below 100 GeV but above 40 – 50 GeV. The latter number is defined by the stability of the power supplies for the beam line, which after all is about 1 km long... and of course the decay losses.

# 16 Appendix A2: Additional Physics Potential with a $K_L$ Beam

As stated on the summary of Mini-Proceedings of the Workshop on Excited Hyperons in QCD Thermodynamics at Freeze-Out (YSTAR2016) [186]: a very interesting further opportunity for the KL facility is to investigate KL reactions on complex nuclei. By selecting events with the appropriate beam momentum together with a fast forward going pion, events can be identified, in which a hyperon is produced at low relative momentum to the target nucleus or even into a bound state. Baryons with strangeness embedded in the nuclear environment, hypernuclei or hyperatoms, are the only available tool to approach the many-body aspect of the three-flavor strong interaction. Furthermore, appropriate events with a forward going $K^+$ could deposit a double-strange hyperon into the remaining nucleus, potentially enabling searches for and studies of double Lambda hypernuclei.

Similarly, the scattering of kaons from nuclear targets could be a favorable method to measure the matter form factor (and therefore neutron skin) of heavy nuclei, with different and potentially smaller systematics than other probes. The character of the neutron skin, therefore, has a wide impact and the potential to give important new information on neutron star structure and cooling mechanisms [187–191], searches for physics beyond the standard model [192, 193], the nature of 3-body forces in nuclei [194, 195], collective nuclear excitations [196–199] and flows in heavy-ion collisions [200, 201]. Theoretical developments and investigations will be required to underpin such a program, but the science impact of such measurements is high.

Further potential exists to search for – or exclude – possible exotic baryonic states that can not easily be described by the usual 3 valence quark structure. Recent results from LHCb provide tantalizing hints for the existence of so-called pentaquarks that include a charm valence quark, however the interpretation of those results is under discussion. In contrast, elastic scattering of $K_L$ with a hydrogen target gives unambiguous information on the potential existence of such states. With the given flux of $K_L$ at the proposed facility, a clear proof of existence or proof of absence will be obtained within the integrated luminosity required for the excited hyperon spectroscopy program that forms the basis of this proposal.

There are two particles in the reaction $K_Lp \to \pi Y$ and $KY$ that can carry polarization: the target and recoil baryons. Hence, there are two possible double-polarization experiments: target/recoil. The total number of observables is 3. The formalism and definitions of observables commonly used to describe the reaction $K_Lp \to KY$ is given in Sec. 6. Although one cannot easily measure recoil polarization with GlueX, the self-analyzing decay of hyperons makes this possible. Double polarization experiments, using, e.g., a polarized target like FROST [158], will however be left for future proposal(s).

The physics potential connected with studies of CP violating decays of the $K_L$ is very appealing, however that topic is not currently the focus of this proposal, since a detailed comparison with the competition from existing and upcoming experiments is needed in order to identify the most attractive measurements that could be done at the proposed KL facility at the Jefferson Laboratory.

# 17 Appendix A3: Details of Monte Carlo Study

## 17.1 Particle Identification

For each topology, one primary particle (the proton for the $pK_S$ channel, the $\pi K^+$ for the $\Lambda\pi^+$ channel and the $K^+$ for the $K^+\Xi$ and $K^+n$ channels) provides a rough determination for the position of the primary vertex along the beam line that is used in conjunction with the start counter to determine the flight time and path of the $K_L$ from the beryllium target to the hydrogen target. Protons, pions, and kaons are distinguished using a combination of dE/dx in the chambers and time-of-flight to the outer detectors (BCAL and TOF). The energy loss and timing distributions for the $pK_S$ channel are shown in Fig. 46; the distributions are similar for the $\Lambda\pi^+$ channel, where a proton band arises from the $\Lambda \to p\pi^-$ decay channel. Also shown is the dE/dx distribution for the $K^+\Xi$ channel, where a prominent kaon band can be seen, along with pion and proton bands arising from $\Lambda$ decays.

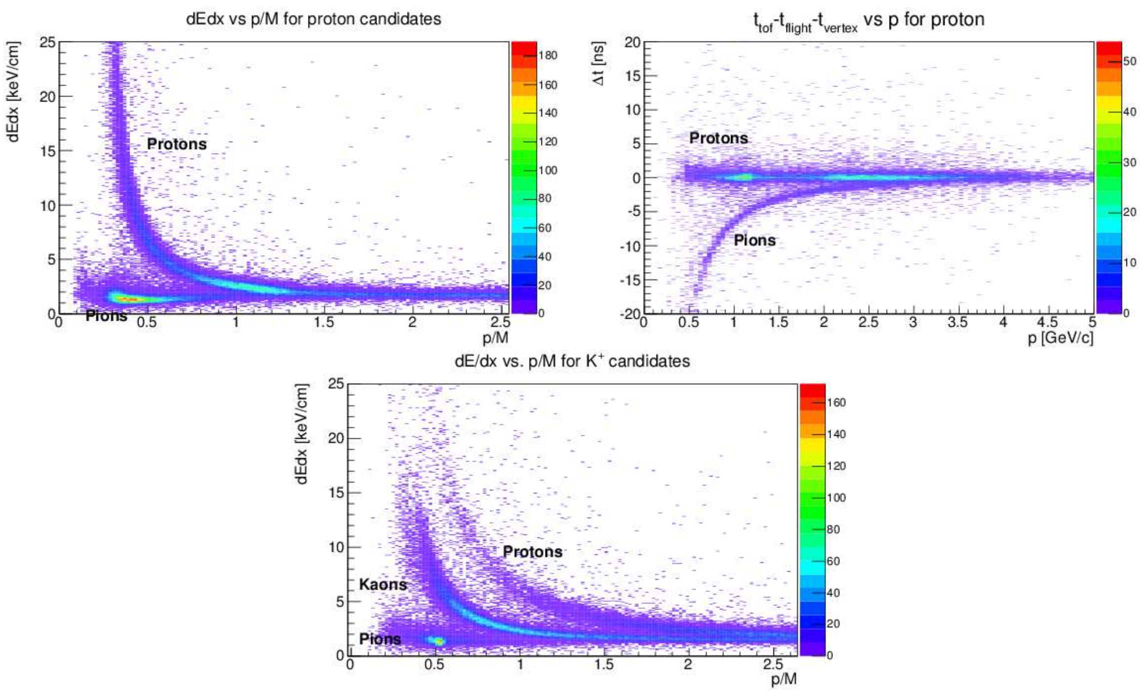


Figure 46: Particle identification. Top left: dE/dx for the $pK_S$ channel. Top right: time difference at the primary "vertex" for the proton hypothesis for the $pK_S$ channel using the TOF. Bottom plot: dE/dx for the $K^+\Xi$ channel. The proton and pion bands arise from the decay of the $\Lambda$.

Since the GlueX detector has full acceptance in $\phi$ for charged particles and large acceptance in $\theta$ (roughly $1 - 140°$), reconstruction of full events is feasible for the majority of the chanels. That allow to apply four or more overconstrain kinematical fit and improve the resolution considerably. A typical comparison between $W$ reconstruction using the $K_L$ momentum for 300 ps SC resolution and the other using kinematically fitted final state particles for the $pK_s$ channel is shown in Fig. 47.

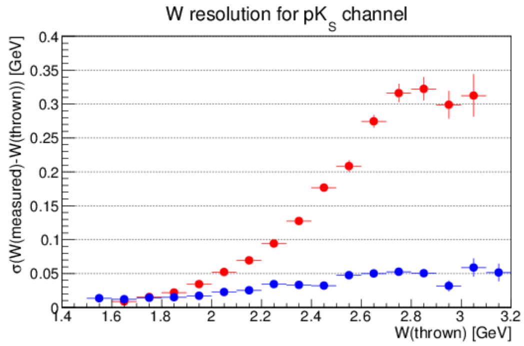


Figure 47: $W$ resolution for the $pK_S$ channel.

#### 17.1.1 Details of MC study for $K_L p \to K_S p$

For the $pK_S$ channel, we take advantage of the BR of $69.2\%$ for $K_S \to \pi^+\pi^-$ [1]: the invariant mass of the $\pi^+\pi^-$ pair and W as computed from the four-momenta of the proton and the two pions is shown in Fig. 48.

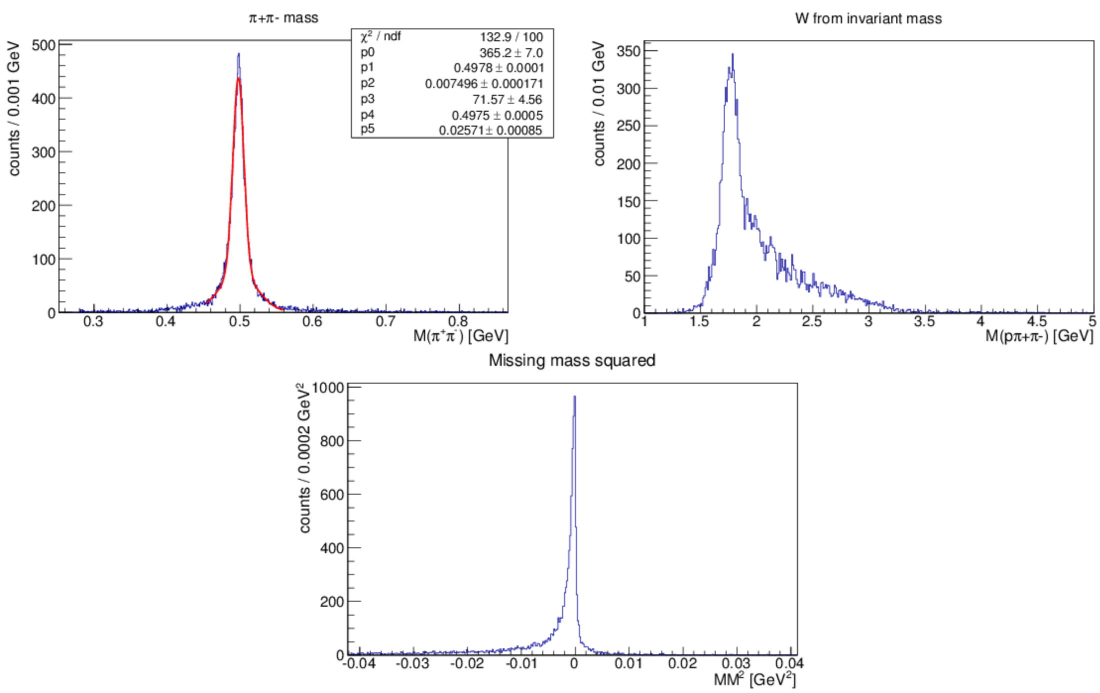


Figure 48: Full reconstruction for $K_L p \to pK_S$ and $K_S \to \pi^+\pi^-$. Top left: $\pi^+\pi^-$ invariant mass. Top right: W computed from $p\pi^+\pi^-$ invariant mass. Bottom plot: Missing mass squared for the full reaction.

After combining the four-momenta of the final state particles with the four-momenta of the beam and the target, the missing mass squared for the full reaction should be zero, which is also shown in Fig. 48. Finally, one require conservation of energy and momentum in the reaction by applying a kinematic fit to the data. After applying a 0.1 cut on the confidence level of the fit, one computed an estimate for the reconstruction efficiency as a function of $W$ as shown in Fig. 49. Here the efficiency includes the BR for $K_S \to \pi^+\pi^-$. The average reconstruction efficiency is about $7\%$.

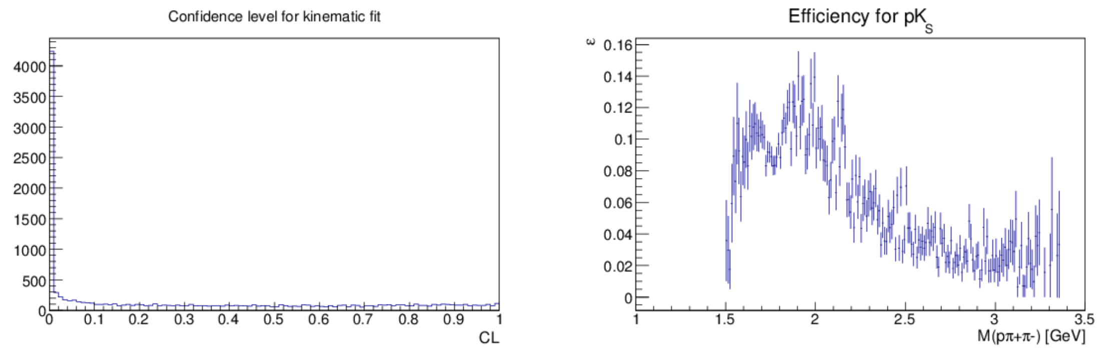


Figure 49: Left plot: Confidence level distribution for kinematic fit for the $pK_s$ channel. Right plot: Estimate for efficiency for full reconstruction of the $K_l p \to pK_S$ and $K_S \to \pi^+\pi^-$ reaction chain as a function of W.

### 17.1.2 Details of MC study for $K_L p \to \pi^+\Lambda$

We have utilized the phase-space event generator for $\pi^+$, $\Lambda$ particles, then $\Lambda$ decays into proton, $\pi^-$ in the GEANT detector simulation step with decay ratio of 64% which is defined in the standard GEANT decay library. After detector simulation, we applied the detector smearing factors to implement detector resolutions into all Monte Carlo events. Once a smearing process is done, all events went through Hall-D JANA reconstruction program. Through entire simulation steps, we estimated the event rate and reconstructed momentum and mass resolution of $K_L p \to \pi^+\Lambda$ reaction. Figure 50 shows an example of plot for polar angle versus momentum distribution of $\pi^+$, $\pi^-$ and protons from the generated event (left) and reconstructed event (right).

### 17.1.3 Details of MC study for $K_L p \to K^+\Xi^0$

Three topologies can be used to reconstruct this reaction. Topology 1 requires the detection of a $K^+$, topology 2 requires the detection of a $K^+$ and a $\Lambda$ by utilising its high branching ration to a $p\pi^-$ pair (63.9%), and Topology 3 requires the detection of the two-photon decay of the $\pi^0$ from $\Xi \to \pi^0\Lambda$. Particle identification is done via a probabilistic approach involving $dE/dX$, time-of-flight, and track curvature information as described in Appendix A3 (Sec. 17.1). The $dE/dX$ distributions for kaon, proton, and negative pion candidates are shown in Fig. 51.

At low particle momenta, kaons and protons can be well separated, but high energy particles cannot be unambiguously differentiated neither by $dE/dX$ nor ToF information leading to missidentification. The higher the $W$, the higher ejectile energy we have and the more missidentification contribution we have. In this analysis (specifically Topology 2 and 3), these events are largely removed from an invariant-mass cut on the $p\pi^-$ pair.

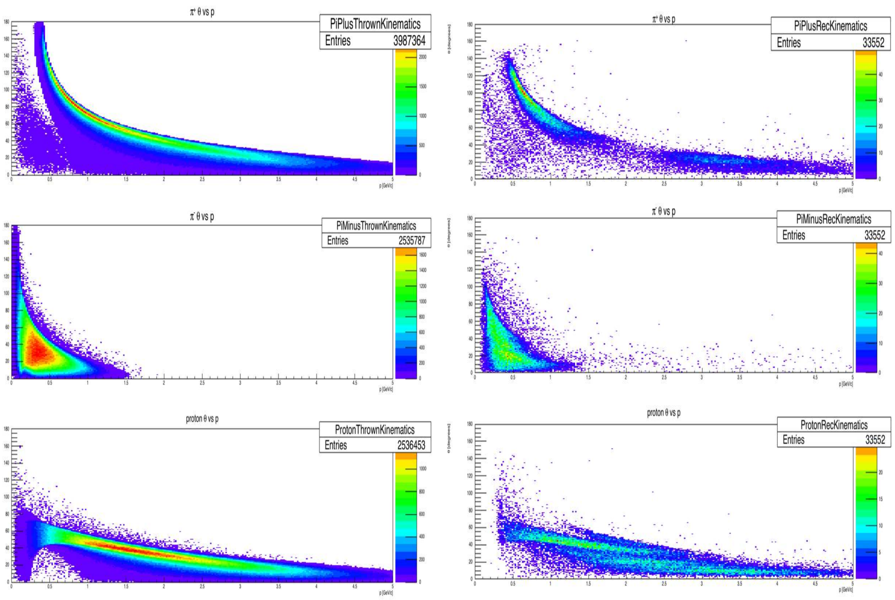

Figure 50: Momentum and angular distributions of $\pi^+$ (top row), $\pi^-$ (middle row) and proton (bottom row) of the reaction: generated (left column), reconstructed (right column) events.

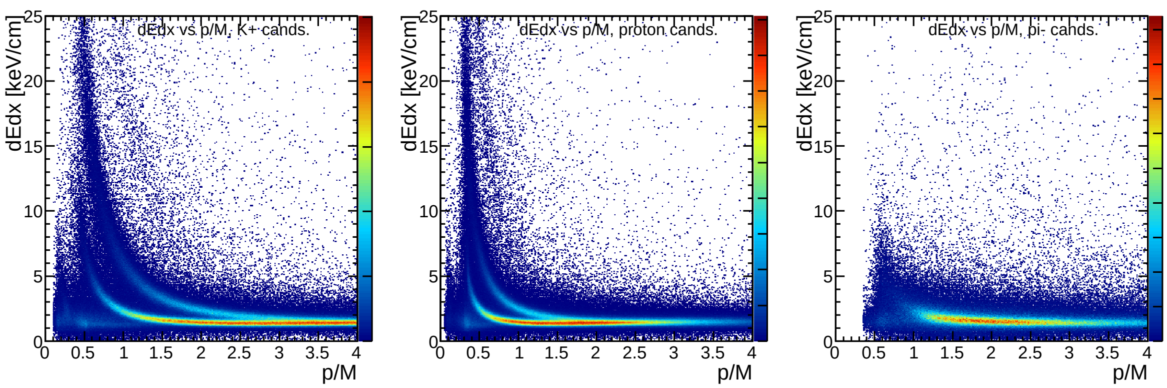


Figure 51: $dE/dX$ distributions used in kaon proton and negative pion identification for the reconstruction of $K_Lp \to K^+\Xi^0$.

Figure 52 shows the missing mass of $K_Lp \to K^+X$ for simulated data for the reaction $K_Lp \to K^+\Xi^0$ used in the reconstruction of all topologies, the invariant-mass distribution of the $p\pi^-$ pair used to reconstruct Topology 2 ($K_Lp \to K^+\Lambda X$) and 3, and the invariant-mass of the two-photon pair used to reconstruct Topology 3 ($K_Lp \to K^+\Lambda\pi^0$). A $3\sigma$ cut on these distributions allows us to fully reconstruct the reaction. The left panel of Fig. 52 shows the $3\sigma$ $W$-dependent cut applied to select the missing $\Xi^0$ as well as the $W$-dependent $3\sigma$ cut to reconstruct the reaction $K_Lp \to K^+n$ (see Appendix A3 (Sec. 17.1.4) for more details on the sources of resolution effects on the missing mass). The latter is one of the major sources of background for our reaction for Topology 1, however the missing-mass resolution (obtained with a vertex-time resolution of 150 ps) allows a clean separation of these two reactions up to $W = 2.3$ GeV. Above this value, special treatment of the

$K_L p \to \pi^+ n$ background is required as discussed in greater detail in Appendix A3 (Sec. 17.1.3).

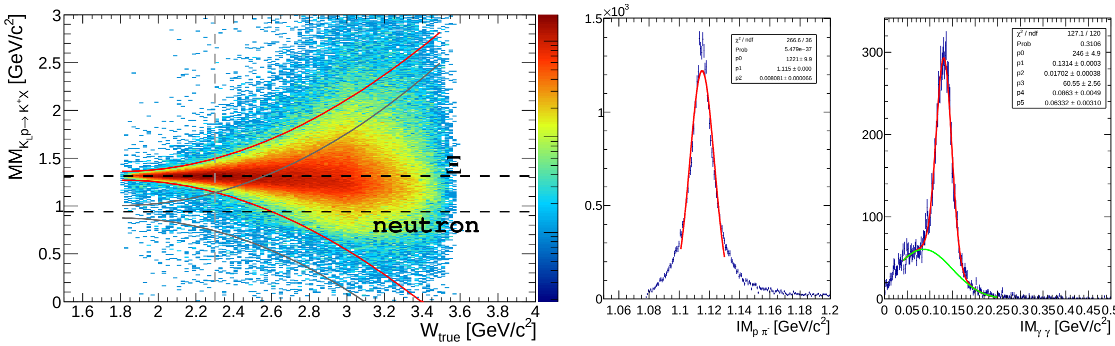


Figure 52: The missing mass of the reaction $K_L p \to K^+ X$ used to reconstruct the reaction $K_L p \to K^+ \Xi^0$ (Tpology 1), and the invariant mass of $p\pi^-$ pair (Tpology 2), and the invariant mass of the two-photon pair (Tpology 3).

The detection efficiency as a function of the true $W$ for each topology is shown in Fig. 53. As expected the efficiency is highest for Topology 1 reaching a maximum at 60% for W=2.05 GeV. The efficiency for topology 2 is about an order of magnitude less than Topology 1, and Topology 3 detection efficiency is on average 0.8%.

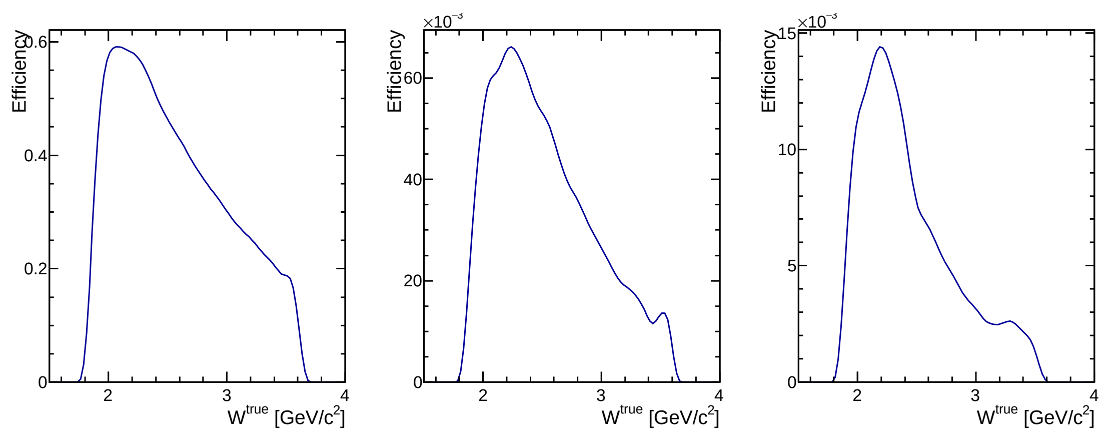


Figure 53: The detection efficiency for the reaction $K_L p \to K^+ \Xi^0$ for each topology.

**$K_L p \to K^+ \Xi^0$ background suppression:** Different sources of background will contribute in the 3 topologies used to study this reaction. Disentangling our signal $K_L p \to K^+ \Xi^0$ from the reaction $K_L p \to K^+ n$ (for Topology 1), which has two order of magnitude larger cross-section is expected to be relatively straightforward. As mentioned before, a simple missing-mass cut is sufficient to remove any contributions from this reaction for $W < 2.3$ GeV. For $W > 2.3$ GeV, an s-weight approach (or neuralNets, etc.) can be utilised to remove these contribution as the shape of the background under any cascade events can be well established from simulations. Figure 54 shows the $W$-dependence of the missing-mass distribution of $K_L p \to K^+ X$ for the simulated reactions $K_L p \to K^+\Xi^0$ and $K_L p \to K^+ n$ (left panel). The right panel shows the missing-mass projection at W=1.9 GeV. In addition to $K_L p \to K^+ n$, the reaction $K_L p \to \pi^+\Lambda$ is also a source

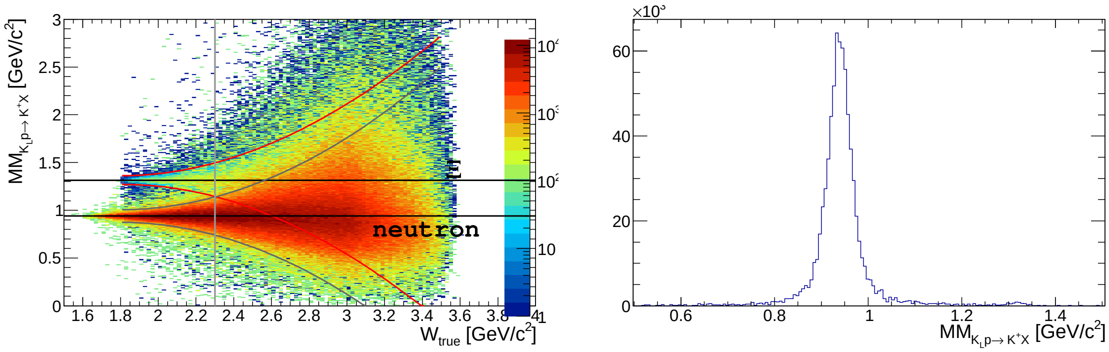


Figure 54: The missing mass of the reaction $K_L p \to K^+ X$ used to reconstruct the reactions $K_L p \to K^+\Xi^0$ (Topology 1) and $K_L p \to K^+ n$ (which has about 2 orders of magnitude larger cross section). Right panel shows the missing mass at W=1.9 GeV.

of background events for Topology 1 ($K_L p \to K^+ X$) and 2 ($K_L p \to K^+\Lambda X$). This channel contributes when the final state $\pi^+$ is miss-identified as a $K^+$. This shifts the missing-mass of $K_L p \to \pi^+ X$ to lower values than the ones expected leading to a good separation of this source of background below $W 2.2$ GeV. Figure 55 shows the missing-mass distribution of these miss-identified events. Contributions from these events for Topology 3 is completely removed by the requirement of two photons in the final state that reconstruct the mass of $\pi^0$. For topology 2, coplanarity cuts between the reconstructed (miss-identified) $K^+$ and $\Lambda$ can reduce contributions, where as a background subtraction approach using the missing-mass information can be used to remove any contribution at $W > 2.2$ GeV.

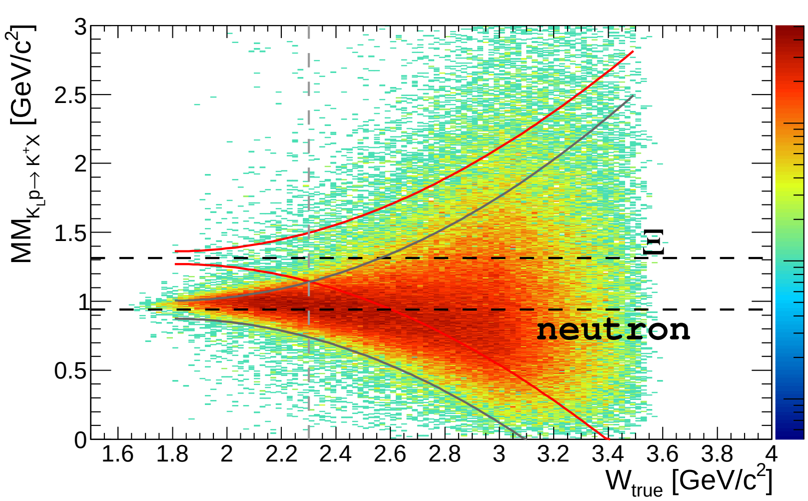


Figure 55: The missing mass of the reaction $K_L p \to K^+ X$ for simulated events from the reaction $K_L p \to \pi^+\Lambda$. The reconstructed events here results from a pion miss-identified as kaon.

$\Xi^0$ **induced polarisation:** The parity violating nature of the cascade's weak decay ($\Xi^0 \rightarrow \pi^0\Lambda$) yiels a pion angular distribution given by

$$n(\theta_\pi^y) = \frac{N}{2}(1 - P_\Xi^y \alpha \cos\theta_\pi^y), \tag{26}$$

where $P_\Xi^y$ is the induced polarisation of the cascade, and is the analysing power $\alpha = 0.406 \pm 0.013$ [1]. Figure 56 shows the production plane defined in the centre-of-momentum system containing the incoming $K_L$ and proton target. The decay plane is defined in the rest-frame of the cascade and contains its decay products.

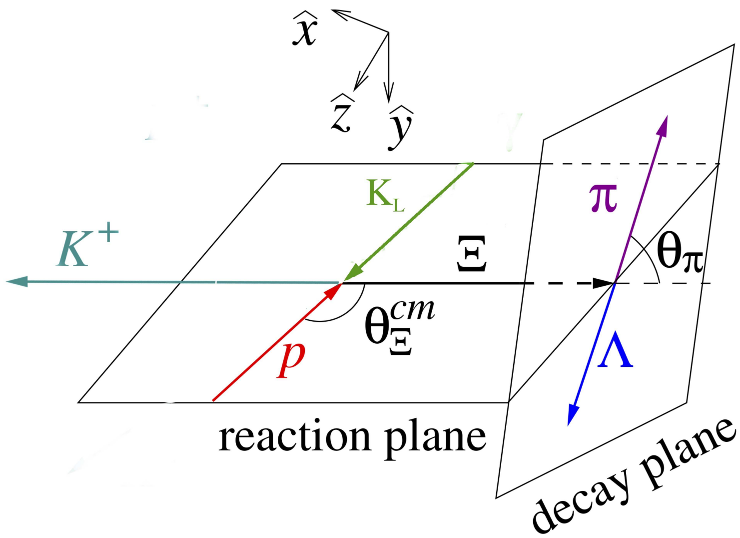


Figure 56: The production plane form $K_L p \rightarrow K^+\Xi^0$ defined in the centre-of-momentum system containing the incoming $K_L$ and proton target. The decay plane is defined in the rest-frame of the cascade and contains its decay products. The induced polarisation $P_\Xi^y$ is defined to lie perpendicular to the reaction plane.

In terms of four-vectors this reaction is written as follows:

$$\mathcal{P}_{K_L} + \mathcal{P}_p = \mathcal{P}_{K^+} + \mathcal{P}_{\Xi^0} \tag{27}$$

The production plane is then defined by

$$\hat{y} = \frac{\vec{P}_\Xi \times \vec{P}_{K_L}}{|\vec{P}_\Xi \times \vec{P}_{K_L}|}. \tag{28}$$

The $\hat{z}$ axis lies along the beam direction

$$\hat{z} = \frac{\vec{P}_{K_L}}{|\vec{P}_{K_L}|}, \tag{29}$$

and thus the $\hat{x}$ axis is defined to give the right-handed coordinate system

$$\hat{x} = \hat{y} \times \hat{z}. \tag{30}$$

The determination of $P_{\Xi}^{y}$ can be established by linear fits to the acceptance-corrected pion angular ($\cos\theta_{\pi}^{y}$) yields. Fitting these distributions with a first degree polynomial

$$y = a_0(1 + a_1 \cos\theta_{\pi}^{y}) \tag{31}$$

allows the determination of $a_1$, which gives us the the induced polarisation

$$a_1 = P_{\Xi}^{y}\alpha. \tag{32}$$

Alternatively, one can determine the induced polarisation transfer from determining the forward-backward asymmetry $A^y$ of the pion angular distribution. This asymmetry is defined as

$$A^y = \frac{N_+^y - N_-^y}{N_+^y + N_-^y}, \tag{33}$$

where $N_+^y$ and $N_-^y$ are the accepted corrected yields with $\cos\theta_{\pi}^{y}$ positive and negative respectively. The asymmetry is related to the induced polarisation by

$$P_{\Xi}^{y} = \frac{-2A^y}{\alpha}. \tag{34}$$

The statistical uncertainty in the asymmetry measurement of $P_{\Xi}^{y}$ is related to the Poisson uncertainty in $N_+^y$ and $N_-^y$. Propagating this uncertainty to the uncertainty of $A^y$ gives

$$\sigma_{A^y} = \frac{2}{(N_+^y + N_-^y)^2}\sqrt{N_+^y N_-^y (N_+^y + N_-^y)}. \tag{35}$$

The uncertainty in $P_{\Xi}^{y}$ is then found by propagating $\sigma_{A^y}$ and $\sigma_\alpha$

$$\frac{\sigma P_{\Xi}^{y}}{P_{\Xi}^{y}} = \sqrt{(\frac{\sigma_{A^y}}{A^y})^2 + (\frac{\sigma_\alpha}{\alpha})^2}. \tag{36}$$

#### 17.1.4 Details of MC study for $K_L p \to K^+ n$

As described in Section 13.1.5 we used only $K^+$ detection to reconstruct this reaction. Kaon identification is done with probabilistic approach involving $dE/dX$, time of flight and track curvature informations, see Appendix A3 (Sec. 17.1) for further details. Even in pure $K_L p \to K^+ n$ MC case one can have more than one charge track reconstructed due to various reactions in the detector volume. That is why in addition to pronounce $K^+$ banana on Fig. 57(left) we see some traces of pion and proton bands. At low $K^+$ momenta, kaons can be well separated from pions and protons, but high energy particles cannot be differentiated neither by $dE/dX$ nor ToF information leading to missidentification. The higher the $W$, the higher ejectile energy we have and the more kaons we loose due to missidentification see Fig. 57(right, green). In our analysis, we restrict ourselves to one and only one reconstructed charged track. This condition helps to suppress the background, but does not reduce the reconstruction efficiency, see Fig. 57(right, black).

Charge track detection efficiency stays flat over the full range of W's, but kaon reconstruction efficiency drops from about 60% at low W to 20% at highest available energy. Since GlueX

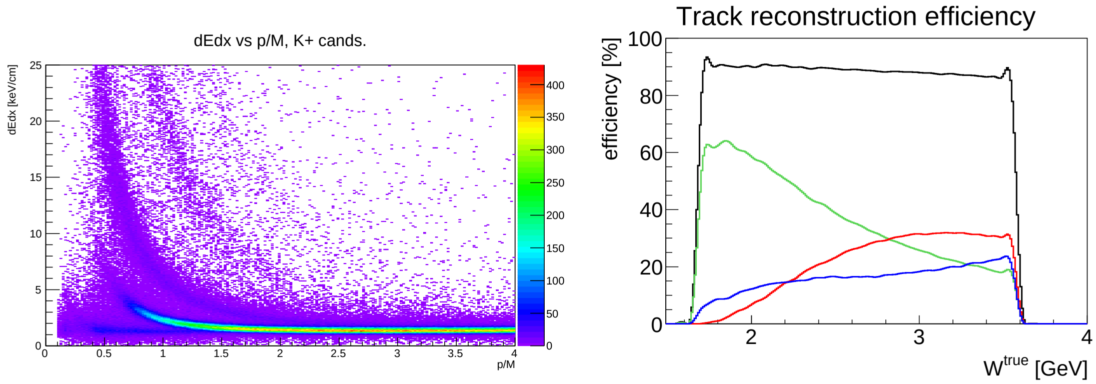


Figure 57: Left plot: dE/dx for the $K_L p \to K^+ n$ channel. Right plot: single charge track detection efficiency as a function of W for the $K_L p \to K^+ n$ channel. Any charged particle (black), kaon (green), proton (red), pion (blue).

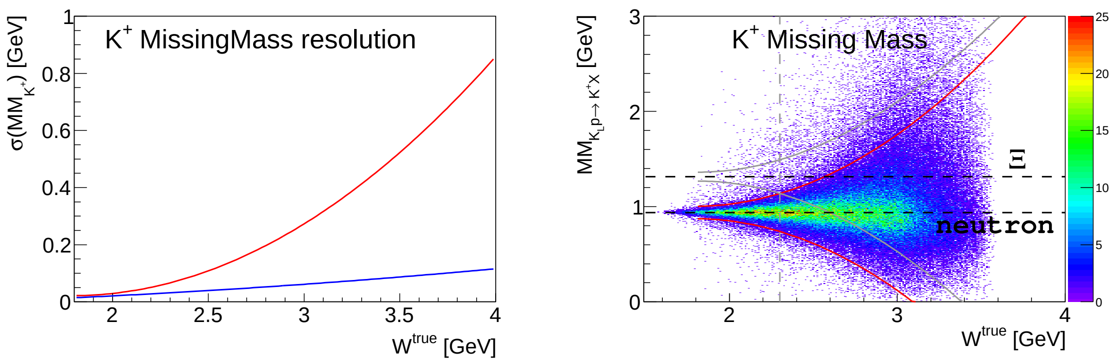


Figure 58: Left plot: full (red) and detector related (blue) $K^+$ missing mass resolution in terms of sigma. In second case true $K_L$ momentum is used to calculate missing mass. Right plot: $K^+$ missing mass resolution as a function of W. Three sigma missing mass cuts for the $K_L p \to K^+ n$ (red) and $K_L p \to K^+ \Xi$ (grey) reactions are indicated by solid lines. Horizontal dashed lines show nominal masses of neutron and $\Xi$ baryon. Vertical grey dashed line indicates the rang of pure missing mass separation between these two reactions

.

acceptance is large and essentially hole-less, kaon reconstruction efficiency does not depend on yet unknown angular distributions. For the final selection of the $K_L p \to K^+ n$ reaction we use $3\sigma$ missing mass cut around neutrons mass, see Fig. 58.

Figure 58 is plotted under assumption of 150 ps vertex time resolution. Both $W$ (Fig. 44) and missing mass resolutions are driven by the $K_L$ momentum resolution. That is why start counter update is essential. Any further time resolution improvement, below 150 ps, would significantly simplify reaction analysis and background suppression for all reactions of interest.

Below $W = 2.3\ GeV$, $K_L p \to K^+ n$ and $K_L p \to K^+ \Xi$ reactions can be disentangled by $K^+$ missing mass only. Above this value, special treatment of the $K_L p \to K^+ \Xi$ background is required. One may notice that a three sigma cut for the $K_L p \to K^+ n$ reaction rises faster than for

$K_L p \to K^+\Xi$. This effect has purely kinematical reason - due to higher mass of $\Xi$ baryon, $K^+$ produced in $K_L p \to K^+\Xi$ reaction has lower energy for the same value of W. The lower $K^+$ energy we have the better missing mass resolution we get and the more narrow the missing mass cut one needs to apply.

$K_L p \to K^+ n$ **background suppression:** Due to very high cross section, the $K_L p \to K^+ n$ is essentially background free. Due to extremely high statistics expected in this channel our uncertainties will be dominated by systematics. We have identified three major sources of physical background: $np \to K^+ nn$, $np \to \pi^+ nn$, and $K_L p \to K^+\Xi$ reactions.

Details on $K_L p \to K^+ n$ and $K_L p \to K^+\Xi$ separation one can find in Appendix A3 (Section **??**). Below W<2.3 GeV these two reactions can be separated by three sigma $K^+$ missing mass cut. Above W>2.3 GeV one can use standard background suppression techniques - S-weights, Q-weights, NeuralNets, etc... The main decay branch of $\Xi$ is $\Xi \to \Lambda\pi^0 \to p\pi^-\pi^0$ leads to several charged particles in the final state besides $K^+$, hence filtered out by "one charge track only" selection condition. Another decay branch $\Xi \to \Lambda\pi^0 \to n\pi^0\pi^0$ cannot be filtered out that easy, however due to smaller branching ratio combining with small $K_L p \to K^+\Xi$ production cross-section this channel contribute at the level of $10^{-3}$ only even without any background suppression techniques. Further suppression vetoing multiple neutral tracks and/or Q-weight push this background far below $10^{-4}$.

Neutron flux drops exponentially with energy (see Sec. for details) and generally the high energy neutron flux is small, but non vanishing. If neutrons and $K_L$s have the same velocity they cannot be separated by time of flight. Neutron induced reactions have high cross-sections that is why one needs to consider them as a possible source of background. On Figure, one can see a comparison of kaon and neutron fluxes for the worse case scenario when no neutron suppression is employed, similar to Fig. 19(right) in terms of $\beta$. Particles with the same $\beta$ cannot be separated by time of flight. At $\beta = 0.95$ neutron and kaon fluxes become equal. This velocity corresponds to a neutron momentum of $p_n = 2.9$ GeV/$c$ and kaon momentum of $p_K = 1.5$ GeV/$c$.

To evaluate the amount of background, we need to fold this flux with production cross-section and reconstruction efficiency. Let's first consider the $np \to K^+\Lambda n$ background. Unfortunately this reaction is not very well measured, so we would use the $pp \to K^+\Lambda p$ cross-section parametrisation together with the knowledge of $\frac{\sigma(pp\to K^+\Lambda p)}{\sigma(np\to K^+\Lambda n)} = 2$ from Ref. [202]. On Fig. 60, one can see the flux of $K^+$s from kaon induced $K_L p \to K^+ n$ reaction in comparison to a neutron induced $np \to K^+\Lambda n$ as a function of projectile velocities.

As one can see on Figure 60, neutron induced $K^+$ production contribute at very narrow range of energies. The contribution is also very small. One can further suppress this type of background vetoing charge particles from $\Lambda$ decay and performing a $K^+$ missing mass cut. All together one can suppress this type of background below $10^{-4}$.

The most dangerous type of neutron induced background originates from $np \to \pi^+ nn$ reaction with fast $\pi^+$ misidentification as $K^+$. There are no measurements of $np \to \pi^+ nn$ reaction but due to isospin symmetry one can relate this reaction to an isospin symmetric case $np \to \pi^- pp$. The later reaction is known, see Ref. [203]. The total cross-section for this reaction is in the order

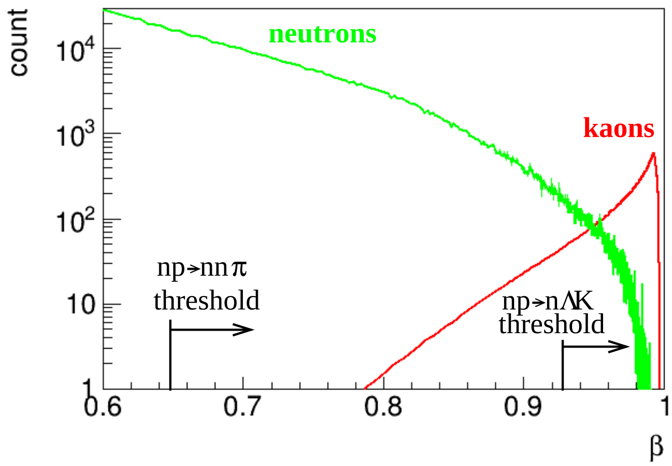


Figure 59: Neutron and $K_L$ fluxes as a function of velocity $\beta$.

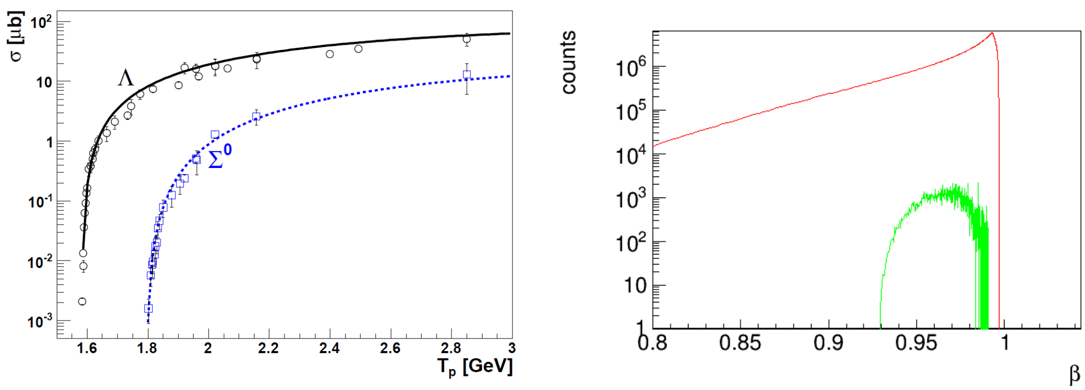


Figure 60: Left plot: $pp \to K^+\Lambda p$ total cross section from Ref. [202]. Right plot: $K^+$ flux as a function of projectile velocity for neutron (green) and kaon (red) induced reactions.

of 2mb. The $np \to \pi^+nn$ reaction has much lower threshold compare to $np \to K^+\Lambda n$, so it can utilize enormous flux of low-energy neutrons. However low energy neutrons predominately produce low energy pions, which can be separated from kaons. The background needs to be considered only for $\beta > 0.8$, see Fig. 61. The background level looks much higher compare to Fig. 60, but it can be severely suppressed with the "$K^+$" missing mass cut, since pion kinematics of three body $np \to \pi^+nn$ reaction is very different from $K_Lp \to K^+n$.

Kaon particle identification together with simple three sigma missing mass cut and assumption of $K_L$ beam can efficiently suppress all physical backgrounds of the $K_Lp \to K^+n$ reaction.

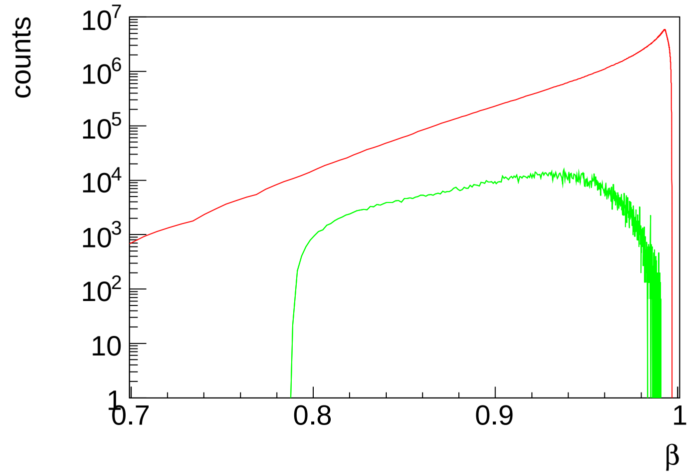


Figure 61: $K^+$ flux as a function of projectile velocity for the $np \to \pi^+ nn$ (green) and $K_L p \to K^+ n$ (red) reactions. Pion missidentification efficiency for the neutron induced reaction is extracted from the full MC-Geant simulation.

# References


[1] C. Patrignani *et al.* (Particle Data Group), Chin. Phys. C **40**, 100001 (2016).

[2] B.M.K. Nefkens, $\pi N$ Newsletter, **14**, 150 (1997).

[3] R. Koniuk and N. Isgur, Phys. Rev. Lett. **44**, 845 (1980).

[4] *The 2015 Long Range Plan for Nuclear Science*, http://science.energy.gov/np/nsac/ .

[5] H. Al Ghoul *et al.* (GlueX Collaboration), AIP Conf. Proc. **1735**, 020001 (2016), *Proceedings of the 16th International Conference on Hadron Spectroscopy* (Hadron2015), Newport News, VA, Sept. 2015, edited by M. Pennington.

[6] A. AlekSejevs *et al.* (GlueX Collaboration), arXiv:1305.1523 [nucl–ex].

[7] Y. Qiang, Ya.I. Azimov, I.I. Strakovsky, W.J. Briscoe, H. Gao, D.W. Higinbotham, and V.V. Nelyubin, Phys. Lett. B **694**, 123 (2010).

[8] W.J. Briscoe, M. Döring, H. Haberzettl, D.M. Manley, M. Naruki, I.I. Strakovsky, and E. Swanson, Eur. Phys. J. A **51**, 129 (2015)

[9] Web page of the Workshop on *Physics with Neutral Kaon Beam at JLab* (KL2016), JLab, Newport News, VA, USA, Feb. 2016: https://www.jlab.org/conferences/kl2016/ contains presentations.

[10] Web page of the Workshop on *Excited Hyperons in QCD Thermodynamics at Freeze-Out* (YSTAR2016), JLab, Newport News, VA, USA, Nov. 2016: https://www.jlab.org/conferences/YSTAR2016/ contains presentations.

[11] Web page of the Workshop on *New Opportunities with High-Intensity Photon Sources* (HISP2017), CUA, Washington, DC, USA, Feb. 2017: https://www.jlab.org/conferences/HIPS2017/ contains presentations.

[12] M. Albrow *et al.*, Mini-Proceedings of the Workshop on *Physics with Neutral Kaon Beam at JLab* (KL2016), JLab, Newport News, VA, USA, Feb. 2016, edited by M. Amaryan, E. Chudakov, C. Meyer, M. Pennington, J. Ritman, and I. Strakovsky, arXiv:1604.02141 [hep–ph].

[13] *Physics opportunities with secondary $K_L$ beam at JLab*, Spokesperson: M. Amaryan (GlueX Collaborations), JLab LoI12–15–001, Newport News, VA, USA, 2015.

[14] *Photoproduction of the very strangest baryons on the proton target in CLAS12*, Spokespersons: L. Guo, M. Dugger, J. Goetz, E. Pasyuk, I.I. Strakovsky, D.P. Watts, N. Zachariou, and V. Ziegler (Very Strange Collaboration for CLAS Collaboration), JLab Proposal E12–11–005A, Newport News, VA, USA, 2013.

[15] *Nucleon resonance structure studies via exclusive KY electroproduction at 6.6 GeV and 8.8 GeV*, Spokespersons: D.S. Carman, R. Gothe, and V. Mokeev (CLAS Collaboration), JLab E12–16–010A, Newport News, VA, USA, 2016.

[16] P. Alba *et al.*, Mini-Proceedings of the Workshop on *Excited Hyperons in QCD Thermodynamics at Freeze-Out* (YSTAR2016), JLab, Newport News, VA, USA, Nov. 2016, edited by M. Amaryan, E. Chudakov, K. Rajagopal, C. Ratti, J. Ritman, and I. Strakovsky, arXiv:1701.07346 [hep–ph].

[17] S. Ali *et al.*, Mini-Proceedings of the Workshop on *New Opportunities with High-Intensity Photon Sources*, CUA, Washington, DC, USA, Nov. 2016, edited by T. Horn, C. Keppel, C. Munoz-Camacho, and I. Strakovsky, arXiv:1704.00816 [nucl–ex].

[18] C. Amsler, S. Eidelman, T. Gutsche, C. Hanhart, S. Spanier, and N.A. Törnqvist, in: Ref. [1]; S. Descotes-Genon and B. Moussallam, Eur. Phys. J. C **48**, 553 (2006).

[19] J. Julia-Diaz *et al.*, Phys. Rev. C **75**, 015205 (2007).

[20] H. Sato and T.S.-H. Lee, J. Phys. G **36**, 0730010 (2009).

[21] Z.-W. Liu *et al.*, Phys. Rev. D **95**, 014506 (2017).

[22] W. Kamleh, PoS **CD15**, 037 (2016).

[23] N.N. Scoccola *et al.*, Phys. Lett. B **201**, 425 (1988); B **220**, 658 (1989).

[24] C. Callan *et al.*, Phys. Lett. B **202**, 269 (1988).

[25] L.Ya. Glozman and D.O. Riska, Phys. Rept. **268**, 263 (1996).

[26] K.-F. Liu *et al.*, PoS LATTICE2013, 507 (2014).

[27] F. Coester *et al.*, Nucl. Phys. A **364**, 335 (1998).

[28] R.G. Edwards, N. Mathur, D.G. Richards, and S.J. Wallace (Hadrons Spectrum Collaboration), Phys. Rev. D **87**, 054506 (2013).

[29] J.J. Dudek and R.G. Edwards, Phys. Rev. D **85**, 054016 (2012).

[30] D.G. Richards, in: *Workshop on Physics with Neutral Kaon Beam at JLab: mini-Proceedings*, arXiv:1604.02141 [hep–ph] (February, 2016), p. 170.

[31] R.G. Edwards, in: *Workshop on Excited Hyperons in QCD Thermodynamics at Freeze-Out: mini-Proceedings*, arXiv:1701.07346 [hep–ph] (November, 2016), p. 117.

[32] R. Bellwied, S. Borsanyi, Z. Fodor, S.D. Katz, and C. Ratti, Phys. Rev. Lett. **111**, 202302 (2013).

[33] S. Borsanyi *et al.* (Wuppertal-Budapest Collaboration), JHEP **1009**, 073 (2010).

[34] A. Bazavov *et al.* (HotQCD Collaboration), hys. Rev. D **90**, 094503 (2014).

[35] M. Floris, Nucl. Phys. A **931**, 103 (2014).

[36] L. Adamczyk *et al.* (STAR Collaboration), Phys. Rev. Lett. **112**, 032302 (2014).

[37] L. Adamczyk *et al.* (STAR Collaboration), Phys. Rev. Lett. **113**, 092301 (2014).

[38] P. Alba, W. Alberico, R. Bellwied, M. Bluhm, V. Mantovani Sarti, M. Nahrgang, and C. Ratti, Phys. Lett. B **738**, 305 (2014).

[39] J. Adam *et al.* (ALICE Collaboration), arXiv:1606.07424 [nucl–ex].

[40] R. Dashen, S. K. Ma, and H. J. Bernstein, Phys. Rev. **187**, 345 (1969).

[41] R. Venugopalan and M. Prakash, Nucl. Phys. A **546**, 718 (1992).

[42] F. Karsch, K. Redlich, and A. Tawfik, Phys. Lett. B **571**, 67 (2003).

[43] A. Tawfik, Phys. Rev. D **71**, 054502 (2005).

[44] R. Hagedorn, Prog. Sci. Culture **1**, 395 (1976).

[45] S. Capstick and N. Isgur, Phys. Rev. D **34**, 2809 (1986).

[46] D. Ebert, R. N. Faustov, and V. O. Galkin, Phys. Rev. D **79**, 114029 (2009).

[47] A. Majumder and B. Muller, Phys. Rev. Lett. **105**, 252002 (2010).

[48] A. Bazavov *et al.*, Phys. Rev. Lett. **113**, 072001 (2014).

[49] P. Alba *et al.*, arXiv:1702.01113 [hep–lat].

[50] M. M. Giannini and E. Santopinto, Chin. J. Phys. **53**, 020301 (2015).

[51] C. Amsler *et al.* (Particle Data Group), Phys. Lett. B **667**, 1 (2008).

[52] E. Santopinto and J. Ferretti, Phys. Rev. C **92**, 025202 (2015).

[53] The Durham HEP Reaction Data Databases (UK) (Durham HepData): http://durpdg.dur.ac.uk/hepdata/reac.html .

[54] M.G. Albrow *et al.*, Nucl. Phys. B **23**, 509 (1970).

[55] M.G. Albrow, in: *Workshop on Physics with Neutral Kaon Beam at JLab: mini-Proceedings*, arXiv:1604.02141 [hep–ph] (February, 2016), p. 5.

[56] A.D. Brody *et al.*, Phys. Rev. Lett. **22**, 966 (1969).

[57] S.D. Drell and M. Jacob, Phys. Rev. **138**, B1312 (1965).

[58] The George Washington University INS Data Analysis Center (SAID); http://gwdac.phys.-gwu.edu .

[59] G. Höhler, *Pion-Nucleon Scattering*, Landoldt-Börnstein, Vol. I/9b2, edited by H. Schopper (Springer-Verlab, Berlin, 1983).

[60] R.A. Arndt, W.J. Briscoe, I.I. Strakovsky, and R.L. Workman, Phys. Rev. C **74**, 045205 (2006)

[61] D.M. Manley, in: *Workshop on Physics with Neutral Kaon Beam at JLab: mini-Proceedings*, arXiv:1604.02141 [hep–ph] (February, 2016), p. 42.

[62] H. Zhang, J. Tulpan, M. Shrestha, and D.M. Manley, Phys. Rev. C **88**, 035204 (2013).

[63] H. Zhang, J. Tulpan, M. Shrestha, and D.M. Manley, Phys. Rev. C **88**, 035205 (2013).

[64] H. Kamano, S.X. Nakamura, T.-S.H. Lee, and T. Sato, Phys. Rev. C **90**, 065204 (2014).

[65] H. Kamano, S.X. Nakamura, T.-S.H. Lee, and T. Sato, Phys. Rev. C **92**, 025205 (2015)

[66] J.K. Hassall *et al.*, Nucl. Phys. B **189**, 397 (1981).

[67] D.J. Wilson, J.J. Dudek, R.G. Edwards, and C.E. Thomas, Phys. Rev. D **91**, 054008 (2015)

[68] J.J. Dudek *et al.* (Hadron Spectrum Collaboration), Phys. Rev. Lett. **113**, 182001 (2014).

[69] J. Prevost *et al.* (Cern-Heidelberg-Saclay Collaboration), Nucl. Phys. B **69**, 246 (1974).

[70] W. Cameron *et al.* (Rutherford-London Collaboration), Nucl. Phys. B **143**, 189 (1978).

[71] J. Timmermans *et al.* (Amsterdam-CERN-Nijmegen-Oxford Collaboration), Nucl. Phys. B **112**, 77 (1976).

[72] W. Cameron *et al.* (Rutherford-London Collaboration), Nucl. Phys. B **131**, 399 (1977).

[73] V.D. Burkert *et al.*, arXiv:1412.0241 [nucl–ex].

[74] A.V. Anisovich, R. Beck, E. Klempt, V.A. Nikonov, A.V. Sarantsev and U. Thoma, Eur. Phys. J. A **48**, 15 (2012).

[75] H. Osmanović, Talk at The International Workshop on Partial Wave Analyses and Advanced Tools for Hadron Spectroscopy (PWA9/ATHOS4, Bad Honnef near Bonn (Germany), March, 2017.

[76] A. Švarc, Talk at The International Workshop on Partial Wave Analyses and Advanced Tools for Hadron Spectroscopy (PWA9/ATHOS4, Bad Honnef near Bonn (Germany), March, 2017.

[77] G. Höhler, $\pi$N Newsletter **9**, 1 (1993).

[78] N.G. Kelkar and M. Nowakowski, Phys. Rev. A **78**, 012709 (2008), and references therein.

[79] G.F. Chew and S. Mandelstam, Phys. Rev. **119**, 467 (1960).

[80] S. Ceci, J. Stahov, A. Švarc, S. Watson, and B. Zauner, Phys. Rev. D **77**, 116007 (2008).

[81] P. Masjuan, J. Ruiz de Elvira, and J. José Sanz-Cillero, Phys. Rev. D **90**, 097901 (2014).

[82] A. Š, M. Hadžimehmedović, H. Osmanović, J. Stahov, L. Tiator, and R.L. Workman, Phys. Rev. C **88**, 035206 (2013).

[83] A. Š, M. Hadžimehmedović, R. Omerović, H. Osmanović, and J. Stahov, Phys. Rev. C **89**, 45205 (2014).

[84] A. Š, M. Hadžimehmedović, H. Osmanović, J. Stahov, L. Tiator, and R.L. Workman, Phys. Rev. C **89**, 065208 (2014).

[85] A. Š, M. Hadžimehmedović, H. Osmanović, J. Stahov, and R.L. Workman, Phys. Rev. C **91**, 015207 (2015).

[86] A. Š, M. Hadžimehmedović, H. Osmanović, J. Stahov, L. Tiator, and R.L. Workman, Phys. Lett. B **755**, 452 (2016).

[87] Michiel Hazewinkel: Encyclopaedia of Mathematics, Vol.**6**, Springer, 31. 8. 1990, pg. 251.

[88] S. Ciulli and J. Fischer, Nucl. Phys. **24**, 465 (1961).

[89] I. Ciulli, S. Ciulli, and J. Fisher, Nuovo Cimento **23**, 1129 (1962).

[90] E. Pietarinen, Nuovo Cimento Soc. Ital. Fis. **12A**, 522 (1972).

[91] E. Pietarinen, Nucl. Phys. B **107**, 21 (1976).

[92] R.L. Workman, M.W. Paris, W.J. Briscoe, and I.I. Strakovsky, Phys. Rev. C **86**, 015202 (2012).

[93] D. Rönchen, M. Döring, F. Huang, H. Haberzettl, J. Haidenbauer, C. Hanhart, S. Krewald, U.-G. Meißner, and K Nakayama, Eur. Phys. J. A **49**, 44 (2013).

[94] M. Döring, C. Hanhart, F. Huang, S. Krewald, U.-G. Meißner, and D. Rönchen, Nucl. Phys. A **851**, 58 (2011).

[95] M. Döring, C. Hanhart, F. Huang, S. Krewald, and U.-G. Meißner, Nucl. Phys. A **829**, 170 (2009).

[96] S. Ceci, M. Döring, C. Hanhart, S. Krewald, U.-G. Meißner, and A. Švarc, Phys. Rev. C **84**, 015205 (2011).

[97] R.A. Arndt, I.I. Strakovsky, and R.L. Workman, Phys. Rev. C **68**, 042201(R) (2003), Ya.I. Azimov, R.A. Arndt, I.I. Strakovsky, and R.L. Workman, Phys. Rev. C **68**, 045204 (2003).

[98] A.V. Anisovich, E. Klempt, V.A. Nikonov, A.V. Sarantsev, H. Schmieden, and U. Thoma, Phys. Lett. B **711**, 162 (2012).

[99] R. Tibshirani, J.R. Statist. Soc. B **58** (1996) 267.

[100] *The Elements of Statistical Learning: Data Mining, Inference, and Prediction*, T. Hasti, R. Tibshirani, J. Friedman, Springer 2009 second ed.; E-book available at http://statweb.stanford.edu/ tibs/ElemStatLearn/index.html .

[101] *An Introduction to Statistical Learning*, Gareth James, Daniela Witten, Trevor Hastie and Robert Tibshirani, Springer 2015; 6th printing; E-book available at http://www-bcf.usc.edu/ gareth/ISL/ .

[102] B. Guegan, J. Hardin, J. Stevens, and M. Williams, JINST **10**, P09002 (2015).

[103] J. Landay, M. Döring, C. Fernández-Ramírez, B. Hu, and R. Molina, Phys. Rev. C **95**, 015203 (2017).

[104] D. Agadjanov, M. Döring, M. Mai, U.-G. Meißner, and A. Rusetsky, arXiv:1603.07205 [hep–lat].

[105] R.L. Workman, M.W. Paris, W.J. Briscoe, and I.I. Strakovsky, Phys. Rev. C **86**, 015202 (2012).

[106] G. D'Agostini, Nucl. Instrum. Meth. A **346**, 306 (1994).

[107] R.D. Ball *et al.* (NNPDF Collaboration), JHEP **1005**, 075 (2010).

[108] L. Wilkinson and G.E. Dallal, Technometrics **23**, 377 (1981).

[109] T. W. Anderson, and D. A. Darling, Annals of Mathematical Statistics **23**, 193 (1952).

[110] M. A. Stephens, Journal of the American Statistical Association **69**, 730 (1974).

[111] M. Döring, arXiv:1603.07265 [nucl–th].

[112] P.C. Bruns, M. Mai, and U.-G. Meißner, Phys. Lett. B **697**, 254 (2011).

[113] M. Mai and U.-G. Meißner, Nucl. Phys. A **900**, 51 (2013).

[114] M. Mai and U. G. Meißner, Eur. Phys. J. A **51**, 30 (2015).

[115] Y. Ikeda, T. Hyodo, and W. Weise, Nucl. Phys. A **881**, 98 (2012).

[116] Z. H. Guo and J. A. Oller, Phys. Rev. C **87**, 035202 (2013).

[117] A. Cieplý and J. Smejkal, Nucl. Phys. A **881**, 115 (2012).

[118] A. Cieply *et al.*, Nucl. Phys. A **954**, 17 (2016).

[119] K. Moriya *et al.* [CLAS Collaboration], Phys. Rev. C **87**, 035206 (2013).

[120] P. Estabrooks *et al.*, Nucl. Phys. B **133**, 490 (1978).

[121] D. Aston *et al.*, Nucl. Phys. B **296**, 493 (1988).

[122] J. Gasser and U.-G. Meißner, Nucl. Phys. B **357**, 90 (1991).

[123] U.-G. Meißner and J. Oller, Nucl. Phys. A **679**, 671 (2001).

[124] J. Oller, E. Oset, and J. Palomar, Phys. Rev. D **63**, 114009 (2001).

[125] M. Frink, B. Kubis, and U.-G. Meißner, Eur. Phys. J. C **25**, 259 (2002).

[126] J. Bijnens and P. Talavera, Nucl. Phys. B **669**, 341 (2003).

[127] T.A. Lähde and U.-G. Meißner, Phys. Rev. D **74**, 034021 (2006).

[128] V. Bernard and E. Passemar, JHEP **04**, 001 (2010).

[129] Z.-H. Guo, J. Oller, and J. Ruiz de Elvira, Phys. Rev. D **86**, 054006 (2012).

[130] J.F. Donoghue, J. Gasser, and H. Leutwyler, Nucl. Phys. B **343**, 341 (1990).

[131] V. Bernard and E. Passemar, Phys. Lett. B **661**, 95 (2008).

[132] S. Descotes-Genon and B. Moussallam, Eur. Phys. J. C **48**, 553 (2006).

[133] J.R. Pelaez and A. Rhodas, arXiv:1703.07661.

[134] F. Niecknig and B. Kubis, JHEP **1510**, 142 (2015).

[135] M. Döring, U.-G. Meißner, and W. Wang, JHEP **1310**, 011 (2013).

[136] D.R. Boito, R. Escribano, and M. Jamin, JHEP **1009**, 031 (2010).

[137] P. Büttiker, S. Descotes-Genon, and B. Moussallam, Eur. Phys. J. C **33**, 409 (2004).

[138] P. Degtyarenko and B. Wojtsekhowski, in: *Workshop on Physics with Neutral Kaon Beam at JLab: mini-Proceedings*, arXiv:1604.02141 [hep–ph] (February, 2016), p. 214.

[139] T. Horn, C. Keppel, C. Munoz-Camacho, I. Strakovsky, *Workshop on New Opportunities with High-Intensity Photon Sources: mini-Proceedings*, arXiv:1704.00816 [nucl–ex] (February, 2017), p. 61.

[140] We used modified version of Pythia package for the GlueX Collaboration at JLab Hall D, http://home.thep.lu.se/torbjorn/Pythia.html .

[141] G. McClellan *et al.*, Phys. Rev. Lett. **21**, 1593, (1971).

[142] A. Titov and T.-S.H. Lee, Phys. Rev. C **67**, 065205 (2003).

[143] A. Titov and B. Kampfer, Phys. Rev. C **76**, 035202 (2007).

[144] T. Mibe *et al.* (CLAS Collaboration), Phys. Rev. C **76**, 052202 (2007).

[145] G.W. Brandenburg *et al.*, Phys. Rev. D **7**, 708 (1973).

[146] I. Larin, in: *Workshop on Physics with Neutral Kaon Beam at JLab: mini-Proceedings*, arXiv:1604.02141 [hep–ph] (February, 2016), p. 198.

[147] Application Software Group, GEANT - *Detector Description and Simulation Tool*, CERN Program Library Long Writeup W5013, CERN, Geneva, Switzerland (1994).

[148] L. Keller, private communication, 2015.

[149] J. Allison *et al.* (Geant4 Collaboration), Nucl. Instrum. and Meth. A **835**, 186 (2016).

[150] T. Goorley *et al.*, Nucl. Tech. **180**, 298 (2012); https://mcnp.lanl.gov/ .

[151] D. Androic *et al.*, Nucl. Instrum. Meth. A **646**, 59 (2011).

[152] M. Spata, private communication, 2016.

[153] E. Pooser, Ph.D. Thesis, Florida International University (2016).

[154] F. Barbosa, C. Hutton, A. Sitnikov, A. Somov, S. Somov, and I. Tolstukhin, Nucl. Instrum. and Meth. A **795**, 376 (2015).

[155] G.A. Slayer*et al.*, Phys. Rev. **169**, 1045 (1968).

[156] K.G. Vorsburgh *et al.*, Phys. Rev. D **6**, 1834 (1972).

[157] G.W. Brandenburg *et al.*, Phys. Rev. D **7**, 708 (1973).

[158] C. Keith, in: *Workshop on Physics with Neutral Kaon Beam at JLab: mini-Proceedings*, arXiv:1604.02141 [hep–ph] (February, 2016), p. 223.

[159] D. Meekins, TGT-CALC-401-007: *Hall D Cryogenic Target: General calculations for relief of the $LH_2$ target*.

[160] H. Seraydaryan *et al.*, Phys. Rev. C **89**, 055206 (2014).

[161] H. Al Ghoul *et al.* (GlueX Collaboration) arXiv:1512.03699v4 [nucl–ex].

[162] S. Tylor, in: *Workshop on Physics with Neutral Kaon Beam at JLab: mini-Proceedings*, arXiv:1604.02141 [hep–ph] (February, 2016), p. 205.

[163] P. Capiluppi, G. Giacomelli, G. Mandrioli, A.M. Rossi, P. Serra-Lugaresi, and L. Zitelli, IFUB-81-25.

[164] R.J. Yamartino, Ph. D Thesis, SLAC Standford University, May (1974).

[165] KLong bi-weekly group meeting, https://wiki.jlab.org/klproject/index.php/March-1st,-2017 .

[166] D.A. Sharov, V.L. Korotkikh, and D.E. Lanskoy, Eur. Phys. J. A **47**, 109 (2011).

[167] Biagi *et al.*, Z Phys. C **34**, 175 (1987).

[168] J.C.M. Armitage *et al.*, Nucl. Phys. B *123*, 11 (1977).

[169] D. Cline, J. Penn, and D.D. Reeder, Nucl. Phys. B *22*, 247 (1970).

[170] P. Bajllon *et al.*, Nucl. Phys. B *134*, 31 (1978).

[171] R. Bijker, J. Ferretti, G. Galata, H. Garcia-Tecocoatzi, and E. Santopinto, Phys. Rev. D **94**, 074040 (2016).

[172] *Project X Physics Study*, https://indico.fnal.gov/event/projectxps12 .

[173] *Project X: Physics Opportunities*, Part 1 edited by S.D. Holmes, arXiv:1306.5022 [physics.acc–ph]; Part 2 edited by A.S. Kronfeld and R.S. Tschirhart, arXiv:1306.5009 [physics.acc–ph]; and Part 3 edited D.M. Asner, P.C. Bhat, S. Henderson, R. Plunkett, arXiv:1306.5024 [physics.acc–ph].

[174] C. Quigg, private communication, 2015.

[175] B. Winstein *et al.*, *High precision, high intensitivity $K^0$ physics at the main injector*, FNAL LoI 0804, 1988.

[176] H. Ohnishi, in: *Workshop on Physics with Neutral Kaon Beam at JLab: mini-Proceedings*, arXiv:1604.02141 [hep–ph] (February, 2016), p. 22.

[177] *Summary of the Report from the Working Group for The External Expert Panel on the Radioactive Material Leak Accident at the Hadron Experimental Facility of J-PARC*; http://j-parc.jp/en/topics/HDAccident20130827_02.pdf

[178] *Charmed baryon spectroscopy experiment at J-PARC*, H. Noumi *et al.*, J-PARC Proposal E50, 2012.

[179] M. Naruki, private communication, 2015.

[180] K. Abe *et al.* (Belle Collaboration), Phys. Lett. B **524**, 33 (2002); T. Lesiak *et al.* (Belle Collaboration), Phys. Lett. B **605**, 237 (2004).

[181] B. Aubert *et al.* (BaBar Collaboration), Phys. Rev. D **78**, 034008 (2008); B. Aubert *et al.* (BaBar Collaboration), Phys. Rev. Lett. **97**, 112001 (2006); B. Aubert *et al*. (BaBar Collaboration), Phys. Rev. Lett. **95**, 142003 (2005).

[182] V. Ziegler, in: *Workshop on Physics with Neutral Kaon Beam at JLab: mini-Proceedings*, arXiv:1604.02141 [hep–ph] (February, 2016), p. 113.

[183] W. Erni *et al.* ($\overline{P}$ANDA Collaboration), arXiv:0903.3905 [hep–ex].

[184] J. Ritman, invited talk at *Excited Hyperons in QCD Thermodynamics at Freeze-Out* Workshop, see Ref. YSTAR2016.

[185] S. Paul, private communication, 2016.

[186] J. Goity, P. Huovinen, J. Ritman, and A, Tang, in: Workshop on *Excited Hyperons in QCD Thermodynamics at Freeze-Out: mini-Proceedings*, arXiv:1701.07346 [hep–ph], p. 158.

[187] A.W. Steiner, M. Prakash, J.M. Lattimer, and P.J. Ellis, Phys. Rep. **411**, 325 (2005).

[188] C.J. Horowitz and J. Piekarewicz, Phys. Rev. Lett. **86**, 5647 (2001).

[189] J. Xu *et. al.*, Astrophys. J. **697**, 1549 (2009).

[190] A.W. Steiner, J.M. Lattimer, and E.F. Brown, Astrophys. J. **722**, 33 (2010).

[191] B.G. Todd-Rutel and J. Piekarewicz, Phys. Rev. Lett. **95**, 122501 (2005).

[192] De-Hua Wen, Bao-An Li, and Lie-Wen Chen, Phys. Rev. Lett. **103**, 211102 (2009).

[193] S.J. Pollock and M.C. Welliver, Phys. Lett. B **464**, 177 (1999).

[194] M.B. Tsang *et. al.*, Phys. Rev. C **86**, 015803 (2012).

[195] K. Hebeler, J.M. Lattimer, C.J. Pethick and A. Schwenk, Phys. Rev. Lett. **105**, 161102 (2010).

[196] M. Centelles, X. Roca-Maza, X. Viñas, and M. Warda, Phys. Rev. Lett. **102**, 122502 (2009).

[197] A. Carbone *et. al.*, Phys. Rev. C **81**, 041301(R) (2010).

[198] L.W. Chen *et. al.*, Phys. Rev. C **82**, 024321 (2010).

[199] A. Tamii *et. al.*, Phys. Rev. Lett. **107**, 062502 (2011).

[200] B.A. Li, L.W. Chen, and C.M. Ko, Phys. Rep. **464**, 113 (2008).

[201] M.B. Tsang *et. al.*, Phys. Rev. Lett. **102**, 122701 (2009).

[202] Yu. Valdau *et al.*, Phys. Rev. C **84**, 055207 (2011).

[203] P. Adlarson *et al.*, arXiv:1702.07212.